Topics in General Relativity

Thesis by

Mihai Bondarescu

In Partial Fulfillment of the Requirements
for the Degree of
Doctor of Philosophy

California Institute of Technology
Pasadena, California

2007
(Defended May 21, 2007)

© 2007
Mihai Bondarescu
All Rights Reserved

To my students

Acknowledgements

First and foremost, I thank Professor Yanbei Chen for suggesting a good research problem and for all the good advice he gave me during my years as a graduate student. I have never been as productive in science as I have been while working under Yanbei's guidance.

I would like to thank my senior faculty advisors for the time and energy they've invested in me. I thank Ed Seidel for providing honest and useful advice and guidance at every time I have asked for it. Without Ed, many of the good things that happened to me would not have taken place. I won the prize for the best student talk at GR 16 and I wouldn't even have been there nor given a talk without Ed. I thank him for the opportunity to teach Gravitational Waves at graduate level and for teaching me how to ski on the most memorable mountain trip I've ever enjoyed.

I thank Barry Barish for agreeing to be my advisor when no one else would. I thank Barry for making peace where was war. I thank John Preskill and Mark Wise and Marc Kamionkowski for being members of my exam committees and for advising me along the way.

I thank Michael Hoffmann for helping me navigate rough seas. He had an open door and offered much needed help when I found myself in trouble.

I thank David Politzer for telling me the truth and nothing but the truth, even when the powers-that-be didn't want the truth told.

Kip Thorne has spent a lot of time on me that I am grateful for. If I am to name the single most important thing that Kip did for my benefit, was taking time to help me get out of the legal trouble I found myself in after teaching String Theory at the University of California Irvine together with Caltech Professor Anton Kapustin. Of all people, Kip is the one respected the most mainly for writing – along with Charles Misner and John Wheeler – a book that shaped the world and my younger years. Kip is also the only person I have ever obeyed.

I thank my fellow graduate students Ketan Vyas, Oleg Kogan, Graeme Smith, Ardis Eliasdottir, Claudiu Giurumescu, Geoffrey Lovelace, Jie Yang, Tristan McLaughlin for their friendship and support.

During the years I spent in graduate school, I was supported by many generous sponsors. It is mainly their generous support that enabled me to travel through 17 countries and 23 states in order to give 12 conference presentations, 13 seminar talks, 4 posters, and teach 3 lecture series. Albert

Einstein Institute paid for my travel to South Africa, where I earned the prize for best talk at GR 16, and supported me during my stay in Europe. The Center for Computation and Technology and Louisiana State University supported me while I taught a series of graduate-level lectures on Gravitational Waves there. Travel to conferences and summer schools, as well as local support and participation fees, were generously provided by The Perimeter Institute; The Center for Gravitational Wave Astronomy associated with The University of Texas at Brownsville; Cornell University; The University of Parma, Italy; Max Planck Institute fuer Astrophysik, Heidelberg, Germany; Max Planck Institute Fuer Gravitationsphysik, Golm, Germany; National Science Foundation; The Heraeus Foundation; and The Humbolt Foundation.

I thank Marius Piso and The Romanian Space Agency for the support they offered to me in organizing a summer school on General Relativity in Romania.

I thank my students, Katie Mach (AEI), Florin Mingireanu (Caltech and CCT), Ioana Bercea (University of Chicago), Irina Craciun (CCT), Razvan Carbunescu (CCT), Elena Caraba (CCT), Lucian Patcas (Dublin), for they have put their future in my hands by allowing me to write letters for them. It's been a pleasure to work with such wonderful people.

During my travels as a scientist, Mihai Badus and Rodica Springean, Mihaela and Mircea Vatui, Dorina Diaconu and Charlie King made me feel at home in their homes. I thank them for giving me so much more than the hotels and rental cars I could barely fit in my travel budget.

This thesis would not have been ready in time without the help of my sister, Ruxandra Bondarescu, and Andrew Lundgren. They carefully proofread the manuscript, checked my calculations, and gave me valuable advice about the content and the format of this document.

I would have never made it in science without my very first advisor - Dumitru Vulcanov nor without the great teachers from the Grigore Moisil Computer Science high school in Timisoara, Romania. From my class of about 30 people I know of 6 who are in the US either having completed their Ph.D. or as graduate students.

Last but not least, my gratitude goes to my family for giving me the best they could. My Mother introduced me to science at a very early age and has always been my accomplice in all things, from skipping school to play with my formulas to playing on the real estate market to make a little fortune. My wife, Lisa, stood by my side for good and for worse. She loved me when I was poor and when I was unemployed. She gave me courage to take on the world if need be.

Abstract

This thesis is based on three of the five research projects I have worked on during my graduate student years. Each of these projects resulted in a paper a chapter of this thesis is based on. Two other papers I published during my stay at Caltech are not included, as they are not related to the research reported here.

After a brief introduction in the first chapter, in chapter two I discuss a simple way to greatly reduce tilt instability in Advanced LIGO by changing the mirror shape from nearly-flat previously considered mesa beams to nearly a nearly concentric shape that would provide the beam characteristics without the tilt instability. I also propose a family of hyperboloidal beams that join the nearly-flat and nearly-concentric mesa beams in a continuous manner.

In chapter three I report the results of a recent search for the lowest value of thermal noise that can be achieved in LIGO by changing the mirror shape. I discuss in detail the beam properties and point out some of the characteristics of an advanced LIGO that uses these beams. Such an instrument, if built, would have an event rate roughly three times higher than an advanced LIGO using the Mesa beams introduced in chapter 2.

Chapter four, which is also the last chapter of this thesis, is based on a Numerical Relativity project. I compute embeddings of general two-dimensional surfaces with spherical topology in flat 3D space using a minimization algorithm. The minimization problem is similar to the one solved in chapter three, albeit in a somewhat different setting. The code was implemented as a thorn in the Cactus Computational Toolkit.

Contents

List of Figures

List of Tables

Chapter 1

Introduction

LIGO [1] and its international partners are likely to detect gravitational waves in the near future. This will open a new observational window onto the universe. If we choose to stay rather optimistic, gravitational waves interferometers such as LIGO and LISA [2] will have successful detections during the next few years, and will have a strong impact on such diverse branches of physics as astronomy, astrophysics, cosmology, and string theory.

Significant emission of gravitational waves is expected from violent astrophysical events such, as collisions and coalescences of neutron stars or black holes. The emitted gravitational waves will carry detailed information about their sources. Waveforms from colliding black holes will bring insights on the highly nonlinear aspects of general relativity. Neutron star collisions may reveal information about their mass-radius relation and, hence, the equation of state at nuclear densities [6]. Gravitational radiation from the early universe can be detected from a much earlier time than electromagnetic radiation, and thus can help us understand how the universe started and maybe how it will end [7, 8]. If cosmic superstrings exist and generate gravitational radiation that is detected, the impact of the discovery on theoretical physics may be higher than that of a major accelerator [9].

Gravitational wave detectors have been operating for over 40 years. Early attempts to detect gravitational waves were made in the 1960s using resonant bar detectors by Joseph Weber [10, 11], and work on this devices continued ever since. Current bar detectors are sensitive to only the strongest potential sources of gravitational waves in our galaxy such as supernova explosions and the end stage of binary black hole inspirals [12].

The most promising currents attempts to detect gravitational waves are ground-based, kilometer-scale gravitational waves detectors like LIGO, VIRGO, GEO600, TAMA300. The gravitational wave searches placed upper limits on the strength of gravitational waves from various sources such as known millisecond pulsars (see results from the fifth science run of LIGO [13, 14]). However,

---

[1] LIGO stands for Laser Interferometer Gravitational Observatory. See [4] for more details.

[2] LISA stands for Laser Interferometer Space Antenna. See [5] for more details.

as of May 2007, no positive detection of gravitational waves has occurred. All these detectors use same principle. A standard Michelson Interferometer is used to measure the variation in the relative length of its arms. Passing gravitational waves will make the interferometer's arms lengths oscillate. Unfortunately, the oscillations generated by gravitational waves are very small and thus the interferometer needs to have a very high sensitivity and very low level of noise in order to measure such small changes in separations. This thesis will discuss innovative beam shapes and mirror shapes for LIGO interferometers that will minimize the noise and could be be implemented in future generations of detectors.

The LIGO Scientific Collaboration (LSC), an organization counting among its members about 500 scientists at universities in United States and in eight foreign countries [4], operates three interferometers in the US. One 4-km interferometer shares a Louisiana marsh with alligators and tree loggers. [3] Two other interferometers share the same beam tubes in eastern Washington high desert. One has 4 km long arms, and the other measures only 2 km.

There are two interferometric gravitational waves detectors in The European Union. VIRGO is a 3-km detector in Italy, and it comes closest in size to LIGO. GEO 600 is a much shorter interferometer, operated in Germany. It is funded jointly by the Max Planck Society in Germany and the Particle Physics and Astronomy Research Council in the United Kingdom. GEO 600 is also part of LSC and there are currently on-going LSC-VIRGO meetings to organize the sharing of data between these detectors.

I was honored to be an undergraduate and later a graduate student at The Albert Einstein Institute in Potsdam, one of The Max Planck institutes that plays an important role in running the instrument, before coming to Caltech. Professor Yanbei Chen was a senior scientist at the same institute after he completed his Ph.D. at Caltech and before returning to Caltech as a faculty member. GEO 600 is known to be a forerunner of LIGO in terms of technology. Many of the ideas implemented in LIGO, such as the quadruple-pendulum monolithic suspension system, and the optical technique of signal recycling have been tested or are to be tested first in GEO 600. Other interferometers include TAMA 300 in Japan, and AIGO [16] in Australia, which is mainly used for testing.

The leading future gravitational wave detector, LISA, if successfully built, will almost certainly detect gravitational waves from many sources. LISA consists of three space crafts placed on carefully calculated orbits around the sun so that they stay in a equilateral-triangle configuration. The separation between the space crafts is 5 million kilometers. Minute changes in this separation are monitored and measured by laser beams shining between the space crafts.

The work presented here was not done with LISA in mind, and is not expected to be useful there.

---

[3] and these tree loggers have posed serious problems [15].

1.1 Brief Description of a LIGO Interferometer

LIGO and all the other interferometric gravitational wave detectors now in operation use four test masses hung by wires arranged as in Fig.1.1. L_1 denotes the separation between the test masses of the first arm, and L_2 denotes the distance that separates the second arm's test masses. Both L_1 and L_2 are nearly equal to $L = 4km$. At frequencies above eigenfrequencies of the suspension system (about 1 Hz), these test masses are freely falling in an horizontal plane. Theory [18] predicts that gravitational waves passing by will squeeze one arm while stretching the other, thereby changing the quantity

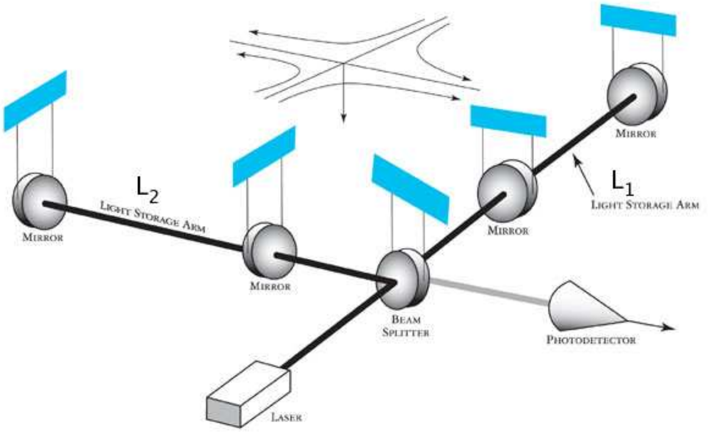

Figure 1.1: A schematic view of a LIGO Interferometer [17]

$$\Delta L = L_1 - L_2. \tag{1.1}$$

For gravitational waves coming from an arbitrary direction, $\frac{\Delta L}{L}$ is given by [19]

$$\frac{\Delta L(t)}{L} = F_+ h_+(t) + F_\times h_\times(t) \equiv h(t) \tag{1.2}$$

F_+ and $F_\times$ depend on the position of the gravitational wave source and the orientation of the detector, and are of order unity; h_+ and $h_\times$ are the gravitational wave strengths for the two polarizations. The gravitational wave strain as experienced by the detector is $h(t)$. The measured quantity, ΔL, is proportional to the arm length. This is why larger detectors are better. LIGO's frequency range is between 10 Hz and 1000 Hz, with the most sensitive frequency at around 100 Hz.

Since light takes much less than 1/100 of one second to travel directly from one test mass to another, it is good to have light bounce in the arm several times. If light bounces in each arm on average 100 times, before the arm length difference is measured, the difference is amplified 100 times, as the arm length is nearly constant in this time. Thus, the arm cavities of LIGO are Fabry-Perot resonant cavities where light is much more intense than in the rest of the instrument.

The LIGO-related original work reported in this thesis is related to mirror designs for these arm cavities. The LIGO-related discussion will focus on the arm cavities.

1.2 The Arm Cavities of Initial LIGO

As of 2007, initial LIGO interferometers are collecting science data, and there is some modest hope they will detect gravitational waves.

A generic interferometer will use Fabri-Perot cavities composed of two mirrors, facing each other. The optical axis is the symmetry axis of the mirrors. For simplicity, the mirrors are assumed to be identical, but should practical considerations dictate otherwise, they need not be. For spherical mirrors, the cavity will be stable if

$$0 < g_1 g_2 < 1, \tag{1.3}$$

where g_1 and g_2 are given by

$$g_i = 1 - \frac{L}{R_i}. \tag{1.4}$$

Above, R_i is the mirror radius, and $i = 1, 2$ labels the two mirrors.

As seen in Eq. 1.3, resonant cavities can be constructed even when one of the mirrors is flat or divergent by using an appropriate second mirror.

In Initial LIGO [4], the Fabri-Perot cavities used in the arms employ spherical mirrors with a curvature radius of 38 km. The diffraction losses are 1 ppm(parts per bounce per million) and the instrument uses light with a wavelength $\lambda = 1064nm$. The total circulating power is 9-12 KW. and the laser output power is 10 W [20].

In Initial LIGO, the mirror shapes are not important as long as they support stable, non-degenerate optical modes. The noise is dominated by suspension thermal noise at low frequencies, and by photon shot noise when higher frequency gravitational waves are observed.

Spherical mirrors have been in use for a very long time. They are well understood and easy to make, and are thus the leading choice in initial LIGO.

1.3 Arm Cavity Design in Advanced LIGO

In Advanced LIGO, the photon shot noise is lowered by increasing the number of photons the instrument averages. Advanced LIGO uses a circulating power of 830 kW in its arm cavities, almost

---

[4] Initial LIGO is the first of several generations of detectors. As this thesis is completed, Initial LIGO detectors are operating at design sensitivity

100 times more than do initial interferometers. The laser power is 125 W, and the power in the arm cavities builds up to 830 KW.

In the baseline design, Advanced LIGO uses nearly-flat spherical mirrors with curvature radii of 53.7 km. This is, however, likely to change to a more-stable, nearly concentric configuration with curvature radius 2076 m.

The suspension thermal noise is also significantly improved so that in the most sensitive region the dominant noise is the internal thermal noise of the mirrors. The shot noise still dominates at high frequencies, and the suspension noise, gradient noise, and seismic noise dominate at low frequencies.

Internal thermal noise arises from imperfect averaging over time-dependednt thermal fluctuations in the mirror surface. As the laser beams that resonate in the arm cavities are used in performing this average, the average is weighted by the power distribution over the mirrors. Thus, the highly illuminated central area weight more than does the mirror boundary that is left nearly in the dark. There are several ways ways to decrease internal thermal noise. One is to increase the mirror area. Averaging over a larger amount of bumps and valleys results in a better average. Another idea is to flatten the beam so that a larger fraction of the mirror is in use and an area as large as possible is weighted roughly in the same way in the averaging.

It is expected that Advanced LIGO will use larger and higher-quality mirrors than initial LIGO. Increasing the mirrors is limited mainly by the technological process of manufacturing large monocrystal sapphire or fused silica. Several attempts have been made to flatten the LIGO beams.

1.4 Mesa Beams in LIGO

O'Shaughnessy and collaborators first proposed the Mesa beams in [10]. They started from a Gaussian. Gaussians are generally stable and well understood beams that are supported by cavities with spherical mirrors. In building Mesa beams, one uses the Minimal Gaussian – the thinnest of all and thus the best for a customized beam. For a cavity of length L, the Minimal Gaussian is given by

$$\Psi(\varpi, \zeta) = \frac{\sqrt{2}}{\sqrt{1+\zeta^2/\ell^2}} \exp\left\{ -\frac{\varpi^2/b^2}{1+\zeta^2/\ell^2} + i\left[\frac{\varpi^2/b^2}{\zeta/\ell + \ell/\zeta} - arctan\left(\frac{\zeta}{\ell}\right) + \frac{2\ell\zeta}{b^2} \right] \right\} \tag{1.5}$$

and is the smallest Gaussian that can resonate in a cavity of length L. Here, $\ell = L/2$ is half the length of LIGOs arm cavity (2 km) and is also equal to the beam's Rayleigh range; $b = \lambda L/2\pi = \lambda\ell/\pi = 2.603$ cm (with the $\lambda = 1.064\mu$m light wavelength) is the radius, at the 1/e point of the beams intensity distribution, at the ends of the cavity, i.e., at $\zeta = \ell$; and b is also the radius, at the $1/e$ point of the beams amplitude distribution, at the beams waist, $\zeta = 0.2$. The spherical mirrors that support a Minimal Gaussian in a symmetric cavity would have a curvature radius L and focal

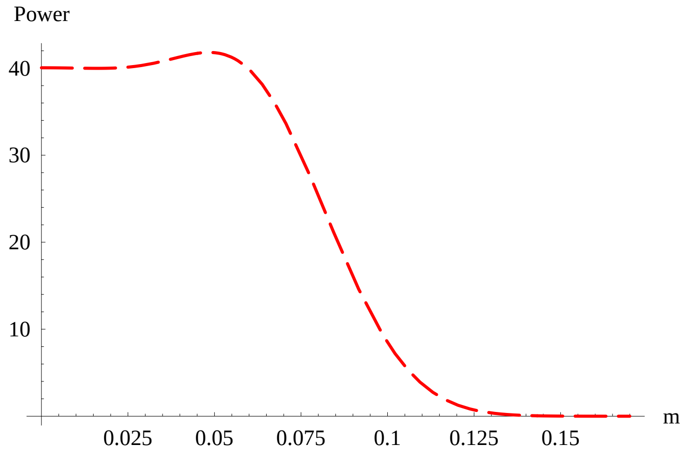

Figure 1.2: Mesa Beam power distribution at the mirror surface. The power distribution at the mirror surface is the same for Mesa Beams supported by both nearly flat and nearly confocal mirrors.

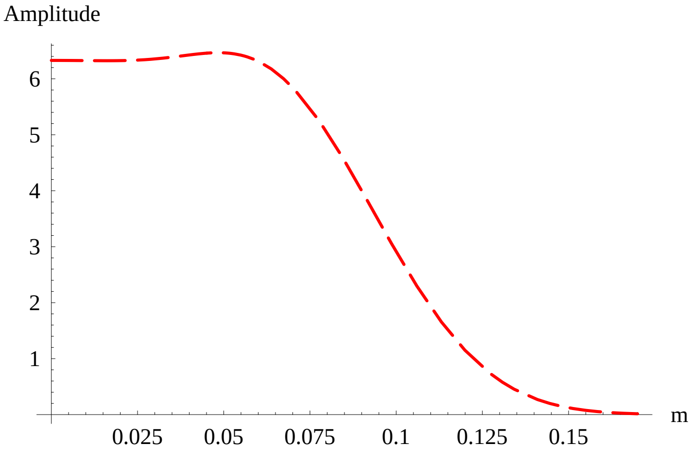

Figure 1.3: Mesa Beam – amplitude of the electric field at the mirror surface. The electric field amplitude at the mirror surface is the same for Mesa Beams supported by both nearly flat and nearly confocal mirrors.

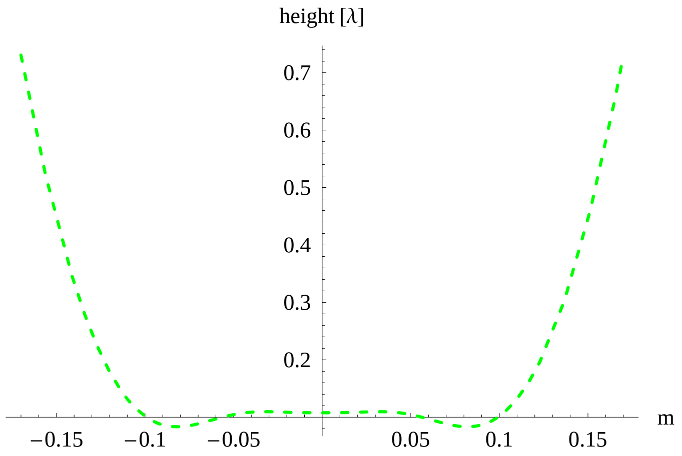

Figure 1.4: Nearly flat Mexican Hat mirror shape. These mirrors support the original Mesa Beam.

length $L/2$. Since the focal points of the two mirrors coincide, such a cavity is called confocal.

A Mesa beam in its first, nearly-flat incarnation, is built by overlapping Minimal Gaussians with symmetry axes parallel to the optic axis, and uniformly distributed within a disk of radius D. In the case of LIGO, $D = 10\ cm$, and the resulting beam has a diffraction loss of 1 ppm in the clipping approximation. Fig. 1.2 and Fig. 1.3 show the power distribution of Mesa beams and, respectively their electric field amplitude distribution.

The mirrors supporting initial Mesa beams are shown in Fig. 1.4. Initially, they have been extracted as phase fronts of the beam's electric field. The mirrors feature a nearly-flat central area with a small bump in the middle surrounded by a high ridge. They somewhat resemble a traditional Mexican hat and are often refereed as Mexican-Hat Mirrors in the LIGO community.

The initial incarnation of the Mesa beam was shown to have a serious tilt instability [17, 22]. To solve this problem, Kip Thorne and I proposed a nearly-concentric incarnation of the Mesa beam in a paper the 2^{nd} chapter of this thesis is based on. The nearly concentric Mesa beam is obtained by overlapping Minimal Gaussians centered on generators of coaxial cones. The density of the Minimal Gaussians is constant and they are all contained within a $D = 10\ cm$ disk on the mirror's surface. The power and electric field amplitude distribution at the mirrors is identical to the nearly flat Mesa power shown in Fig. 1.2 and Fig. 1.3. The mirrors that support our nearly concentric Mesa beams are as close to concentric as the initial Mesa mirrors are close to flat. Just like in flat mirrors, the optical modes in concentric mirrors are unstable. Qualitatively speaking, to make initial Mesa's flat mirrors stable, the Mexican Hat profile is added which makes the mirror somewhat convergent. Concentric mirrors are unstable because they are too convergent. To make them stable, the exact same Mexican Hat profile is subtracted from the mirror height. It thus makes the mirror less convergent and confers optical stability to the cavity. The nearly concentric Mesa

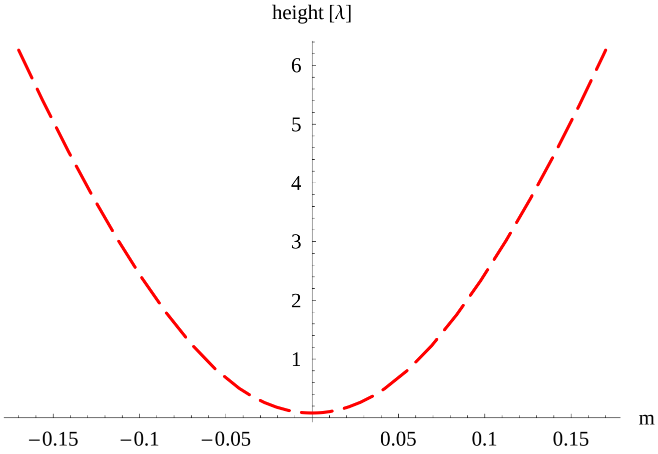

Figure 1.5: Nearly spherical mirror shape that supports the nearly confocal Mesa Beam proposed by Bondarescu and Thorne in [1]. The difference between a spherical mirror of radius equal to one half of the cavity length and the height of this mirror is exactly the height of the nearly flat Mexican Mirror shown in Fig. 1.4. This was first noted in [1] and later fully understood in [17] and [19]

mirror profile we proposed is shown in Fig. 1.5.

The Mesa beam diffraction loss is estimated using the clipping approximation and checked using FFT (Fast Fourier Transform) codes. This method assumes the loss to be equal to the beam's power outside the LIGO mirror if the mirror were infinite. The clipping approximation yields a loss of 1 ppm for both nearly flat and nearly concentric Mesa beams. The beam power outside the mirror is well-behaved and decays almost like a Gaussian's tail.

1.5 Hyperboloidal Beams in LIGO

The two types of Mesa beams can be thought of as the end points of a family of hyperboloidal beams. These are discussed in chapter two of this thesis and in [1].

Heuristically, the hyperboloidal beams are obtained by combining Minimal Gaussians in a similar way to Mesa beams. The difference is that now Gaussian axis are generators of coaxial hyperboloids rather than coaxial cylinders or cones in the case of the two types of Mesa beams.

We parametrized these hyperboloidal beams by a twist angle α which is the angle by which one would have to twist a set of coaxial cylinders to obtain the hyperboloids that generate the beam.

A few notable members of the hyperboloidal beam family include the two Mesa beams, the Minimal Gaussian and the baseline design Gaussian of the Advanced LIGO. The two Mesa beams are obtained for $\alpha = 0$ (nearly flat) and $\alpha = \pi$ (nearly concentric). A nearly confocal cavity supporting the Minimal Gaussian beam is obtained for $\alpha = \pi/2$. There is a duality between the mirror shapes and the intensity profiles of hyperboloidal beams of twist angle α and $\pi - \alpha$. This duality was first noticed in [1] and explored in greater depth in [17, 22, 19]. The mostly Italian

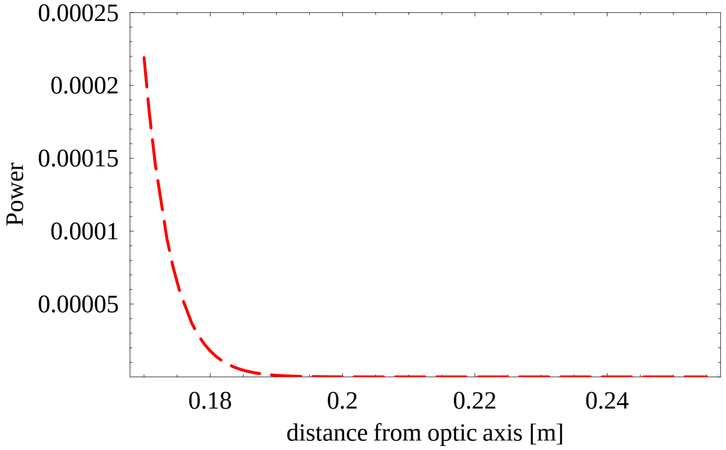

Figure 1.6: Mesa Beam theoretical losses. The plot shows the theoretical power distribution of the Mesa Beam outside the LIGO mirror. According to the clipping approximation, the theoretical loss is the integral of the power outside the mirror. Although the clipping approximation predicts the same losses for nearly flat and nearly confocal Mesa cavities, the nearly confocal ones are seen to have higher losses in practice [32]

group [19] understood analytically the hyperboloidal family of beams that Thorne and I proposed in [1].

The Advanced LIGO baseline design Gaussian is obtained for $\alpha = 0.25276\pi$ and $\alpha = \pi - 0.25176\pi$. The interesting range for LIGO is between the advanced LIGO baseline design Gaussian beam and the Mesa beams. In this range, hyperboloidal beams can be thought of as milder Mesas. If Mesa beams prove too hard to implement or to use, and something better than baseline Gaussian is still desired, one of the hyperboloidal beams in-between can be used. Such a beam would not offer a noise as low as a Mesa; it would behave more like a Gaussian, and thus the mirrors may be easier to manufacture and handle.

1.6 Conical Mirrors in LIGO

Chapter 3 is dedicated to a recent search [3] for the optimal beam for LIGO. We simply wanted to see what is the very best we can do by reshaping the mirrors in order to drive down the thermal noise in LIGO and other gravitational waves detectors built on the same principle.

We employed a simple gradient flow minimization algorithm to search for the beam with minimum noise in the space of all possible beams.

Although the code only took into account coating thermal noise – the largest thermal noise source in Advanced LIGO – all types of thermal noise have been shown to decrease by comparable factors. Our minimization was subject to two constraints:

(i) The beam must have a diffraction loss of 1 ppm – same as Mesa

(ii) The total power of the beam was normalized to be 1.

Provided that other noises stay the same, the resulting beam decreases the overall thermal noise by more than a factor of two. This would significantly increase LIGO's event rate if it can be used.

To see if this beam is indeed suitable for LIGO, we studied its behavior under various perturbations, such as mirror figure errors and tilt. We observed that the new conical mirrors are comparable to Mesa when subjected to perturbations of scale smaller than the mirror radius. When the scale of the perturbations comes close to or exceeds the mirror radius, conical cavities yield much larger diffraction loss than do Mesa cavities subjected to the same perturbation. Since tilting the mirrors can be thought to be a perturbation of wavelength roughly twice the mirror radius, conical cavities are more susceptible to tilt than Mesa. The same holds for mirror translations.

1.7 Isometric Embeddings of Black Hole Surfaces in Flat 3D Space

Chapter 4 discuses a problem that first arose in mathematics, and has applications in physics. The solution presented involves methods typically employed in computer science.

We can briefly state the problem as follows:

Given a two-dimensional surface S, with spherical topology and arbitrary metric g_{ij} written in an arbitrary coordinate system, find a surface in S' embedded in flat three dimensional space with Euclidian metric such that the induced metric on S' is the same as the metric on S.

This surface S' is called an isometric embedding.

The problem is not new and several attempts at solving it have been made in the past. The problem is easily solved if the surface has rotational symmetry [6]. A less trivial solution is known for surfaces with negative curvature [5], and earlier attempts have been made to solve the full 3D problem [16].

Not all surfaces with spherical topology have three dimensional isometric embeddings. A classic example of a non-embeddable surface is the horizon of a Kerr black hole with maximum angular momentum. Such a surface has a rotationally symmetric polar area with negative curvature. This polar area cannot be embedded in 3D space in an rotationally symmetric way; thus, a global embedding cannot be constructed. Local embeddings can be made at the equator or in limited ares of the polar zone.

Not all surfaces have unique embeddings. A clear example is a sheet of paper. As a flat two dimensional surface it can be embedded in three dimensions in infinitely many ways - flat or arbitrarily bent. The different embeddings have the same intrinsic curvature - zero, but their extrinsic curvature will not be the same. Surfaces with spherical topology and positive, nowhere vanishing, intrinsic curvature have unique embeddings if the extrinsic curvature of the embedding is required to be everywhere well-defined. If the extrinsic curvature of the embedding is allowed to be singular, and, if one has one embedding, a second one can be built as follows:

(1) Cut the embedding surface along an arbitrary plane, P.

(2) Build a mirror image of one of the pieces with respect to this plane, P.

(3) Glue this mirror image back to the original surface.

The newly built surface will have an extrinsic curvature singularity along the intersection with the plane P (or the "gluing" line). Such a curvature singularity would not be noticeable to two-dimensional observers living on the surface, but it is not desirable on embedidngs.

If the embedding has a flat area, a second embedidng may exist. Consider, for example, a flat round sheet of paper with a bump on it, somewhere far from the border. This sheet of paper is glued to a sphere such that they form a flat-topped ball. A surface with the same metric and curvature would be obtained by turning the sheet of paper such that the side previously inside the sphere now faces outwards. In this particular case, if one is not given any additional information, it is not possible to label one embedding as "good" and one as "bad."

Our generic solution is based on a minimization problem similar to the one solved in chapter 3. We expanded the surface S' in spherical harmonics. Since the coordinate system that the metric g_{ij} of the original surface is written in is rather arbitrary, we had to introduce a series expansion for this coordinate system as well. We then ran a minimization algorithm over all the expansion coefficients. The minimized quantity was a measure of the difference between the two metrics. If the code reached a minimum that was consistent with zero (numerically, there will always be a residual amount left), an embedding was found. The code was implemented as a thorn in the Cactus Computational Toolkit [33].

Since we expressed our surfaces as a sum of spherical harmonics, the embeddings we computed always had smooth exterior curvature and most surfaces had a unique embedding. In some peculiar situations, like the example above where multiple embeddings exist, it is impossible for a minimization algorithm to tell the difference between two embeddings of the same surface with the same induced metric and non-singular intrinsic curvature. The code will thus converge to one solution and not indicate the presence of the others.

1.7.1 Why is this in my thesis?

I worked on this project after leaving Romania in October 1999. Between October 1999 and February 2000, I also completed three years of academic credit at Freie Universitat Berlin and, after having transfered the two years I completed in Romania, I earned a Diplom Physiker degree in February 2001.

From February 2001 until October 2001, when I joined Caltech, I worked full time on this project at AEI. Strangely, it was Kip Thorne, the only person I have ever obeyed, who advised me to do so when we first met at a LISA conference held at AEI. I had asked Kip how to prepare so as to do well at Caltech, after telling him about the research projects and coursework I had been doing. I asked Kip if there were any exams I should prepare and if there was anything I should learn to make the most of Caltech. Kip advised that this project would be the best thing to do and I obeyed.

The Albert Einstein Institute although, in my opinion, more qualified to award Ph.D.s than most universities, is not authorized by German authorities to do so. Work performed at AEI under Ph.D. fellowships like I had has to be submitted to another university, and the student has to fulfill whatever course and examinations requirements that university may have. Caltech is the university I have chosen. I fulfilled the course and exam requirements of this university and I am submitting this work as part of my thesis.

1.7.2 Relationship With The Rest of The Thesis

The minimization procedure and some of the tricks employed to find the beam with the lowest thermal noise for LIGO discussed in the third chapter of this thesis were I learned and developed at AEI while as part of the Embedding project. Like the research reported in Chapter 3, this project involved running minimization codes in spaces with a large number of dimensions. The generic functions we minimized in [1] are not well-behaved, and we had to invent clever tricks to avoid local minima. The same situation was encountered in the work reported in Chapter 3 of this thesis when we minimize the thermal noise of LIGO's mirrors in the subspace of all possible beams where the constraints regarding diffraction loss and normalization are satisfied.

Bibliography

[1] M. Bondarescu, M. Alcubierre and E. Seidel, “Isometric embeddings of black hole horizons in three-dimensional flat space,” Class. Quant. Grav. **19**, 375 (2002) [arXiv:gr-qc/0109093].

[2] M. Bondarescu and K. S. Thorne, “A new family of light beams and mirror shapes for future LIGO interferometers,” Phys. Rev. D **74**, 082003 (2006) arXiv:gr-qc/0409083.

[3] M. Bondarescu, O. Kogan and Y. Chen, in preparation .

[4] http://www.ligo.org, May 10, 2007 .

[5] http://lisa.nasa.gov/, May 10, 2007 .

[6] A. Abramovici, W.E. Althouse, R.W. Drever, Y. Grusel, S. Kawamura, F.J. Raab, D. Shoemaker, L. Sievers, R.E. Spero, K.S. Thorne, R.E. Vogt, R. Weiss, S.E. Whitcomb, M.E. Zucker, ”LIGO:The Laser Interferometer Gravitational-Wave Observatory”, Science, New Series, Vol. 256, No. 5055 (1992), 325.

[7] M. S. Turner, F. Wilczek, “Relic gravitational waves and extended inflation”, Phys. Rev. Lett. **65**, 3080 (1990).

[8] P. Schewe, B. Stein, and D. Castelvecchi, “Gravitational Wave Background,” Physics News Update **809**, 1 (2007).

[9] “Gravitational wave stochastic background from cosmic (super)strings” X. Siemens, V. Mandic, J. Creighton, arXiv.org:astro-ph/0610920. J. Polchinski, “Cosmic Superstrings Revisited” , International Journal of Modern Physics A **20**, 3413 (2005).

[10] J. Weber, “Detection and Generation of Gravitational Waves”, Phys. Rev. **117**, 305 (1960).

[11] P. F. Michelson, J. C. Price, R. C. Taber, “Resonant Mass Detectors of Gravitational Radiation”, Science **297**, 150 (1987).

[12] E. Coccia, “Resonant-mass detectors of gravitational waves in the short- and medium-term future”, Class. Quantum Grav. **20**, S135 (2003) .

[13] M. Pitkin, G. Woan, “Binary system delays and timing noise in searches for gravitational waves from known pulsars”, arXiv:gr-qc/0703152, LIGO report number P060063-01-Z (2007).

[14] B. Abott *et al.* (LSC), “Analysis of First LIGO Science Data for Stochastic Gravitational Waves”, Phys. Rev. D69 (2004) 122004, arXiv:gr-qc/0312088. B. Abott *et al.* (LSC), “Search for Gravitational Wave Bursts in LIGO’s Third Science Run”, Class. Quantum Grav. **23**, S29 (2006). B. Abbott *et al.* (LSC), “Upper Limits on a Stochastic Background of Gravitational Waves”, Phys. Rev. Lett. **95**, 221101 (2005).

[15] “LIGO’s First Science Run - A Special Report”, http://www.ligo.caltech.edu/LIGO_web/0209news/0209s1r2.html , May 10, 2007.

[16] http://www.anu.edu.au/Physics/ACIGA/.

[17] http://www.ligo.caltech.edu/LIGO_web/PR/scripts/facts.html , May 10, 2007.

[18] C. W. Misner, K. S. Thorne, J. A. Wheeler, *Gravitation*, W. H. Freeman & co., San Francisco, 1973.

[19] K. S Thorne, *300 years of Gravitation*, S. W. Hawking and W. Israel editors, Cambridge University Press, Cambridge, pp 330, 1987.

[20] LIGO Scientific Collaboration, ”LIGO interferometer reference design” http://www.ligo.caltech.edu/advligo/scripts/ref_des.shtml, May 10, 2007.

[21] R. O’Schaughnessy, “Coating thermal noise for arbitrary shaped beams”, Class.Quant.Grav. **23** (2006) 7627, arXiv:gr-qc/0607035.

[22] P. Savov, S. Vyatchanin, “Estimate of tilt instability of mesa-beam and Gaussian-beam modes for advanced LIGO”, Phys. Rev. D **74**, 082002 (2006).

[23] M. Born and E. Wolf, *Principles of Optics*, 2nd edition, New York, The MacMillan Company, 1964.

[24] A. G. Fox and T, Li, ”Resonant modes in a maser interferometer, The Bell System Technical Journal, **40**, 453, (1961).

[25] A. Siegman, *Lasers*, Mill Valley, 1986 University Science Books.

[26] S. Vyatchanin, LIGO Report Number T030272-00 (2003), http://admdbsrv.ligo.caltech.edu/dcc, May 10, 2007.

[27] P. Savov, J. Agresti, Y. Chen, E. D’Ambrosio, “A duality relation between non-spherical optical cavities and its application to gravitational-wave detectors”, arXiv.org:gr-qc/0511062.

[28] V. Galdi, G. Castaldi, V. Pierro, I. M. Pinto, J. Agresti, E. D'Ambrosio and R. DeSalvo, "On the analytic structure of a family of hyperboloidal beams of potential interest for future LIGO interferometers," Phys. Rev. D **73**, 127101 (2006) arXiv:gr-qc/0602074.

[29] J. D. Romano and R. H. Price, "Embedding initial data for black-hole collisions," Class. Quantum Grav. **12**, 875 (1995).

[30] L. L. Smarr, "Surface Geometry of Charged Rotating Black Holes," Phys. Rev. D **7**, 289 (1973).

[31] H.-P. Nollert and H. Herold, "Visualization in Curved Spacetimes: II. Visualization of surfaces via embedding" in *Relativity and Scientific Computing*, edited by F. W. Hehl, R. A. Puntigam, and H. Ruder (Springer Verlag, Berlin, 1998), p. 330.

[32] Hiro Yamamoto, private communication.

[33] The Cactus Code web page

http://www.cactuscode.org, May 10, 2000.

Chapter 2

A New Family of Light Beams and Mirror Shapes for Future LIGO Interferometers

This chapter, with minor modifications, was originally published in [1]

Advanced LIGO's present baseline design uses arm cavities with Gaussian light beams supported by spherical mirrors. Because Gaussian beams have large intensity gradients in regions of high intensity, they average somewhat poorly over fluctuating bumps and valleys on the mirror surfaces (thermal noise). Flat-topped light beams (*Mesa beams*) are being considered as an alternative because they average over thermal noise more effectively. However, the proposed Mesa beams are supported by nearly flat mirrors, which experience a very serious *tilt instability.* In this paper, we propose an alternative configuration in which Mesa-shaped beams are supported by nearly concentric spheres, which experience only a weak tilt instability. The tilt instability is analyzed for these mirrors in a companion paper by Savov and Vyatchanin. We also propose a one-parameter family of light beams and mirrors in which, as the parameter α varies continuously from 0 to π, the beams and supporting mirrors get deformed continuously from the nearly flat-mirrored Mesa configuration ("FM") at $\alpha = 0$, to the nearly concentric-mirrored Mesa configuration ("CM") at $\alpha = \pi$. The FM and CM configurations at the endpoints are close to optically unstable, and as α moves away from 0 or π, the optical stability improves.

2.1 Introduction

The initial gravitational-wave detectors in the Laser Interferometric Gravitational Wave Observatory (LIGO) are now near design sensitivity and are taking science data [3]. The interferometers will be upgraded to a much more sensitive *advanced-LIGO* design beginning in early 2011. Until 2003, the baseline design for advanced LIGO used nearly flat but spherical mirrors in its arm cavities. However, in 2003, Sidles and Sigg [3, 4] showed that these mirrors experience a strong tilt instability: when the mirrors are tilted symmetrically, the light beam slides across their surfaces to an off-center location and its light pressure then pushes hard to increase the tilt. Sidles and Sigg proposed switching to mirrors that are segments of nearly concentric spheres (radii of curvature slightly larger than half the cavity length); such mirrors, they showed, can support Gaussian beams of the same (large) radius as the baseline design, while experiencing a much weakened tilt instability. This triggered a change of the baseline design for advanced LIGO to nearly concentric, spherical mirrors.

Gaussian beams have the serious disadvantage that, because of their steep intensity gradient over most of the beam's area, they average poorly over the fluctuating bumps and valleys on the mirrors' surfaces that are caused by thermal fluctuations (*thermoelastic noise*). O'Shaughnessy and Thorne [5, 6, 7] have proposed improving the averaging and thereby reducing the thermoelastic noise substantially, by replacing the arm cavities' Gaussian beams by flat-topped beams (*Mesa beams*, as Willems has named them), which are supported by nearly flat, Mexican-hat-shaped mirrors. O'Shaughnessy, Strigin and Vyatchanin [8, 7] have shown that the substrate thermoelastic noise for Mesa beams, at fixed diffraction loss, is three times weaker in noise power than for the baseline Gaussian beams, and Agresti [9, 10, 11] and Lovelace [4] have shown that substrate Brownian thermal noise and coating thermal noises are about two times weaker. Correspondingly, Mesa-beam interferometers could see significantly farther into the universe than Gaussian-beam interferometers, producing event rates for inspiraling binaries as much as three times higher [7]. D'Ambrosio et. al. [13, 8, 7] have shown that the nearly flat Mesa-beamed mirrors are practical in all respects that could be analyzed theoretically, and research groups at Caltech [14] and Stanford [15] have built prototype optical cavities with Mesa beams, and are exploring practical issues experimentally.

Unfortunately, the nearly flat, Mexican-hat-shaped mirrors ("FM") proposed by O'Shaugnessy and Thorne to support Mesa beams (Sec. 2.2 below), like the nearly flat, spherical mirrors of the pre-2003 baseline design, experience a severe tilt instability (Vyatchanin [16]; Savov and Vyatchanin [17]). In this paper, motivated by the Sidles-Sigg result that, for Gaussian beams and spherical mirrors, the tilt instability is greatly weakened by switching from nearly flat to nearly concentric mirrors, we propose (Sec. 2.3) a new, nearly concentric mirror design ("CM") that supports Mesa beams. In a companion paper, Savov and Vyatchanin [17] show that the tilt instability is weaker for these CM mirrors than for any other mirrors thus far considered — FM, nearly-flat spherical, and nearly-concentric spherical.

In Secs. 2.2 and 2.3, we mathematically construct our FM and CM beams and their Mexican-hat mirror shapes by superposing minimal-radius Gaussian beams with optic axes that are the generators of cylinders (for FM) and of cones (for CM); Fig. 2.1a,c. In Sec. 2.4 we introduce a one-parameter family of "hyperboloidal" light beams and supporting mirrors, computed by superposing minimal

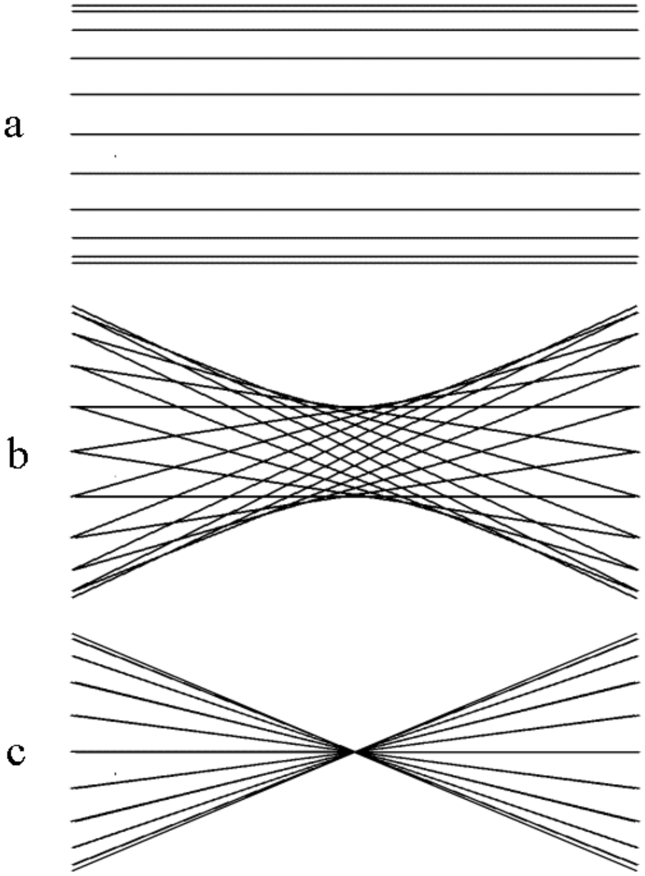

Figure 2.1: Optical axes of the families of minimal Gaussians beams used to construct: (a) an FM Mesa beam [8], denoted in this paper $\alpha = 0$; (c) our new CM Mesa beam, denoted $\alpha = \pi$; (b) our new family of hyperboloidal beams, which deform, as α varies from 0 to π, from a FM beam (a) into a CM beam (c).

Gaussians whose optic axes are the generators of hyperboloids; Fig. 2.1b. For each hyperboloidal beam, the hyperboloid's generators (minimal-Gaussian optic axes) have a fixed twist angle α. As α is varied continually, the hyperboloidal light beams deform continually from Mesa-shaped FM form (at $\alpha = 0$, where the hyperboloids are cylinders) to sharply peaked Gaussian form (at $\alpha = \pi/2$) to Mesa-shaped CM form (at $\alpha = \pi$, where the hyperboloids degenerate to cones).

We do not discuss practical aspects of Mesa-beam interferometers in this paper. For practical issues (e.g., sensitivity to mirror figure errors and misalignments, creation of Mesa beams by driving a Mexican-Hat-mirrored arm cavity with a Gaussian beam, ...), see Refs. [7, 8, 14].

2.2 Mesa Beams Supported by Nearly-Flat Mirrors (FM Beams; $\alpha = 0$)

The Mesa beams supported by nearly-flat Mexican-Hat mirrors ("FM" beams) can be constructed mathematically by a procedure due to O'Shaughnessy and Thorne [6, 8]: One superposes minimal Gaussian beams[1] with their optic axes all parallel to the cavity axis and distributed uniformly over a disk with some radius D, as shown in Fig. 2.1a. Each minimal Gaussian beam (field) is given by

$$\begin{aligned}\Psi(\varpi,\zeta) \quad &= \quad \frac{\sqrt{2}}{\sqrt{1+\zeta^2/\ell^2}} \exp\left\{ \frac{-\varpi^2/b^2}{1+\zeta^2/\ell^2} \right. \\ &\quad \left. +i\left[\frac{\varpi^2/b^2}{\zeta/\ell+\ell/\zeta} - \arctan\left(\frac{\zeta}{\ell}\right) + \frac{2\ell\zeta}{b^2}\right]\right\} . \end{aligned} \tag{2.1}$$

Here ϖ is the transverse distance from the beam's optic axis; ζ is the distance parallel to the optic axis with $\zeta = 0$ at the beam waist; $\ell \equiv L/2$ is half the length of LIGO's arm cavity (2 km) and is also equal to the beam's Rayleigh range; $b = \sqrt{\lambda L/2\pi} = \sqrt{\lambda\ell/\pi} = 2.603$ cm (with $\lambda = 1.064\mu$m, the light wavelength) is the radius at the $1/e$ point of the beam's *intensity* distribution at the ends of the cavity, i.e., at $\zeta = \ell$; and b is also the radius, at the $1/e$ point of the beam's *amplitude* distribution, at the beam's waist, $\zeta = 0$. Note that the last phase factor, $2\ell\zeta/b^2$, is actually $k\zeta$ in disguise, with $k = 2\pi/\lambda$ the light's wave number. We adjust λ or ℓ slightly so that at $\zeta = \ell$ and $\varpi = 0$, Ψ is real and positive; i.e., the sum of the last two phase factors is a multiple of 2π. Then in the immediate vicinity of the mirror plane, at $\zeta = \ell + \delta\zeta$ (with $|\delta\zeta| \ll b$), the minimal Gaussian has the simple form

$$\Psi(\varpi,\ell) = \exp\left[\frac{-\varpi^2(1-i)}{2b^2} + ik\delta\zeta\right] , \tag{2.2}$$

with $k = 2\ell/b^2$. (Here and throughout this paper we ignore fractional corrections of order $\lambda/b \sim b/\ell \sim 10^{-5}$.) The Mesa-beam (FM-beam) field, constructed by superposing minimal Gaussians as in Fig. 2.1a, is given by (Sec. IIA of [7])

$$U_0(r,z,D) = \int_{\mathcal{C}_D} \Psi(\sqrt{(x-x_o)^2+(y-y_o)^2}, z)\, dx_o dy_o . \tag{2.3}$$

Here, $r = \sqrt{x^2+y^2}$ is the radius from the cavity's central axis, the integral is over Cartesian coordinates (x_o, y_o) of the Gaussians' optic axes, and the integral extends over the interior of the disk, $\mathcal{C}_D$, with radius D, i.e., $\sqrt{x_o^2+y_o^2} \leq D$. The subscript 0 on U_0 is the value $\alpha = 0$ of the twist angle of the Gaussians' optic axes, when one regards this FM beam from the viewpoint of the

---

[1] By "minimal Gaussian beam" we mean the fundamental, TEM00 mode of an optical resonator with spherical mirrors, with the mirror radii of curvature adjusted so the Gaussian-shaped intensity distributions on the two mirrors are identical and have the minimum possible radii b at the $1/e$ point of the intensity distribution.

hyperboloidal family of beams (Sec. 2.4 below).

By inserting expression (2.2) with $\delta\zeta = 0$ into Eq. (2.3), we obtain for the FM beam at the mirror plane $z = \ell$,

$$U_0(r, \ell, D) = \int_{\mathcal{C}_D} \exp\left[\frac{-[(x-x_o)^2 + (y-y_o)^2][1-i]}{2b^2}\right] dx_o dy_o \ . \tag{2.4}$$

The mirror surface must coincide with a phase front of this Mesa beam (FM beam); i.e., it must have a shape $z = \ell + H_0(r)$ such that $\arg[U_0(r, \ell + H_0, D)] = \text{constant} = \arg[U_0(0, \ell, D)]$. In the vicinity of the mirror the phase of each minimal Gaussian varies as $k\delta\zeta = k\delta z$ [Eq. (2.2)], so $\arg[U_0(r, \ell + H_0, D)] = \arg[U_0(r, \ell, D)] + kH_0$, and the shape of the mirror surface must be

$$H_0(r) = k^{-1} \left\{\arg[U_0(0, \ell, D) - \arg[U_0(r, \ell, D)]\right\} \ . \tag{2.5}$$

By carrying out the integral (2.4) analytically in one dimension and then numerically in the other, and then inserting into Eq. (2.5), O'Shaughnessy and Thorne find the "Mexican-hat" mirror shape $H(r)$ shown as a solid line in Fig. 2.2.

To high accuracy, the field U_0 on the mirror surface differs from that on the plane $z = \ell$ only by the phase factor $e^{ikH_0(r)}$, so the intensity distribution on the mirror is the same as at $z = \ell$; i.e., it is

$$I_0(r) \propto |U_0(r, \ell, D)|^2 \ . \tag{2.6}$$

This intensity has the Mesa shape shown as a solid line in Fig. 2.3.

2.3 Mesa beams supported by nearly concentric mirrors (CM Beams; $\alpha = \pi$)

Our proposed Mesa beams with nearly concentric, spherical mirrors ("CM" beams) can be constructed by overlapping minimal Gaussians whose optic axes all pass through the center of the cavity [Fig. 2.1(c)], and are distributed uniformly inside a cone with angular radius $\Theta = D/\ell$.

It should be clear from this construction that the resulting Mesa beam will have a beam radius approximately equal to D at the mirrors ($z = \ell$), and approximately equal to b (the minimal Gaussian radius) at the cavity's center ($z = 0$). For advanced LIGO, D is approximately $4b$ [7], so the waist of this Mesa beam will be approximately four times narrower than the beam on the mirrors. This contrasts with a Mesa beam supported by nearly-flat mirrors (previous section), for which the waist is only slightly narrower than the beam on the mirrors.

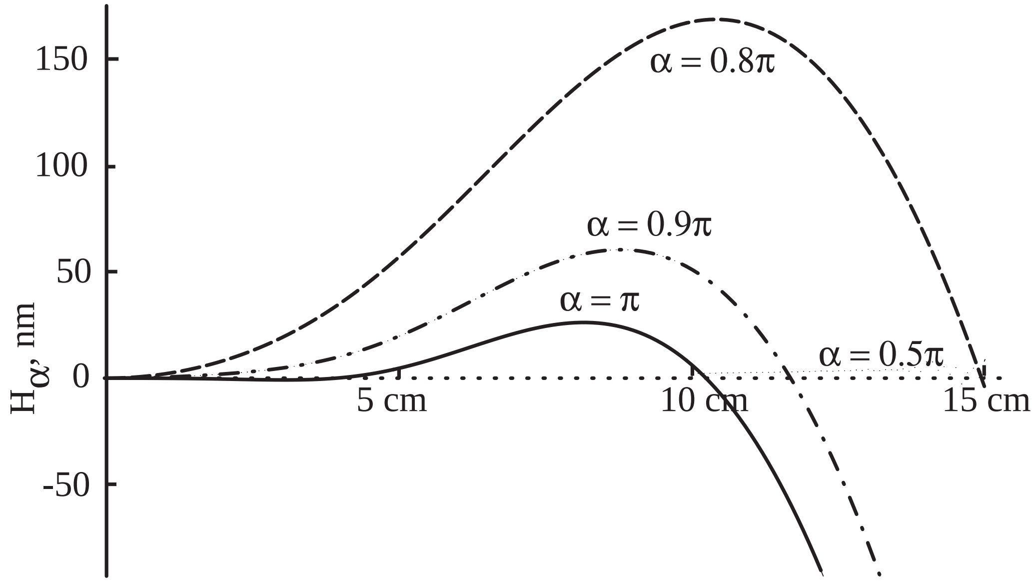

Figure 2.2: The correction $H_\alpha(r)$ to the mirror shape for hyperboloidal beams in a LIGO arm cavity ($L = 4$ km) with $D = 10$ cm and with twist angles α between $\pi/2$ and π. For $\alpha = 0$, the correction is the negative of that for $\alpha = \pi$; for $\alpha = 0.1\pi$ it is the negative of that for 0.9π; for any α between 0 and $\pi/2$, it is the negative of that for $\pi - \alpha$. For $\alpha = \pi$ (the Mexican-hat correction for our new CM Mesa beam), $H_0(r)$ drops to about -500 nm (half the wavelength of the light beam) at $r = 16$ cm (the mirror's edge). These corrections are added onto the fiducial spheroidal shape $S_\alpha(r)$ [Eq. (2.13)].

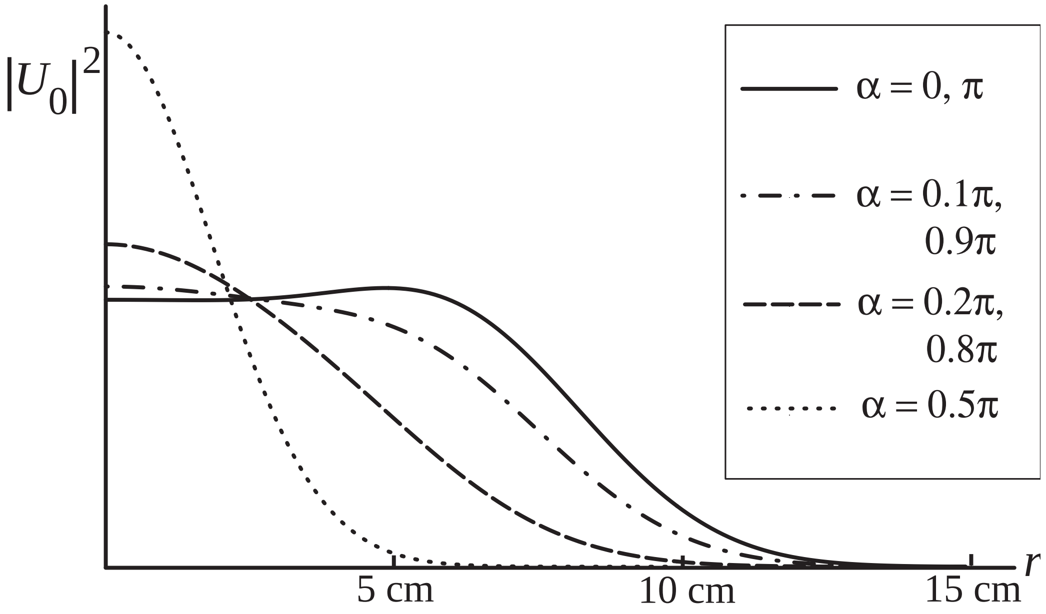

Figure 2.3: The light beam's un-normalized intensity $|U_\alpha|^2$ as a function of radius r on the mirror, for hyperboloidal beams in a LIGO arm cavity ($L = 4$ km) with $D = 10$ cm and various twist angles α. For $\alpha = 0$ and π, the intensity has the Mesa shape; for $\alpha = 0.5\pi$ it is a minimal Gaussian.

Near the mirrors, the phase fronts of this CM beam will be nearly concentric spheres centered on the point $(r, z) = (0, 0)$ through which the Gaussians' optic axes pass, so we shall evaluate the CM field as a function of radius r on this *fiducial sphere*,

$$z = S_\pi(r) \equiv \sqrt{\ell^2 - r^2} \simeq \ell - r^2/2\ell \ . \tag{2.7}$$

[Here and below we use a subscript π to denote Mesa-beam quantities with nearly concentric mirrors, i.e., CM quantities. This is because the minimal Gaussians used to generate the CM beam have twist angles $\alpha = \pi$; see Sec. 2.4.] For each minimal Gaussian, this fiducial sphere bends away from the Gaussian's transverse plane by an amount $\delta\zeta = -\varpi^2/2\ell$; so on this fiducial sphere the Gaussian's phase factor, $k\delta\zeta = (2\ell/b^2)\delta\zeta$, is equal to $-\varpi^2/b^2$. As a result, the Gaussian field on the fiducial sphere is [cf. Eq. (2.2)]

$$\begin{aligned} \Psi(\varpi, S_\pi) &= \exp\left[\frac{-\varpi^2(1-i)}{2b^2} + ik\delta\zeta\right] \\ &= \exp\left[\frac{-\varpi^2(1+i)}{2b^2}\right] \ . \end{aligned} \tag{2.8}$$

Correspondingly, these minimal Gaussians superpose on the fiducial sphere to produce a CM field given by

$$\begin{aligned} &U_\pi(r, S_\pi, D) = \\ &\int_{\mathcal{C}_D} \exp\left[\frac{-[(x-x_o)^2 + (y-y_o)^2][1+i]}{2b^2}\right] dx_o dy_o \ . \end{aligned} \tag{2.9}$$

Notice that this $U_\pi(r, S_\pi, D)$ is the complex conjugate of the FM field, $U_0(r, \ell, D)$, evaluated on the transverse plane $z = \ell$ (the fiducial surface for the case of nearly flat mirrors); see Eq. (2.4).

As for the nearly-flat (FM) case, the phase of the CM field will vary with distance δz from the fiducial sphere, nearly proportionally to $k\delta z$; and correspondingly, the mirror's surface, $\delta z = H_\pi(r)$ (a surface of constant phase), will be given by the analog of Eq. (2.5):

$$H_\pi(r) = k^{-1}\left\{\arg[U_\pi(0, S_\pi, D) - \arg[U_\pi(r, S_\pi, D)]\right\} \ . \tag{2.10}$$

Because $U_\pi(\varpi, S_\pi, D)$ is the complex conjugate of $U_0(\varpi, \ell, D)$, Eqs. (2.5) and (2.10) imply that

$$H_\pi(r) = -H_0(r) \ . \tag{2.11}$$

In words: To support Mesa beams with the same beam size, D, on their mirrors, the nearly-concentric mirrors and the nearly-flat mirrors must deviate from precisely concentric spheres, $z = S_\pi(r)$, and precisely flat planes, $z = \ell$, by equal and opposite displacements, $\delta z = H(r)$. This fact was discovered in numerical work by one of us (MB) and was later proved numerically in a much wider context by Savov [17] and analytically by Agresti, d'Ambrosio, Chen and Savov [18], before we found the above demonstration.

Because [to the accuracy of our analysis, $O(\lambda/b)$] the field U_π is the same, aside from phase, on the mirror surface as on the fiducial sphere, S_π, the light's intensity distribution is the same on the mirror as on S_π:

$$I_\pi(r) \propto |U_\pi(r, S_\pi, D)|^2 \ . \tag{2.12}$$

Moreover, because $U_\pi(r, S_\pi, D)$ is the complex conjugate of $U_0(r, \ell, D)$, both have the same moduli and intensity distributions; i.e., the CM beam has the same Mesa-shaped intensity distribution as the FM beam (solid curve in Fig. 2.3 below). This fact was discovered in numerical work by one of us (MB) and was later proved numerically in a much wider context by Savov [17] and analytically by Agresti, d'Ambrosio, Chen and Savov [18], before we found the above demonstration.

2.4 Hyperboloidal Beams Supported by Nearly Spheroidal Mirrors

One can smoothly transform FM beams into CM beams, and the in-between beams may be interesting for LIGO. In this section, we will focus on one way to make such a transformation.

We will first look at a smooth deformation of the geometric body formed by the optic axes of the minimal Gaussians that are used in constructing the FM and CM beams. For a FM beam, the axes of the minimal Gaussians lie on coaxial cylinders, while for CM beams they lie on coaxial cones. It is well-known that one can smoothly deform a cylinder into a cone as follows: The generators of a cylinder of height 2ℓ and radius r (Fig. 2.1a) are lines that join points with cylindrical coordinates $(r, \phi, -\ell)$ on the base circle to points (r, ϕ, ℓ) on the top circle. The generators of a symmetric cone of height 2ℓ and end radii r (Fig. 2.1c) are lines that join points $(r, \phi, -\ell)$ and points $(r, \phi + \pi, \ell)$. A path from the cylinder to the cone is given by a family of hyperboloids generated by lines that join points $(r, \phi, -\ell)$ and points $(r, \phi + \alpha, \ell)$ (Fig. 2.1b). For $\alpha = 0$, one obviously gets the cylinder, and for $\alpha = \pi$, the cone.

We therefore propose constructing a new two-parameter family of light beams, and the mirrors that support these beams, using the O'Shaugnessy-Thorne technique of superposing minimal Gaussians. The parameters are $\{\alpha, D\}$; and for given values of $\{\alpha, D\}$, the minimal Gaussians have their optic axes uniformly distributed on the hyperboloid generators that reach from $(r, \phi, -\ell)$ to $(r, \phi + \alpha, \ell)$ (Fig. 2.1b), with ϕ running from 0 to 2π and r confined to the interior of the disk, $\mathcal{C}_D$, $r \leq D$. For $\alpha = 0$, these *hyperboloidal beams* will be Mesa beams with nearly-flat mirrors, i.e., FM beams. For $\alpha = \pi$, they will be Mesa beams with nearly concentric mirrors; i.e., CM beams.

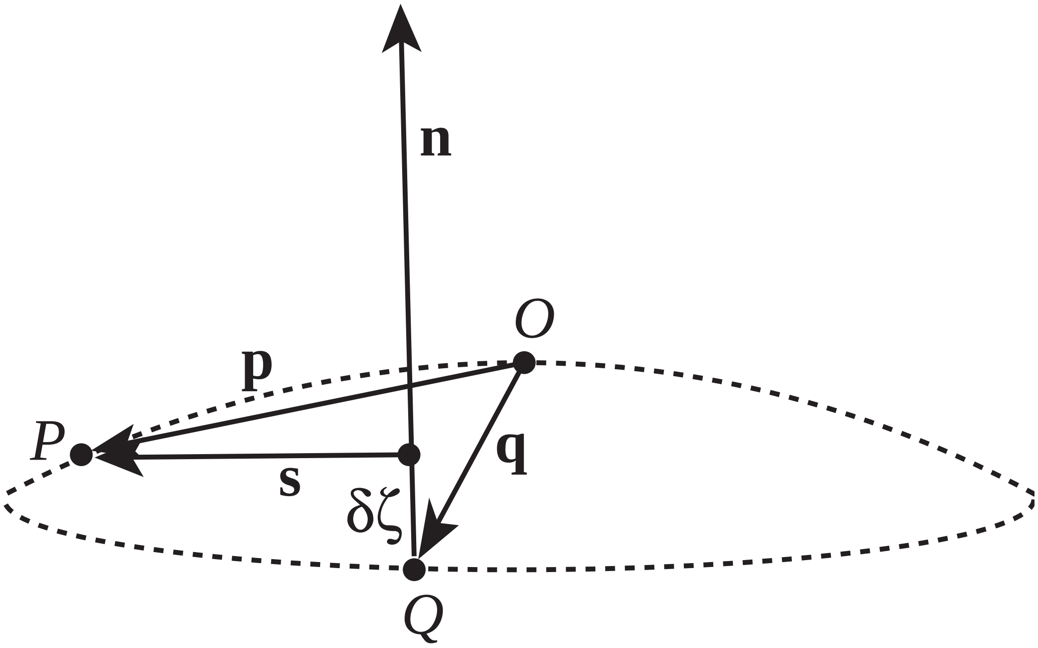

Figure 2.4: Geometric construction for computing the hyperboloidal field $U_\alpha(r, S_\alpha, D)$ on the fiducial spheroid S_α (a segment of which is shown dotted).

We can construct explicit expressions for the shapes of the mirrors that support these hyperboloidal beams, and expressions for the fields on those mirrors, by using the same method as in the FM case (Sec. 2.2) and the CM case (Sec. 2.3): Because the phase of each minimal Gaussian varies nearly proportionally to $k\zeta$, the surface of constant phase at the mirror location will be nearly the same as the "fiducial" surface obtained by cutting off each Gaussian's optic axis at $\zeta = \ell$. One can show that, with the optic axes being generators of hyperboloids, the surface formed by their ends at constant distance $\zeta = \ell$ from the cavity's mid point is the fiducial spheroid

$$z = S_\alpha(r) \equiv \sqrt{l^2 - r^2 \sin^2(\alpha/2)} \simeq \ell - \frac{r^2 \sin^2(\alpha/2)}{2\ell} \; . \tag{2.13}$$

We can compute our hyperboloidal field $U_\alpha(r, S_\alpha, D)$ on this fiducial spheroid by superposing our minimal Gaussians with the aid of Fig. 2.4. In this figure, P is the point on the spheroid, S_α, at which we wish to compute the field. The vector, $\mathbf{p}$, reaching from the spheroid's center point, O (the center of our hyperboloidal field's cross section), to P has Cartesian coordinates $\mathbf{p} = (r, 0, \mathcal{Z})$, where $\mathcal{Z} \equiv S_\alpha(r) - \ell = -(r^2/2\ell)\sin^2(\alpha/2)$. The optic axis of a minimal Gaussian, over which we will integrate, intersects S_α at the point Q, that has Cartesian coordinates $\mathbf{q} = (r_o \cos\phi_o, r_o \sin\phi_o, \mathcal{Z}_o)$, where $\mathcal{Z}_o = S_\alpha(r_o) - \ell = -(r_o^2/2\ell)\sin^2(\alpha/2)$. The optic axis of this minimal Gaussian points along the unit vector $\mathbf{n} = \{(r_o/2\ell)[\cos(\phi_o) - \cos(\phi_o - \alpha)], (r_o/2\ell)[\sin(\phi_o) - \sin(\phi_o - \alpha)], 1\}$. [Here as elsewhere we neglect corrections of order $r/\ell \sim r_o/\ell \sim b/\ell \sim \lambda/b \sim 10^{-5}$.] The vector $\mathbf{s} =$

$\mathbf{p}-(\mathbf{q}+\mathbf{n}\delta\zeta)$ reaches orthogonally from the minimal Gaussian's optic axis to point P. The length of this vector is the radius ϖ of P as measured in cylindrical coordinates centered on the minimal Gaussian's optic axis,

$$\varpi = |\mathbf{s}| \simeq |\mathbf{p}-\mathbf{q}| = \sqrt{r^2 + r_o^2 - 2rr_o\cos\phi_o}\ , \tag{2.14}$$

where the second expression, accurate to $O(\lambda/b)$, can be deduced from the above equations. The distance $\delta\zeta$ along the optic axis $\mathbf{n}$, at which the normal $\mathbf{s}$ intersects the axis, is determined by the orthogonality relation $\mathbf{s}\cdot\mathbf{n}=0$:

$$\delta\zeta = \mathbf{n}\cdot(\mathbf{p}-\mathbf{q}) = \frac{-1}{2\ell}\left[\varpi^2\sin^2\left(\frac{\alpha}{2}\right) + rr_o\sin\alpha\sin\phi_o\right]\ . \tag{2.15}$$

The field $U_\alpha(r, S_\alpha, D)$ on the spheroid S_α is obtained by adding up the minimal Gaussians (2.2) with ϖ and $\delta\zeta$ given by Eqs. (2.14) and (2.15), and with $k = 2\ell/b^2$, and by then doing some simple algebra:

$$\begin{aligned} U_\alpha(r, S_\alpha, D) = \textstyle\int_0^D r_o\, dr_o \int_0^{2\pi} d\phi_o \exp\Big[i\tfrac{rr_o}{b^2}\sin\phi_o\sin\alpha \\ -\tfrac{(r^2+r_o^2-2rr_o\cos\phi_o)}{2b^2}(1-i\cos\alpha)\Big]\ . \end{aligned} \tag{2.16}$$

The radial integral can be carried out analytically yielding an expression involving error functions, and the angular integral can then be done numerically.

The field (2.16) cannot be sensitive to the chirality of the optic axes' twist, i.e., to the sign of α, since it is a scalar complex function of r: $U_{-\alpha} = U_\alpha$. This tells us that *the relevant range for* α *is* 0 *to* π. Replacing α by $\pi-\alpha$ and changing the sign of α is equivalent to complex conjugating U_α; therefore:

$$U_{-\alpha} = U_\alpha\ ; \quad U_{\pi-\alpha} = U_\alpha^*\ . \tag{2.17}$$

For $\alpha = 0$, the fiducial spheroid, $S_0(r)$, is the transverse plane, and the field (2.16) is the FM Mesa beam U_0 [Eq. (2.4)]. For $\alpha = \pi/2$, the fiducial spheroid, $S_{\pi/2}$, is a sphere of radius $R = L = 2\ell$ (the distance between the mirrors), and both the radial and the angular integrals can be carried out analytically, giving for the field on that sphere

$$U_{\pi/2} = \text{constant}\exp\left[-r^2/2b^2\right]\ ; \tag{2.18}$$

this is precisely the minimal Gaussian beam [Eq. (2.2) with $\varpi = r$, evaluated at $k\delta\zeta = -kr^2/2R = -(2\ell/b^2)r^2/4\ell = -r^2/2b^2$]. For $\alpha = \pi$, the fiducial spheroid, $S_\pi(r)$, is a sphere with radius $\ell = L/2$, and the field (2.16) is the CM Mesa beam [Eq. (2.9)]. Thus, as α varies from 0 to π, U_α deforms continuously from the FM Mesa beam, $\alpha = 0$, through a set of hyperboloidal beams to a minimal Gaussian at $\alpha = \pi/2$, and on through another set of hyperboloidal beams to the CM Mesa beam,

$\alpha = \pi$.

As for the FM and CM beams, so also for the hyperboloidal beam (2.16) and for the same reasons: The mirror's surface must be displaced longitudinally from the fiducial spheroid, $z = S_\alpha(r)$, by $\delta z = H_\alpha(r)$, where

$$H_\alpha(r) = k^{-1} \left\{ \arg[U_\alpha(0, S_\alpha, D) - \arg[U_\alpha(r, S_\alpha, D)] \right\} \ . \tag{2.19}$$

This equation and $U_{\pi-\alpha} = -U_\alpha^*$ [Eq. (2.17)] tell us that

$$H_{\pi-\alpha}(r) = -H_\alpha(r) \ . \tag{2.20}$$

This is a special case of a duality relation discovered numerically by Savov and Vyatchanin [17] and proved analytically by Agresti, d'Ambrosio, Chen and Savov [18]. Figure 2.2 shows these mirror shape corrections for various α's. The light intensity on the mirrors is given by the obvious analog of Eqs. (2.6) and (2.12):

$$I_\alpha(r) \propto |U_\alpha(r, S_\alpha, D)|^2 \ . \tag{2.21}$$

This equation and $U_{\pi-\alpha} = -U_\alpha^*$ [Eq. (2.17)] tell us that

$$I_{\pi-\alpha}(r) = I_\alpha(r) \ . \tag{2.22}$$

This is another special case of the duality relation discovered by Savov and Vyatchanin [17], and proved analytically by Agresti, d'Ambrosio, Chen and Savov [18].

The intensity distribution (2.21) is shown in Fig. 2.3, for fixed $D = 10$ cm and various α. To minimize thermal noises, one wants the largest beam compatible with acceptable diffraction losses. In this spirit, in Fig. 2.5 we compare hyperboloidal beams with fixed diffraction losses (as computed in the clipping approximation) rather than with fixed D.

2.5 Conclusions

For twist angles α near 0 and π, the hyperboloidal beams introduced in this paper have the flat-top form needed to reduce thermoelastic noise in LIGO. The radius of the flat top is largest for $\alpha = 0$ and $\alpha = \pi$ (the FM and CM Mesa beams) and smallest for $\alpha = \pi/2$ (the minimal Gaussian).

Because the mirrors are most nearly flat or concentric for the Mesa configurations, $\alpha = 0$ or π, those configurations are most nearly optically unstable. (Near instability goes hand in hand with large beams on the mirrors, which are needed to control thermoelastic noise.)

The results of Savov and Vyatchanin [18] suggest that the tilt instability is smallest for $\alpha = \pi$ and worst for $\alpha = 0$.

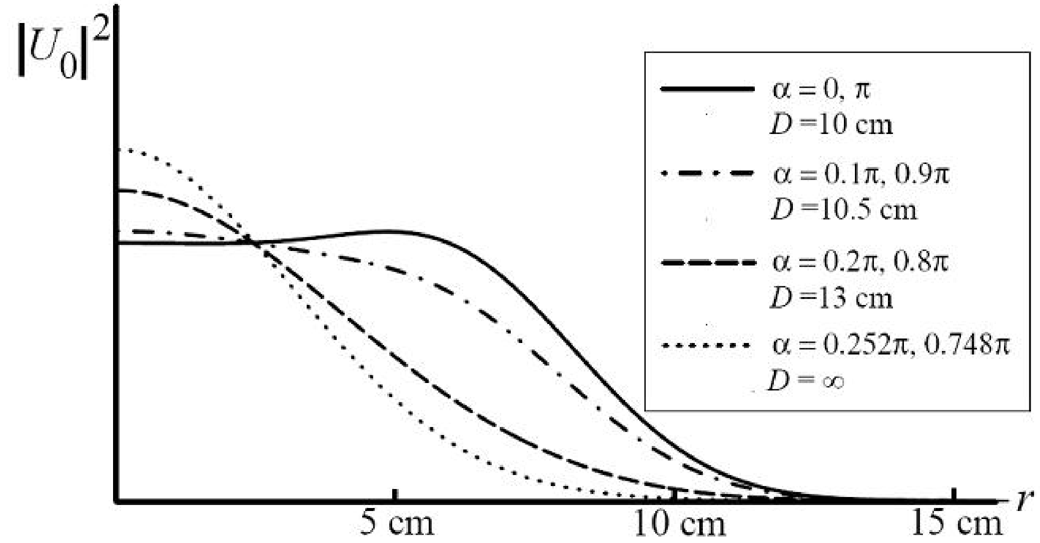

Figure 2.5: The light beam's un-normalized intensity $|U_\alpha|^2$ as a function of radius r on the mirror, for hyperboloidal beams in a LIGO arm cavity ($L = 4$ km) with fixed diffraction losses: 2.68 ppm in the clipping approximation, assuming mirror radii of 16 cm. The Mesa beam ($\alpha = 0$) has $D = 10$ cm and is identical to that of Fig. 2.3. For $\alpha = 0.1\pi$, to keep the diffraction losses at 2.68ppm, D has been increased to 10.5 cm and the physical beam diameter is, correspondingly, a bit larger than in Fig. 2.3. For $\alpha = 0.2\pi$, D has been increased to $D = 13.0$ cm; for $\alpha = 0.252\pi$, it has been increased to $D = \infty$, producing a beam shape that is Gaussian to the accuracy of our numerical computations, but is substantially larger than the minimal Gaussian of Fig. 2.3 and is approximately the same as the baseline design for advanced LIGO. (Our numerical computations suggest that for $D = \infty$ and all $\alpha \neq 0$ or π, the hyperboloidal beam is Gaussian, with width varying from minimal, $\sigma = b = \sqrt{\lambda L/2\pi}$ at $\alpha = \pi/2$ to $\sigma \to \infty$ as $\alpha \to 0$ or π, but we have not been able to prove this analytically.)

These considerations suggest that the optimal configuration for advanced LIGO will be near $\alpha = \pi$, but whether the optimum is precisely at $\alpha = \pi$ (the CM configuration) or at some modestly smaller α will depend on practical and thermal-noise considerations not examined in this paper.

2.6 Acknowledgments

We thank Pavlin Savov, Juri Agresti, Erika D'Ambrosio, Yanbei Chen, Geoffery Lovelace, and Poghos Kazarian for useful discussions and advice. MB thanks Manuela Campanelli and the University of Texas at Brownsville, and Ed Seidel, Gabrielle Allen and the Center for Computation and Technology at Louisiana State University for helpful discussions and travel support during this research. This research was supported in part by NSF Grants PHY-0099568 and PHY-0601459.

Bibliography

[1] M. Bondarescu and K. S. Thorne, “A new family of light beams and mirror shapes for future LIGO interferometers,” Phys. Rev. D **74**, 082003 (2006) arXiv:gr-qc/0409083.

[2] LIGO http://www.ligo.caltech.edu/ , as of May 10 2007 .

[3] J. Sidles and D. Sigg, LIGO Report T0301320-00 (2003), URL `http://www.ligo.caltech.edu/docs/T/T030120-00.pdf`.

[4] J. Sidles and D. Sigg, ”Optical torques in suspended Fabry Perot interferometers” Phys. Lett. A **354**, 167 (2006).

[5] K.S. Thorne, “Thermoelastic Noise in LIGO II,” LIGO Report G000068-00-D (2000), URL `http://www.ligo.caltech.edu/docs/G/G000068-00.pdf`.

[6] E. D’Ambrosio, R. O’Shaughnessy and K.S. Thorne, “Beam Reshaping to Reduce Thermoelastic Noise,” LIGO Report G000223-00-D (2000), URL `http://www.ligo.caltech.edu/docs/G/G000223-00.pdf`.

[7] E. D’Ambrosio, R. O’Shaugnessy, S. Strigin, K.S. Thorne, and S. Vyatchanin, “Reducing Thermoelastic Noise in Gravitational-Wave Interferometers by Flattening the Light Beams,” Phys. Rev. D, submitted; gr-qc/0409075.

[8] R. O’Shaunessy, S. Strigin and S. Vyatchanin, “The implications of Mexican-hat mirrors: calculations of thermoelastic noise and interferometer sensitivity to perturbation for the Mexican-hat-mirror proposal for advanced LIGO,” Phys. Rev. D, submitted; gr-qc/0409050 .

[9] J. Agresti, LIGO Technical Report T040225-00-R; ”Researches on Non-Standard Optics for Advanced G.W. Interferometers.” URL `http://www.ligo.caltech.edu/docs/T/T040225-00.pdf`.

[10] J. Agresi and R. DeSalvo, ” Flat-Topped Beam Cavity Prototypes” LIGO-G050041-00-Z; URL `http://www.ligo.caltech.edu/docs/G/G050041-00`.

[11] J. Agresti, paper in preparation.

[12] G. Lovelace, “The dependence of test-mass coating and substrate thermal noise on beam shape in the advanced laser interferometer gravitational-wave observatory (advanced LIGO),” [arXiv:gr-qc/0610041].

[13] E. D’Ambrosio, “Nonspherical mirrors to reduce thermoelastic noise in advanced gravitational wave interferometers,” Phys. Rev. D **67**, 102004 (2003).

[14] J. Agresti, E D’Ambrosio, R. DeSalvo, Danielle Forest, Patrick Ganau, Bernars Lagrange, Jean-Marie Mackowski, Christophe Michel, John Miller, Jean-Luc Montorio, Nazario Morgado, Laurent Pinard, Alban Remillieux, Barbara Simoni, Marco Tarallo, Phil Willems, ”The Mesa Beam”, LIGO Report G050522-00-Z (2005), URL `http://www.ligo.caltech.edu/docs/G/G050522-00/G050522-00.pdf`.

[15] P.T. Beyersdorf, S. Zappe, M.M. Fejer and M. Burkhardt, paper in preparation.

[16] S. Vyatchanin, LIGO Report Number T030272-00 (2003), ”Estimate of Angular Instability for Mexican-Hat and Gaussian Modes of a Fabry-Perot Interferometer” URL `http://www.ligo.caltech.edu/docs/T/T030272-00.pdf`.

[17] S. Vyatchanin and P. Savov, ”Estimate of Tilt Instability of Mesa-Beam and Gaussian-Beam Modes for Advanced LIGO” Phys.Rev. D74 (2006) 082002; gr-qc/0409084.

[18] P. Savov, E. D’Ambrosio, Y. Chen, J. Agresti, ”A duality relation between non-spherical optical cavities and its application to gravitational-wave detectors” Phys. Rev. D, submitted; gr-qc/0511062.

Chapter 3

Optimal Light Beams and Mirror Shapes for Future LIGO Interferometers

Advanced LIGO's present baseline design uses arm cavities with Gaussian light beams supported by spherical mirrors. Flat-topped light beams (*Mesa Beams*) have been considered as an alternative that lowers thermal noise by a factor of three.

The research reported here is devoted to finding the beam and mirror shapes that would lower thermal noise the most. We wanted to see how far we can go and how much we can improve the sensitivity of LIGO by reshaping the mirrors.

We use a minimization algorithm to search for the beam with the lowest thermal noise in the space of all possible beams.

The result of this minimization is a beam with thermal noise a factor of two (in power) [1] lower than previously consider *Mesa Beams* and a factor of six (in power) lower than the Gaussian beams employed in the current baseline design. If this beam can be successfully implemented in LIGO, and noises other than the thermal noise considered here remain unchanged, the event rate of the instrument will increase roughly by a factor of three in the frequency range of maximum sensitivity. In this frequency range, the thermal noise is the dominant noise source. Lowering it will not only increase LIGO's event rate and thus our chances of seeing gravitational waves, but it will also bring LIGO closer to probing the quantum limit, and, thus, for the first time, LIGO can study quantum effects as experienced by 40-kilogram objects.

In Figure 3.1, we show the LIGO noise budget and the important role internal thermal noise plays in limiting the instrument sensitivity. The sensitivity of Initial LIGO, also shown in this figure, is not high enough to benefit from internal thermal noise reduction. However, Initial LIGO has a higher internal thermal noise, and will be upgraded soon; we then might actually see coating

---

[1] The exact numbers for all types of noise are given in Table 3.1.

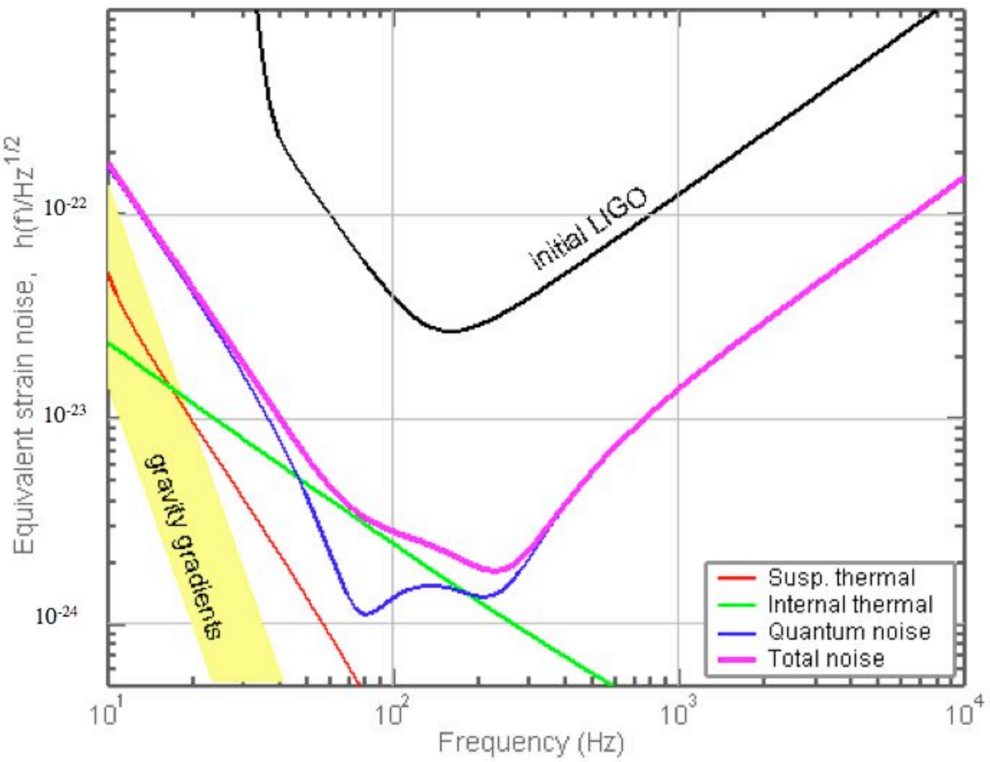

Figure 3.1: Advanced LIGO noise budget. Internal Thermal Noise is the dominant noise source in the maximum frequency range (40-200 Hz.)

thermal noise. Employing the technology developed here in an interferometric gravitational waves detector comparable to Initial LIGO would thus provide little or no benefits. Enhanced LIGO may be sensitive enough to see coating thermal noise and then this work might provide a small benefit. In any case, technology involved here will be developed in a longer time scale, beyond that of initial LIGO.

3.1 Noise Characterization

This work was made possible by a better understanding of thermal noise recently published [4]. In [4], Lovelace summarized and extended previous results, thus making it possible for us to employ little computational power to estimate the thermal noise many times as required in a numerical minimization process. This section briefly reviews the main results of Lovelace, which will be the basis of our work. He assumes half-infinite mirrors, i.e. he neglects all effects arising from a mirror's finite thickness as well as mirror edge effects, and also ignores the dynamics of the mirror, e.g., by using the quasi-static approximation.

LIGO extracts the gravitational wave signal by measuring the position of the mirrors. The position information is read as $q(t)$, a weighted average of the mirror's longitudinal position, which depends on $Z(r, \phi, t)$, as follows:

$$q(t) \equiv \int_0^{2\pi} d\phi \int_0^R dr r p(r) Z(r, \phi, t) \tag{3.1}$$

where Z is the displacement of the mass element at (r, ϕ) of the mirror surface, R is the mirror radius, and $p(r)$ is the light intensity of the axisymmetric beam at distance r from the optical axis.

Internal thermal noise will cause small fluctuations in the longitudinal position of the mirror, $Z(r, \phi, t)$.

Internal thermal noise can be divided into two different types: Brownian and Thermoelastic. Brownian thermal noise is due to imperfections in the substrate r coating material that couples normal modes of vibration to each other. Thermoelastic noise is due to random heat flow in the mirror that causes some regions to expand and some to contract.

Both noises arise from the substrate as well as from the mirror coating. Thus, we have to deal with four types of noise: Coating Brownian noise, Coating Thermoelastic noise, Substrate Brownian noise and Substrate Thermoelastic noise.

Gillespie and Raab used normal-mode decomposition to calculate the Brownnian thermal noises [5]. Yuri Levin [6] developed this alternative approach using Fluctuation Dissipation Theorem (FDT), which is easier and more intuitive. It also leads to the scaling laws discovered by Geoffrey Lovelace [4].

The spectral density, S, of the fluctuations in the measured mirror position, q, is derived from the Fluctuation Dissipation Theorem using Levin's thought experiment [6]:

$$S = \frac{2k_B T W_{diss}}{\pi^2 f F^2}, \tag{3.2}$$

where k_B is Boltzmann's constant, T is the mirror temperature, and W_{diss} is the dissipated power if a longitudinal force F is applied to the mirror surface with frequency f and pressure profile $p(r)$.

In initial LIGO, to keep diffraction losses under 1 ppm per bounce, the beam radius over which 95% of the signal is collected is kept significantly smaller than the mirror radius, R, and mirror thickness, H. Lovelace was forced to use infinite test-mass approximation because the non-infinite case is too difficult to solve analytically and will not give a simple scaling law. He later showed that the infinite test mass approximation holds reasonably well for beams considerably larger than in initial LIGO.

Fused silica is found to be significantly less susceptible to the mirror edge effects and finite effects due to the finite thickness of the mirror than sapphire substrate.

By using his results, we make the same assumptions in computing the noise. The condition that 95% of the signal is collected from a mirror area smaller than R is very true in the case of Gaussian beam, almost true in the case of Mesa beams and almost false in the case of the conical beams proposed here.

Because the resonant frequencies of the mirror are of order 10^4 Hz, far higher than the $40 - 200$ Hz gravitational waves frequencies measured in LIGO, the hypothetical force, F, can be idealized as quasi- static when computing the resulting strain of the mirror. Advanced LIGO will measure from 10 Hz to 10 kHz; however, thermal noise may only be dominant from 40Hz to 200 Hz.

Thus, to compute the noise S, Lovelace [4] substitutes in Eq. 3.2 the Brownian and Thermoelastic dissipated power, W_{diss}, due to a mirror deformation with the same pressure distribution as $p(r)$, the light intensity. This entire procedure is based on Levin's thought experiment [6, 2].

The thermally induced gravitational wave strain noise power, $S_h(f)$, is related to S by

$$S_h = \frac{4}{L^2} S \tag{3.3}$$

because the interferometer measures

$$h = \frac{(q_1 - q_2) - (q_3 - q_4)}{L}, \tag{3.4}$$

where q_i is the measured position of the i^{th} mirror and $L = 4km$, the arm cavity length.

In the case of Gaussian beams, thermal noise overall was first understood in the LIGO context in [7, 8, 9]. In addition, Gillespie and Raab [5] were the first to calculate Substrate Brownian noise, using modal decomposition method.

The dependence of thermal noise on beam shape, for arbitrary beam shapes was addressed as follows: O'Schaughnessy [10] and Vyatchanin [11] proposed a simple scaling law for Coating Brownian noise mirrors idealized as infinitely large and thick. In the same paper, O'Schaunessy [10] put forward scaling laws for Coating Thermoelastic, Substrate Brownian, and Substrate Thermoelastic noises. O'Schaunessy, Strigin and Vyatchanin [12] derived a scaling law for Substrate Thermoelastic noise and Vinet [13] found the Substrate Thermoelastic noise scaling law.

Lovelace [4], building on the work mentioned above, clearly presented and verified the scaling laws for all noises. These simple scaling laws make it easy to estimate the change in thermal noise caused by changing the shape of the laser beeam.

To summarize the above papers in a single formula, different noise components depend on the beam shape as follows – and this is Eq. (3.1) of Lovelace [4]:

$$S_n = A \int_0^\infty dk\ k^n |\tilde{p}(k)|^2, \tag{3.5}$$

where $n = 1$ for Coating Brownian and Coating Thermoelastic noise, $n = 0$ for Substrate Brownian noise, $n = 2$ for Substrate Thermoelastic noise, A is a constant that depends on the noise type and instrumental setup but does not change with the beam shape, and $\tilde{p}(k)$ is the two-dimensional Fourier transform of the power distribution over the mirror surface, $p(r)$:

$$\tilde{p}(k) = \int_0^\infty dr\ r J_0(kr) p(r) \tag{3.6}$$

$$p(r) = \int_0^\infty dk\ k J_0(kr) \tilde{\tilde{p}}(k) \tag{3.7}$$

In the above, $J_0(x)$ is the 0^{th} order Bessel function of the first kind.

In the case of coating Brownian and Thermoelastic noises, we have $n = 1$, which converts directly to

$$S_1 \sim \int_0^\infty dr\ r |p(r)|^2 \tag{3.8}$$

according to the Parseval Theorem.

This makes numerical evaluation of these noises easiest in the context of a minimization code that requires noise to be computed a large number of times.

In fused silica mirrors, the leading choice for Advanced LIGO, coating noise is also the dominant type of internal thermal noise.

3.2 The Minimization Problem

3.2.1 Radiation in a Cavity - Generalities

Following a series of mental steps will bring us to the level of approximation at which we will be working.

Step 1: Scalar approximation

The following narrative is intended to walk us through a series of logical steps that lead into what is called a "scalar approximation" beyond an inexact statement that "we choose to work with E_x and E_y components of electric fields." What we need to know is the distribution of radiation pressure over the mirror, which is proportional to the intensity, I, that in turn is extracted from the knowledge of electric and magnetic fields, $\mathbf{E}$ and $\mathbf{B}$ respectively. For monochromatic light it is, from the theory of electromagnetism,

$$I = \frac{2}{4\pi} \left| \langle \mathbf{E} \times \mathbf{B} \rangle \right| , \tag{3.9}$$

where the average is over a period of the wave. It has been stated in Born and Wolf (BW) [14] that in problems involving "passage of light through an optical instrument of moderate aperture and of conventional design" there exists a complex scalar function U, such that

$$I = C \left| U \right|^2 , \tag{3.10}$$

where C is some complicated function of the properties of the source and the optical instrument. However, given that the relevant quantity often is a *relative* intensity (this is the case in our minimization problem in particular), an effective intensity can simply be defined as $I = \left| U \right|^2$. One way to introduce a scalar field is to first realize that under paraxial approximation, electric and magnetic fields are approximately perpendicular to the optical axis z. Furthermore, let's assume that electric field is polarized along the x-axis, and to simply consider the propagation equation for E_x. This field simply obeys the vacuum Maxwell's Equation $\nabla^2 E_x = \frac{1}{x^2}\ddot{E}$. However, a reader may find this argument imprecise unless the approximation that was made (that the field is approximately perpendicular to the z-axis) is made more rigorous. BW offered one pedagogical argument meant to guide one to believe that there indeed there exists a scalar function U from which $I = |U|^2$. In brief, their argument is as follows. First, they considered a situation of a generic optical instrument with an optical axis (the z-axis). They imagined that the light that enters the optical instrument is generated by an oscillating dipole at point P_0 (which does not have to be exactly on the optical axis, but not too far from it so that small angle approximations, also known as "paraxial approximations," can be used), and that there is an observation point, P, beyond the exit aperture of the optical instrument. Then the function U is given by

$$U(x,y,z,\omega) = \frac{\omega}{2\pi ic}\int_{\mathcal{A}} \frac{1}{s} e^{i\frac{\omega}{c}\left[\mathcal{L}(x',y',z')+s\right]}\, d\mathcal{A}. \tag{3.11}$$

Here $\mathcal{L}$ is the optical path length between the source of light and the point (x',y',z') on the exit aperture, and s is the length between the observation point, P, and a point (x',y',z') on the exit aperture. In this particular expression, it was assumed that P lies far enough from the exit aperture along the z-directon, and does not lie far off from the optical axis. Within this approximation, the distance, s, can also be replaced by a constant over the exit aperture, although if these assumptions are dropped, U would be given by a more complicated expression.

A more complicated light source can be thought of as a superposition of oscllating dipoles, and because the problem is linear, an expression for the appropriate scalar field would be built as a linear superposition of U (given above), with each piece of the light source contributing its own $\mathcal{L}$. Also, an optical resonator can be thought of as a semi-infinite optical device, built out of replicas of the resonators stacked together in series. Therefore, we have convinced ourselves that for the purposes of calculating the intensity, there exists an appropriate scalar field, $U(x,y,z,\omega)$. The problem is now reduced to understanding how this scalar field propagates.

Step 2: Fresnell-Kirchoff theory of scalar field distribution

The next step is to note that U satisfies an appropriate wave equation. BW showed that in their simple example

$$U(x,y,z,\omega)f(\omega) = \frac{1}{\sqrt{2\pi}}\int_{-T}^{T} E_x(x,y,z,t)e^{i\omega t}\, dt, \tag{3.12}$$

or, equivalently,

$$U(x,y,z,\omega)g(\omega) = \frac{1}{\sqrt{2\pi}}\int_{-T}^{T} E_y(x,y,z,t)e^{i\omega t}\, dt. \tag{3.13}$$

(Also, similar expressions can be written for B_x and B_y). Here functions $f(\omega)$ and $g(\omega)$ are related in a complicated way based on the positions of the source and the optical instrument. Also, it is assumed that the radiation exists only for the period of time between $-T$ and T, but then the limit $T \to \infty$ can be taken. Notice that

$$\nabla^2 U(x,y,z,\omega) = -\frac{\omega^2}{c^2}U(x,y,z,\omega), \tag{3.14}$$

and $f(\omega)$ can be cancelled. We also know that if a quantity $\phi(x,y,z,t)$ obeys the wave equation in space and time, $\nabla^2\phi = \frac{1}{c^2}\ddot{\phi}$, then its Fourier Transform will obey $\nabla^2\tilde{\phi} = -\frac{\omega^2}{c^2}\tilde{\phi}$. By comparison, we see that U obeys the wave equation. Henceforth, it enjoys all the properties that solutions to wave equations enjoy. For example, it can be shown (see, for example, Fox and Li [15]) that when a distribution of scalar field at an aperture is known, then the subsequent scalar field at a point, P, beyond an aperture is given by

$$U(P) = \frac{ik}{4\pi}\int_{\mathcal{A}} U(x',y',z')\frac{e^{-ikR(x',y',z')}}{R(z',y',z)}(1+\cos\theta)\,d\mathcal{A}. \tag{3.15}$$

Again, the integration is over the exit aperture. Here, R is the distance from the point on the aperture to the observation point, P. BW [14] give a rigorous derivation of a similar result, with a point source that follows certain small-angle approximations. A general expression such as given here then follows, due to the principle of superposition.

3.2.2 Normal Modes

If an eigen-mode sets up in an optical cavity, then as light bounces back and forth between mirrors, upon a single bounce from one mirror to the adjacent one, the field distribution will change at most by a complex constant λ, which includes the effects of energy loss and a net phase shift. Hence, $U_{q+1} = U_q/\lambda$, where q is a counter of the number of reflections from either mirror. This gives a general method, first employed by Fox and Li [15], to calculate eigen-modes of a cavity by solving the equation

$$U = \lambda\int_{\mathcal{A}} KU\,d\mathcal{A}, \tag{3.16}$$

where the propagator K is given by $\frac{ik}{4\pi R}(1+\cos\theta)e^{-ikR}$. Note that the assumption was made that both mirrors are identical. If the mirrors are different, then an eigen-equation would be written for propagation "there and back," obviously with a different propagator (not to be mentioned here). The normal modes enjoy an orthogonality property, although not a completeness property [16]. In this work, we expand the scalar field in the so-called "Gauss-Laguerre" modes [25], which is an orthonormal and complete basis. Under paraxial approximation, these modes are eigenmodes of a confocal spherical cavity (not necessarily our cavity), with infinite mirrors:

$$\Psi_n(z,r) = \frac{1}{\omega\sqrt{1+\left(\frac{z}{z_o}\right)^2}}\psi_n\left(\frac{\sqrt{2}r}{\omega\sqrt{1+\left(\frac{z}{z_o}\right)^2}}\right)e^{i\left(-(2n+1)\arctan\left(\frac{z}{z_0}\right)\right)}, \tag{3.17}$$

where $\psi_n(r) = Ce^{-r^2/2}\mathcal{L}_n(r^2)$ and $\mathcal{L}_n$ is n-th Laguerre Polynomial. Also, $z_0 = L/2$, where $L \approx 4km$, the length of the LIGO arm cavity and $z = 0$ is defined to be 0 in the middle of this arm cavity. Note that all our conditions are evaluated at $z = \pm L/2$ (i.e., the locations of the mirrors). Also note that these basis functions are real-valued at when $z = 0$, and that this is a complete basis for all real-valued functions. This is not coincidental, but has to do with the following argument.

We first assume our mirrors and arm cavities to be infinite, and construct modes of infinite-mirror arm cavities using two identical (but non-spherical) mirrors facing each other. Because the cavities are infinite, eigenmodes must be formed by two identical but counter-propagating waves, forming a standing-wave pattern. This pattern is invariant under time-reversal symmetry . (This is very false for a finite arm cavity, because cavity loss breaks time-reversal symmetry, by allowing some light to escape.) The scalar field that we expand in Ψ-modes is now one of the counter-propagating components. Because of the time-reversal symmetry, the phase front of this component going through $z = 0$ on the optical axis must be orthogonal to the optical axis, and therefore coincides with the $z = 0$ plane. For this reason, this component must be expandable by a set of modes that are real-valued at $z = 0$, since the phase distribution over the $z = 0$ plane is a constant and can thus be set to zero! Since we also require axisymmetry, we use the $n = 0$ Gauss-Laguerre modes. After obtaining the mode, we *prescribe* the mirror as phase fronts at $z = \pm L/2$. If the mirrors were infinite, then the mode will indeed be supported by this pair of mirrors. If the mirrors were finite, then we estimate the loss of the actual mode as the "clipping loss" of the current beam.

3.2.3 Minimizing The Coating Noise – Statement of The Problem

One strategy for calculating the eigenmode of the arm cavity is to solve the integral eigen-equation (3.16). This will be pursued in Section 3.4.5. At present our goal is to calculate such eigen-mode of light inside laser arms, the phase fronts of which at $z = \pm L/2$ (and hence the mirror shape) will turn out to be such that will minimize certain types of noise in the mirrors mentioned in Section 3.2. As already stated, given the shape of the mirror, the coating noise is given by $\int_0^\infty rp^2(\pm L/2, r)\, dr$, where the intensity field is given by $p(r) = |U(\pm L/2, r)|^2$, with U being the scalar field. Therefore, the noise is a functional of this scalar field. The objective in this part of the project is to minimize this functional, denoted by $\mathcal{N}$, with respect to U:

$$\mathcal{N} = \int_0^\infty 2\pi r |U(\pm L/2, r)|^4\, dr, \tag{3.18}$$

hence, solving for the scalar field, U. However, there are two additional constraints: The first constraint is simply a normalization requirement:

$$\int_0^\infty 2\pi r |U(\pm L/2, r)|^2\, dr = n = 1, \tag{3.19}$$

and the second constraint is the so-called "clipping approximation" that state that the loss of light outside of the mirror edge (at $r = R$) must be some given value (10^{-6} in this problem). So the second constraint is

$$\int_R^\infty 2\pi r|U(\pm L, 2, r)|^2\, dr = \eta = 10^{-6}. \tag{3.20}$$

We will expand the field U in the Ψ-basis stated in the previous section

$$U(z,r) = \sum_{n=0}^{\infty} a_n \Psi_n(z,r). \tag{3.21}$$

Recall that Ψ_n at $z = 0$ are real. We re-iterate that for the mode to resonate in a *symmetric* arm cavity, we need $U(r, z = 0)$ to be real-valued (but it may not be real at other zs). Hence all the coefficients a_n are *real*. In terms of this expansion, the normalization constraint becomes

$$\sum_{n=0}^{\infty} a_n^2 = n = 1, \tag{3.22}$$

and the loss constraint becomes

$$\sum_{n,m} a_n a_m \int_R^\infty r\Psi_n(z,r)\Psi_m(z,r)\, dr = \eta = 10^{-6}. \tag{3.23}$$

3.2.4 Gradient Flow with Constraint

The minimization will proceed along the path of "gradient descent" in the space of coefficients $\{a_n\}$. From some initial condition, $\mathbf{a}_0$, the minimization will proceed as a series of steps, with $\mathbf{a}_{j+1} = \mathbf{a}_j + \delta\mathbf{a}$. To first order, this $\delta\mathbf{a}$ can be calculated as follows: First, perform a Gamm-Schmidt procedure on the vectors $\vec{\nabla} n$ and $\vec{\nabla}\eta$. Define the new vectors:

$$\hat{\mathbf{v}}_\mathbf{n} = \frac{\vec{\nabla} n}{\sqrt{\vec{\nabla} n \cdot \vec{\nabla} n}} \tag{3.24}$$

$$\hat{\mathbf{v}}_\eta = \frac{\vec{\nabla}\eta - (\vec{\nabla}\eta \cdot \hat{\mathbf{v}}_\mathbf{n})\hat{\mathbf{v}}_\mathbf{n}}{\sqrt{(\vec{\nabla}\eta - (\vec{\nabla}\eta \cdot \hat{\mathbf{v}}_\mathbf{n})\hat{\mathbf{v}}_\mathbf{n}) \cdot (\vec{\nabla}\eta - (\vec{\nabla}\eta \cdot \hat{\mathbf{v}}_\mathbf{n})\hat{\mathbf{v}}_\mathbf{n})}}. \tag{3.25}$$

Second, subtract from the gradient of $\mathcal{N}$ its projections along vectors $\hat{\mathbf{v}}_\mathbf{n}$ and $\hat{\mathbf{v}}_\eta$:

$$\delta\mathbf{a} = \left(\vec{\nabla}\mathcal{N} - (\vec{\nabla}\mathcal{N} \cdot \hat{\mathbf{v}}_\mathbf{n})\hat{\mathbf{v}}_\mathbf{n} - (\vec{\nabla}\mathcal{N} \cdot \hat{\mathbf{v}}_\eta)\hat{\mathbf{v}}_\eta\right)\delta l = \mathbf{v}\delta l. \tag{3.26}$$

Note that $\vec{\nabla}\mathcal{N}$ is orthogonal to both $\hat{\mathbf{v}}_\mathbf{n}$ and $\hat{\mathbf{v}}_\eta$. Aside from the calculation of gradients, and inventing an efficient way to code this algorithm, this is the crux of the calculation. From our initial calculations with this method, we found that although the normalization constraint is well maintained, the loss constrained is not. Indeed, the steepest descent method, as defined by Eq. 3.26, will not strictly keep the constraint because $\delta\mathbf{a}$ lies in the plane tangent to the constraint manifold,

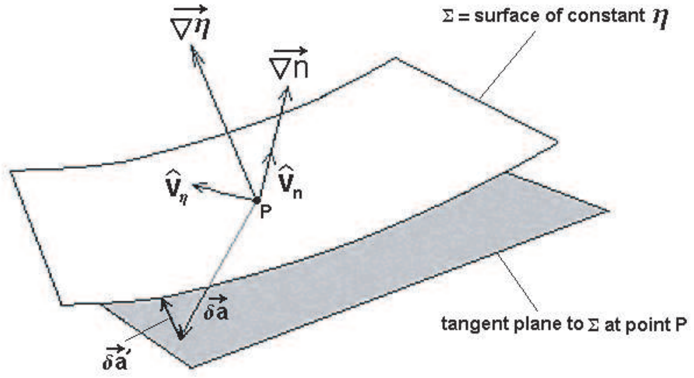

Figure 3.2: Surface of $\eta = const$ and its tangent plane.

and this manifold is non-linear, so there will be an error of order δl^2. Thus, we modified individual steps: $\mathbf{a}_{j+1} = \mathbf{a}_j + \delta\mathbf{a} + \delta\mathbf{a}'$, where $\delta\mathbf{a}' = \alpha\vec{\nabla}\eta\left(\mathbf{a}_j\right)$ (see Fig. 3.2). After making a step, $\delta\mathbf{a}$, along the plane tangent to the surface of constant η and n, we return to this surface along the gradient to η calculated[2] at the point $\mathbf{a}_j$. What is the error in the constraint that is being made without $\delta\mathbf{a}'$? We have

$$\Delta\eta = \eta(\mathbf{a}_{j+1}) - \eta(\mathbf{a}_j) = \frac{\partial\eta}{\partial a_i} v_i \delta l + \frac{1}{2}\frac{\partial^2\eta}{\partial a_i \partial a_j} v_i v_j \delta l^2.$$

But the quantity $\frac{\partial\eta}{\partial a_i} v_i$ is zero, which can be verified directly from Eq. 3.26 and the definition of $\hat{\mathbf{v}}_\eta$ in Eq. 3.25 and in Fig. 3.2. So the error in η is $\frac{1}{2}\frac{\partial^2\eta}{\partial a_i \partial a_j} v_i v_j \delta l^2$. Let's come up with a correction $\delta\mathbf{a}' = \alpha\vec{\nabla}\eta$. The goal is to calculate this α, i.e., how far along $\vec{\nabla}\eta$ do we need to travel to return precisely to the surface of constant η we left when making the step $\delta\mathbf{a}$. To obtain the needed α, let's assume that we made this correction at a step $\delta\mathbf{a}'$, calculated a new $\Delta\eta$, and set it to zero. We have

$$0 = \Delta\eta \quad = \quad \frac{\partial\eta}{\partial a_i}\left(v_i\delta l + \frac{\partial\eta}{\partial a_i}\alpha\right) + \frac{1}{2}\frac{\partial^2\eta}{\partial a_i\partial a_j}\left(v_i\delta l + \frac{\partial\eta}{\partial a_i}\alpha\right)\left(v_j\delta l + \frac{\partial\eta}{\partial a_j}\alpha\right).$$

This expression can be written more compactly in a coordinate-free notation:

$$0 = \frac{1}{2}\mathbf{T}\left(\tilde{\nabla}\eta, \tilde{\nabla}\eta\right)\alpha^2 + \left[\left\|\vec{\nabla}\eta\right\|^2 + \mathbf{T}\left(\mathbf{v}, \tilde{\nabla}\eta\right)\delta l\right]\alpha + \frac{1}{2}\mathbf{T}\left(\mathbf{v},\mathbf{v}\right)\delta l^2, \tag{3.27}$$

where $\mathbf{T}$ is a second-rank tensor with components $\frac{\partial^2\eta}{\partial a_i \partial a_j}$ in the $\hat{\mathbf{a}}$-basis. In the limit of very small δl, α is also very small, so to the very lowest order, we can neglect α^2 and δl in the above expression to see that $\alpha \approx -\frac{\text{error}}{\|\vec{\nabla}\eta\|^2}$. For the exact root to correspond to this approximate solution, we must

---

[2] We can return to it along many other vectors which do not lie in the $(\hat{\mathbf{v}}_\mathbf{n}, \hat{\mathbf{v}}_\eta)$ plane.

choose the $-$ root:

$$\alpha = \frac{-\left[\left\|\vec{\nabla}\eta\right\|^{2} + \mathbf{T}\left(\mathbf{v}, \tilde{\nabla}\eta\right)\delta l\right] - \sqrt{\left[\left\|\vec{\nabla}\eta\right\|^{2} + \mathbf{T}\left(\mathbf{v}, \tilde{\nabla}\eta\right)\delta l\right]^{2} - \mathbf{T}\left(\mathbf{v}, \mathbf{v}\right)\mathbf{T}\left(\tilde{\nabla}\eta, \tilde{\nabla}\eta\right)\delta l^{2}}}{\mathbf{T}\left(\tilde{\nabla}\eta, \tilde{\nabla}\eta\right)} \tag{3.28}$$

3.2.5 Minimization Strategy

Carrying this algorithm out numerically proves to be not trivial for several reasons. The first reason is that the minimization proceeds in a high-dimensional space; as many dimensions as n, the number of coefficients employed. An idea of how to avoid getting an undesired local minima was to first minimize in a space of relatively few dimensions, say start with a space of 7 a - coefficients picked such that η has the desired value of 10^{-6}. Normally this guess consisted of Mesa coefficients adjusted to fit the desired value of η. After the minimum in this low-dimensional space is found, we subsequently open up more dimensions *one by one*, and further minimize each time a new dimension is opened up (see Fig. 3.3). Note that we do not claim to prove rigorously that this strategy will result in the global minimum asymptotically as n grows; however, following this strategy proved useful in avoiding getting trapped in such solutions that are obviously incorrect. The second non-triviality is the choice of a step size. The program includes a sub-routine such that if the value of α is calculated to be complex, the program will return to one step back, decrease the step size by a factor of 10, and try again. However, there remains a question as to how to choose an *initial* step size. If a step size is too large, then even though a step is made in the direction of gradient, due to non-linearities, when the step is completed the new point may be situated at location of a *higher* value of noise. This can be corrected at the next step, but the approach to minimum would be non-uniformly decreasing. Therefore, we choose an initial step size such that at no time during the descent, a temporary increase in the value of the noise observed.

3.3 Results

The minimization code discussed in the previous section converges to a beam much wider than Mesa. The intensity profile is shown in Fig. 3.6, and the amplitude distribution in Fig. 3.4. In the clipping approximation, these beams have the same diffraction loss as Mesa: 1ppm.

Although only the coating noise was minimized in the code, the substrate noise decreased as well by a comparable factor. Overall noise is reduced by roughly a factor of two in the region of maximum sensitivity, increasing LIGO's event rate by a factor of three in this region.

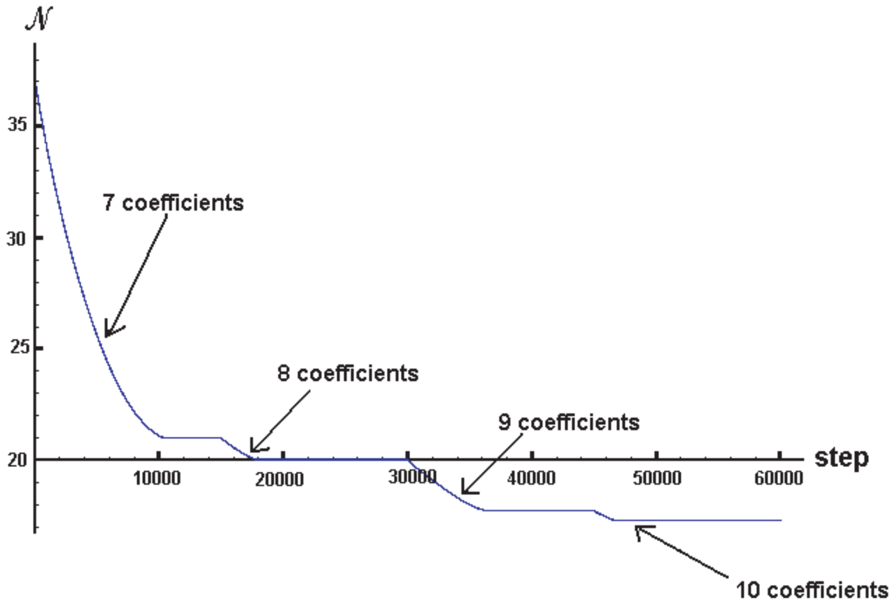

Figure 3.3: A sample minimization process. Every time a new dimension is added, the minimization falls downhill.

3.3.1 Internal Thermal Noise

As shown in Fig. 3.7 and Fig. 3.5, the power and electric field amplitude distribution for the beam we derived extends over a much larger fraction of the mirror than the previously considered Mesa beam. This desirable feature leads to an overall decrease in thermal noise by a factor of two compared to Mesa, and hence provides a strong reason to further research conical beams in the context of LIGO.

In Table 3.1, we show how much lower the conical cavity noise is compared to the Mesa cavity noise. This decrease in noise by roughly a factor of two could drive an increase in event rate by up to a factor of three in the region where the instrument has the highest sensitivity.

Table 3.1: Ratio of Mesa cavity noise to conical cavity noise for different types of noises. The conical cavity noise is lower by more than a factor of 2.

Noise	Brownian	Thermoelastic
Coating	2.339	2.339
Substrate	1.534	3.302

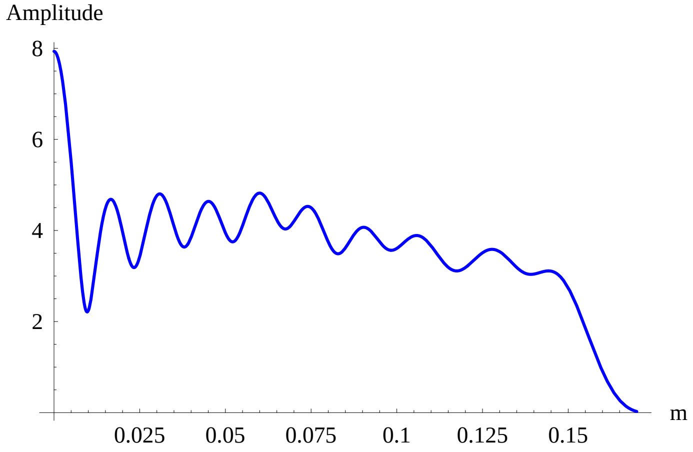

Figure 3.4: The amplitude distribution of the lowest-noise beam found using our minimization algorithm. This plot includes 35 Gauss-Laguerre coefficients.

3.3.2 Field Characterization at the Mirror

The power distribution at the mirror shown in Fig. 3.6 is characterized by a central peak and oscillations at centimeter scale. The power decreases very quickly, much faster than a minimum Gaussian, close to the mirror edge. The integrated power outside the mirror is 1 ppm of the total power, but, unlike Gaussians and Mesa, the power does not decrease in a uniform manner, and there are a few noticeable power maxima outside the mirror radius. Figure 3.14 shows the conical beam power distribution outside the mirror, and Figure 3.15 compares it with Mesa. The amplitude of the electric field as shown in Fig. 3.5 at the central peak is only 30% stronger than the amplitude of the electric field on the Mesa beam's constant power area and less than the baseline design Gaussian at the mirror center. The power in this central peak is small compared to the total beam power which remains smaller than Mesa everywhere else in Mesa's flat central area. Conical beams have a lot of power at large radii spread over a larger fraction of the mirror than the Mesa's small radius plateau.

We thus do not believe that our beam is particularly hard for the coating to tolerate.

3.3.3 Mirror

The mirror we obtained shown in Fig. 3.8 is nearly conical with minor perturbations that cause the resulting beam to fall off faster at larger radii than does the standard Bessel-Gauss beam [21]. As in previous work [1], we determined the mirror surface to be the phasefront of the theoretical beam obtained through the minimization process.

Although a cone may seem hard to make in practice, we believe this is possible because the curvature scale is not fundamentally different from the non-spherical Mesa mirrors considered previously for LIGO, that present technology can produce. We do not understand the details of the

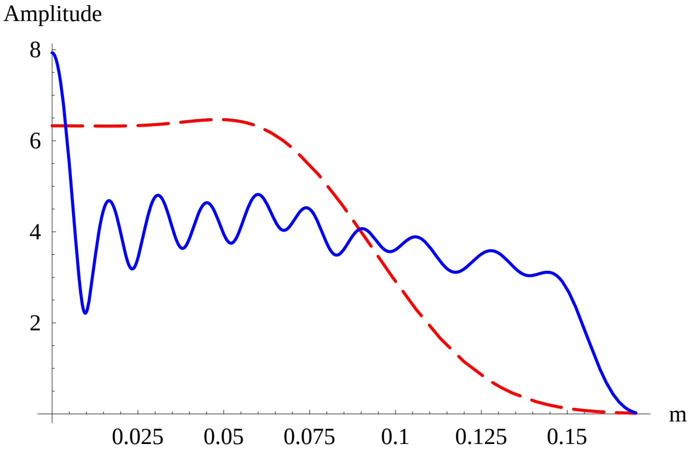

Figure 3.5: The amplitude distribution of the lowest-noise 35 coefficient beam found using our minimization algorithm compared with the previously published Mesa Beam.

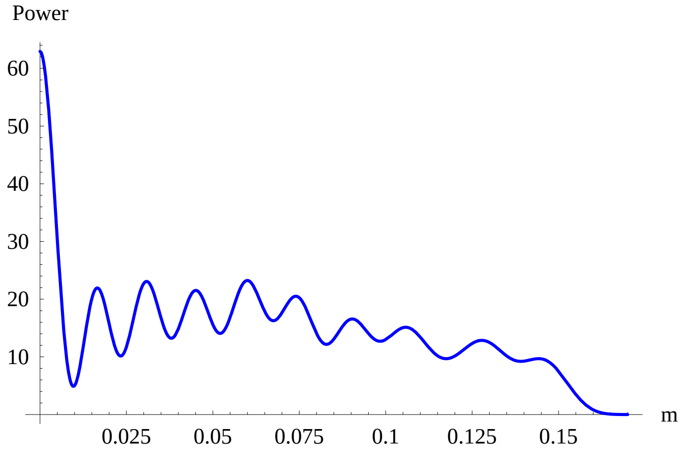

Figure 3.6: The power distribution of the lowest-noise 35 coefficient beam found using our minimization algorithm.

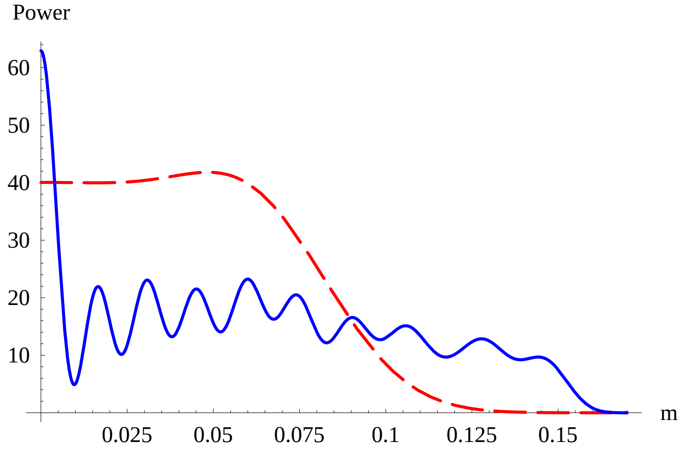

Figure 3.7: The power distribution of the lowest-noise 35 coefficient beam found using our minimization algorithm, compared with the previously published Mesa Beam.

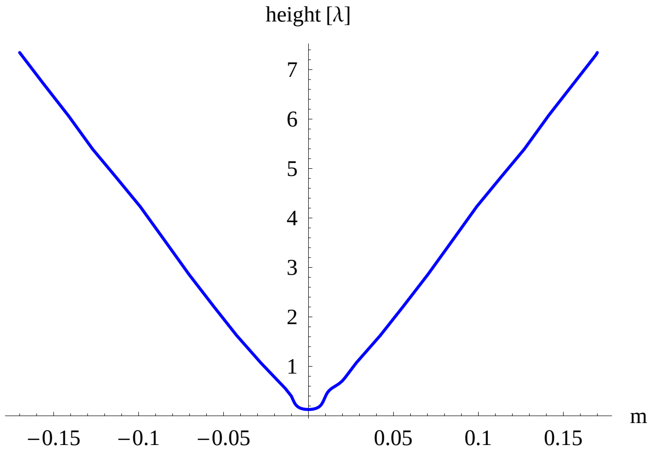

Figure 3.8: The height of the nearly conical mirror plotted in units of $\lambda = 1.06\mu\text{m}$

manufacturing process and differences may exists, but, a priori, the conical mirrors and Mesa appear to be equally hard to manufacture.

In Fig. 3.9, we plot the cross section of the conical mirror along with the nearly-concentric and the nearly-flat Mesa mirrors.

3.3.4 Convergence and Conical Cavities with Fewer Coefficients

The results presented throughout most of this chapter are based on our 35 coefficients best-case minimization result. Low-noise cavities may however be found that employ many fewer Gauss-Laguerre coefficients. They are not as good as our final result, but still much better than Mesa. Employing fewer Gauss-Laguerre modes may lead to a cavity that is more desirable for reasons other

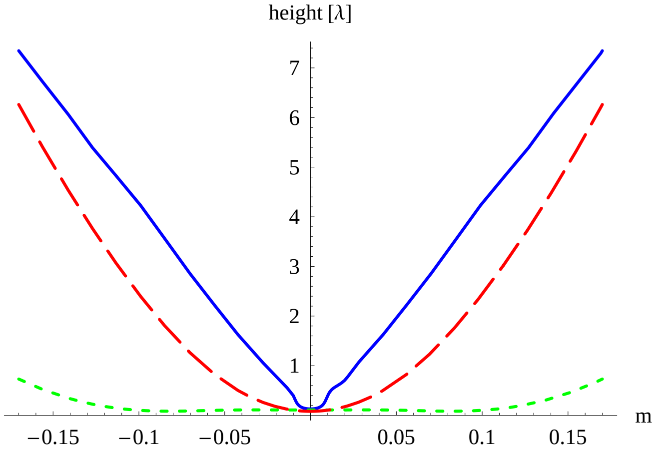

Figure 3.9: Nearly conical (solid blue line) mirror compared with the its nearly concentric (dashed red line) and nearly flat (dotted green line) Mesa counterparts.

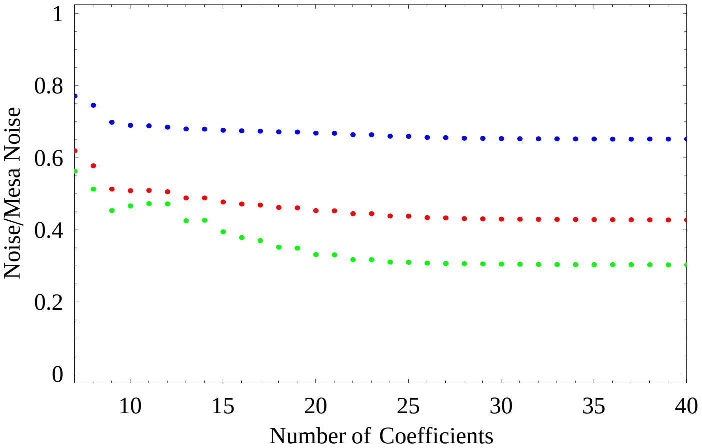

Figure 3.10: Thermal noise as a function of the number of Gauss-Laguerre coefficients employed in the minimization code. Substrate Brownian noise is in blue, the coating noise is in red, and the substrate thermoelastic noise is in green. Although we minimized for the coating noise alone, the substrate thermoelastic noise decreases more than the coating noise, while the substrate Brownian noise decreases less. Both coating Brownian noise and coating thermoelastic noise obey the same scaling law. The coating thermal noise is expected to be the largest in the fused silica mirrors considered for LIGO design, while thermoleastic noise would be the leading contribution if Sapphire mirrors were to be used. This figure is normalized so that the Mesa noise is 1 for each of the three noises.

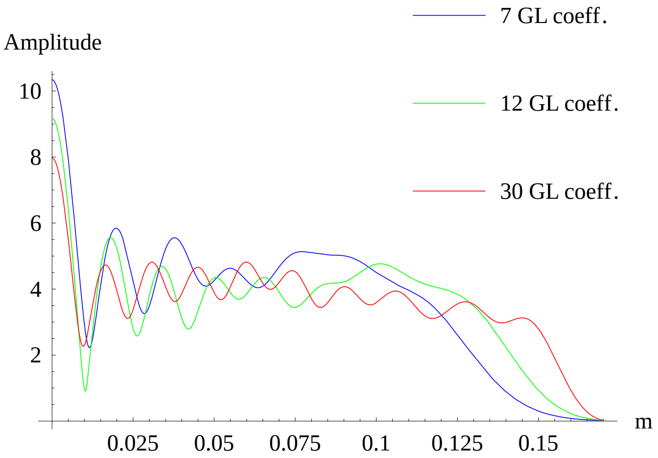

Figure 3.11: Amplitude of the electric field at the mirror as a function of the number of Gauss-Laguerre coefficients employed in the minimization code. When fewer coefficients are used, the beam is spread over a smaller area of the mirror.

than thermal noise. Another reason for showing this figure is to demonstrate convergence.

In Figure 3.10, we show how different noises decrease compared to Mesa as the number of Gaus-Laguerre coefficients is increased.

When using fewer Gauss-Laguerre modes in the beam expansion, the beam does not extend all the way out to the end of the mirror. In Fig. 3.11, we show the electric field amplitude at the mirror for beams obtained by minimizing the coating noise over the lowest 7-, 12- and 30- Gauss-Laguerre modes. In Fig. 3.12, we show the power distribution at the mirror for the same beams.

As seen in Fig 3.13, there is little qualitative difference in the mirror shapes, depending on the number of coefficients used. Qualitatively, in all these cases we are dealing with nearly-conical mirrors and nearly-diffraction-free beams [24]. [3]

3.3.5 Optical Modes Supported by Finite Nearly-Conical Mirrors and their Diffraction Loss

Maintaining diffraction losses under 20 ppm is important for LIGO. We designed our mirrors to have losses of 1 ppm in the minimization process as these are the same guidelines used for designing Mesa Beams with 20-ppm losses.

---

[3] Diffraction free means the mode maintains its shape when it travels. This is not true for our beam, nor for any finite beam in the real world. Bessel-Gauss beams have been called nearly diffraction free because they diffract very little. Little diffraction means small diffraction losses and thus what we want.

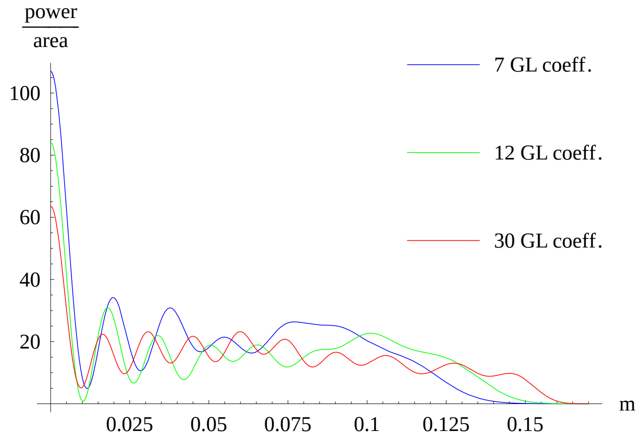

Figure 3.12: Power distribution at the mirror as a function of the number of Gauss-Laguerre coefficients employed in the minimization code. When fewer coefficients are used, the beam is spread over a smaller area of the mirror.

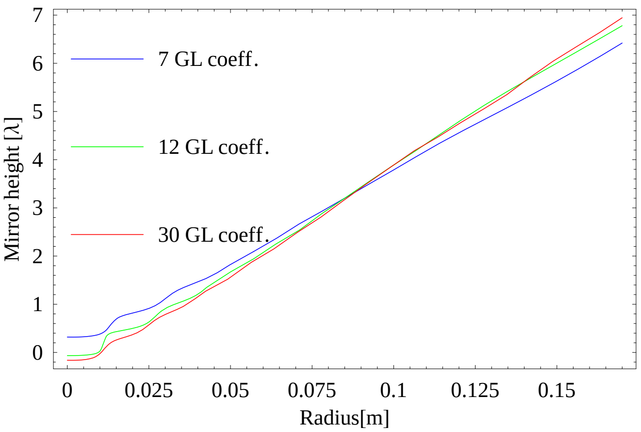

Figure 3.13: Mirrors supporting the 7, 12, and 30 coefficients modes. The mirror height is measured in units of λ, where $\lambda = 1.06\mu$m is the wavelength of the light used in the interferometer.

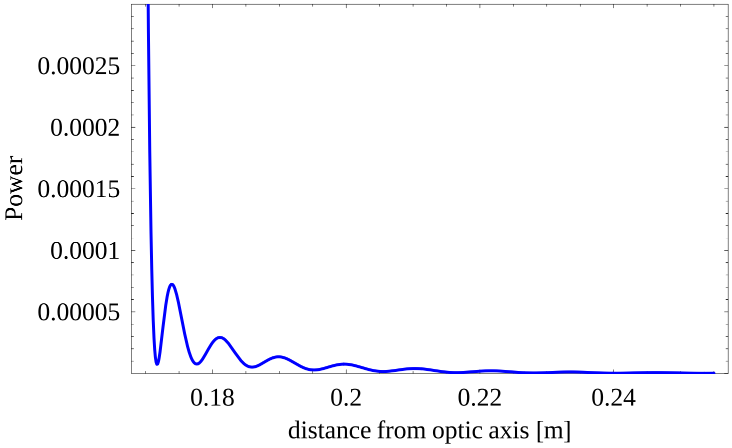

Figure 3.14: The power distribution of the 35 coefficient lowest-noise beam outside the mirror. In the clipping approximation, the integral of this power is the assumed to be the diffraction loss.

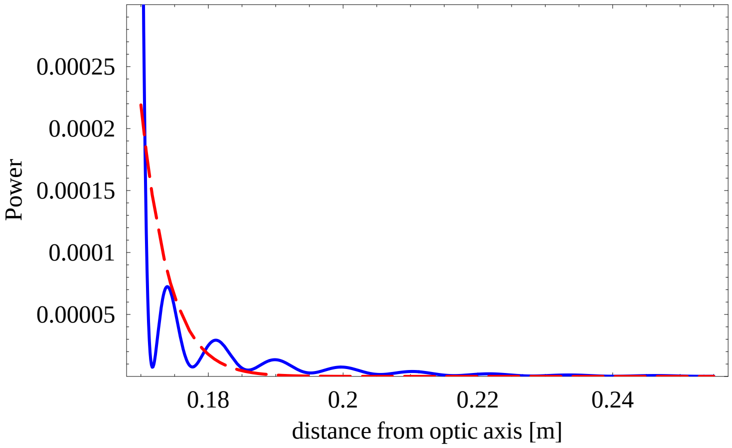

Figure 3.15: The power distribution of the 35 coefficient lowest-noise beam outside the mirror compared to the theoretical prediction for Mesa. In the clipping approximation, the integral of this power is the assumed to be the diffraction loss.

The clipping approximation discussed previously in this chapter estimates the diffraction loss as

$$D = \frac{\int_{Rmirror}^{\infty} 2\pi U^2 r dr}{\int_0^{\infty} 2\pi U^2 r dr}. \tag{3.29}$$

This is a simple formula and has been used in many published papers [8, 4, 1], but its results are not always very exact. Its main advantage is that it requires little computational resources, and thus is suitable for a minimization code where it needs to be run many times.

We verified the diffraction losses of the final result by propagating a beam in a cavity with mirror surfaces described by the innermost 17 cm of the phasefronts of the theoretical beam. In this cavity we obtained a beam that closely resembles the theoretical prediction with diffraction losses about three times higher (3.03 ppm). [4]

In each optical cavity, there are an infinity of resonating modes. When the cavity has finite mirrors, these modes will not be loss-free and their corresponding eigenvalues will be less than 1.

Following [17], we computed the eigenvalues of the axisymmetric propagator and obtained only one that was close to 1. All other higher eigenmodes had high diffraction losses. These eigenvalues are listed in Table 3.2.

According to [17], in axisymmetric cavities, the propagator, K, from one mirror to the other can be written as

$$K_n = \frac{i^{n+1} k}{L} J_n(\frac{k r_1 r_2}{L}) e^{ik[h_1(r_1)+h_2(r_2)-L-\frac{r_1^2+r_2^2}{2L}]} \ , \tag{3.30}$$

where $J_m(z)$ is the m^{th} order Bessed function of the first kind given by

$$J_n(z) = \frac{1}{2\pi i^n} \int_0^{2\pi} e^{iz\cos\phi} e^{in\phi} d\phi \ . \tag{3.31}$$

L is the length of the arm cavity, k is the wave number $k = \frac{2\pi}{\lambda}$, and $h_1(r)$,$h_2(r)$ are the mirror heights and are assumed to be equal; i.e., the cavity is assumed to be symmetric and unperturbed. The mirror radii are r_1 and r_2, and n labels the state, with $n = 0$ being the desired cavity state.

The eigenvalues and eigenvectors of this propagator were found numerically using Mathematica.

3.4 Tolerance to Imperfections and Compatibility with LIGO

3.4.1 Sensitivity to Mirror Tilt

To simulate the effects of mirror perturbations on the conical cavity, we simulated the propagation of the light from one mirror of the cavity to the other, in Mathematica, without taking advantage

---

[4] This shows the limitations of the clipping approximation.

Table 3.2: Diffraction losses in parts per million for the first few modes of the conical cavity. The diffraction loss is computed as $1-|\lambda_i|$, where $|\lambda_i|$ is the absolute value of the one-way axisymmetric propagator.

	l=0	l=1	l=2
p=0	1.45	62086	11380
p=1	22441	69032	48377
p=2	62587	244030	120902
p=3	146275	406127	220276
p=4	289039	553632	359044

Table 3.3: Separation of eigenmodes in phase space. The table shows the difference between the argument of the desired mode and all the others. Having the desirable mode well separated from higher modes makes locking easier.

	l=0	l=1	l=2
p=0	0	-3.06	0.19
p=1	2.93	-0.12	-3.11
p=2	-1.08	2.01	-0.79
p=3	1.50	-1.46	1.82
p=4	-2.51	0.23	-2.25

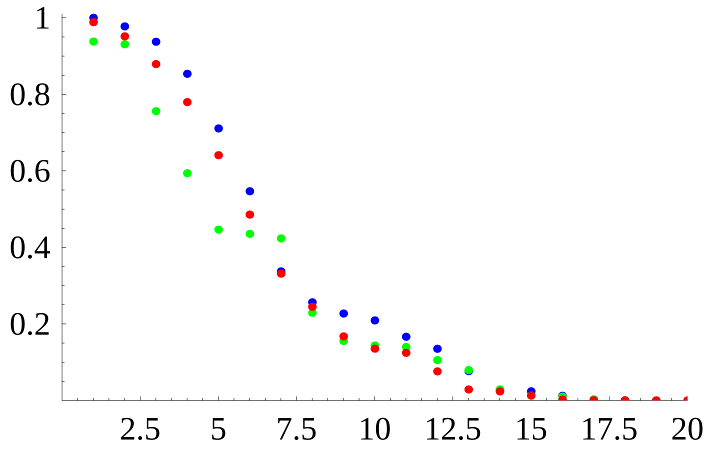

Figure 3.16: Absolute Value of eigenvalues of the one-way propagator. The blue dots represent $p = 0$ axisymmetric modes, the green $p = 1$, and the red $p = 2$.

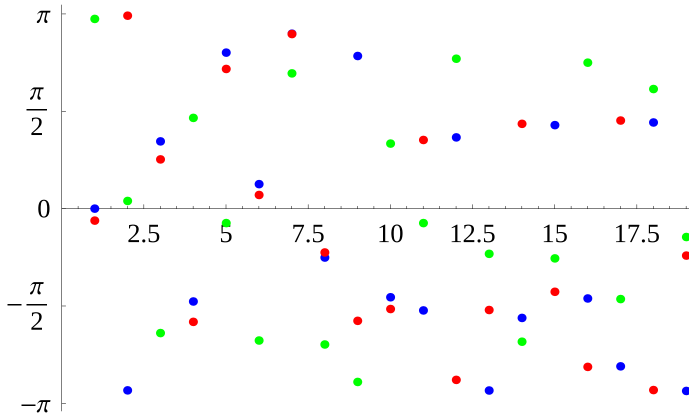

Figure 3.17: Phase of eigenvalues of the one-way propagator. The blue dots represent $p = 0$ axisymmetric modes, the green $p = 1$, and the red $p = 2$. The desirable mode has phase zero in this picture. The modes are well separated and, compared to Mesa, the modes close to the desirable one have high losses.

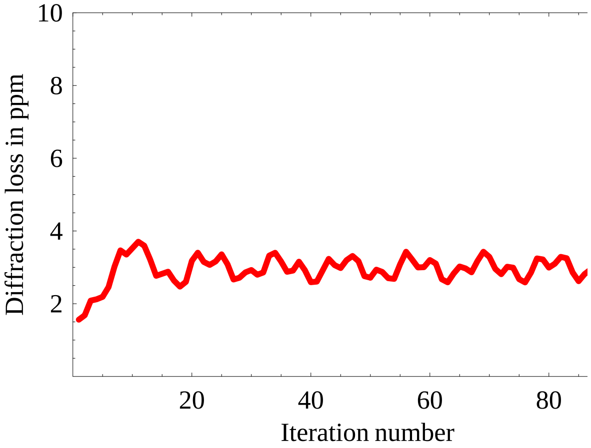

Figure 3.18: Diffraction loss in a nearly-flat Mesa cavity when perturbed symmetrically by a 10^{-8} radians tilt

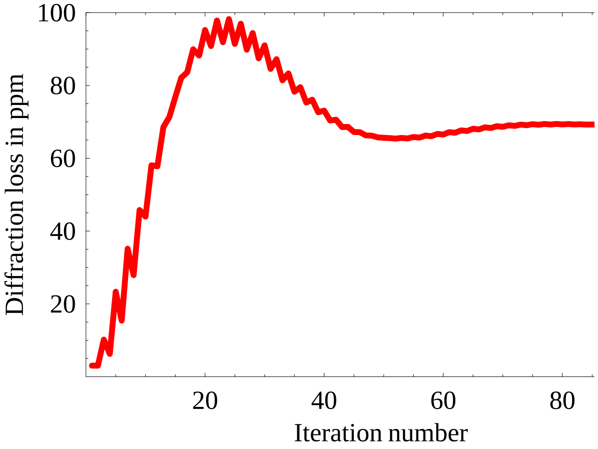

Figure 3.19: Diffraction loss in a conical cavity when perturbed symmetrically by a tilt of 10^{-8} radians

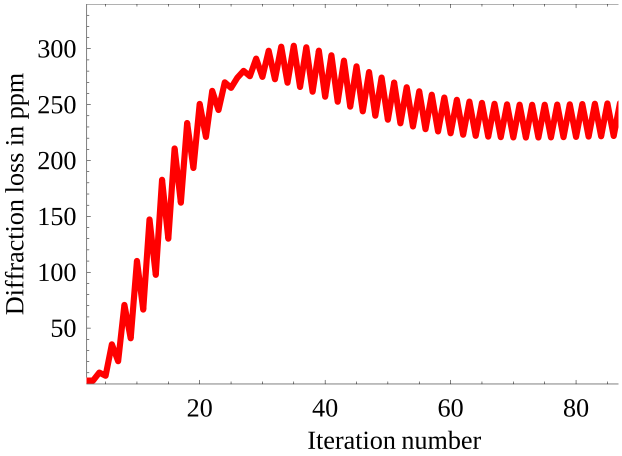

Figure 3.20: Diffraction loss in a conical cavity when only one mirror is perturbed by a 10^{-8} radians tilt

of any symmetries. We used this tool to study the effects of mirror tilt, mirror displacement, and mirror figure errors as well as checking the diffraction losses of the conical cavity.

Our numerical simulation (Fig. 3.18) shows Mesa cavities to increase the diffraction loss to about 3 ppm when perturbed symmetrically by a 10^{-8} radians mirror tilt. The same tilt induces a diffraction loss of about 70 ppm in our conical cavity (Fig. 3.19). When the perturbation is asymmetric [5], as is often the case in the real world, the same tilt induces a diffraction loss of nearly 250 ppm as seen in Fig. 3.20. This is because the effect of the tilt is combined with a mirror translation. The diffraction loss depends quadratically on the tilt angle as shown in figure 3.21. The interpolating function, when x is the tilt in radians, is given by

$$DL = 3.03ppm + x^2 * 0.646\frac{ppm}{nrad} \tag{3.32}$$

In conclusion, the conical mirrors proposed here respond to tilt perturbation more strongly than Mesa does. The suspension and mirror control system would need to be engineered to control the mirror direction better.

If LIGO is to use conical mirrors, the tilt needs to be controlled at the level of about 3 nano radians.

3.4.2 Mirror Figure Error

The mirror figure errors are imperfections in the mirror surface. In this section, we discuss the way mirror figure errors affect the Mesa and our conical beam. The figure errors have been measured experimentally for the LIGO I mirrors currently used in the experiment. We used the real measured

---

[5] Any asymmetric tilt can be decomposed in a symmetric and an antisymmetric component. The antisymmetric component can be thought as a displacement because the mirrors remain parallel.

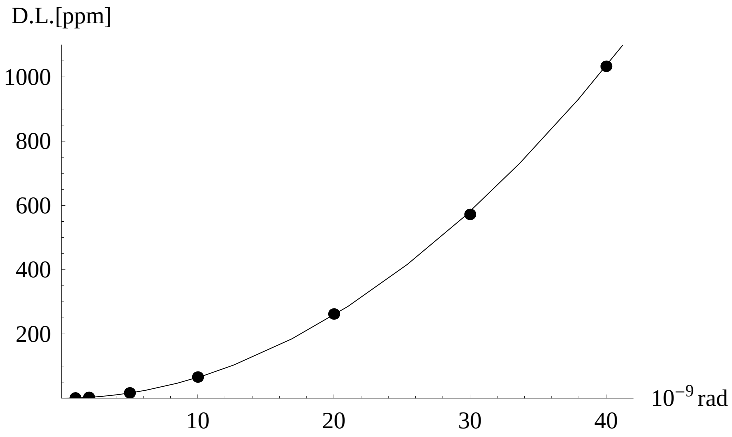

Figure 3.21: Diffraction loss in a conical cavity when its mirrors are symmetrically tilted as a function of the tilt

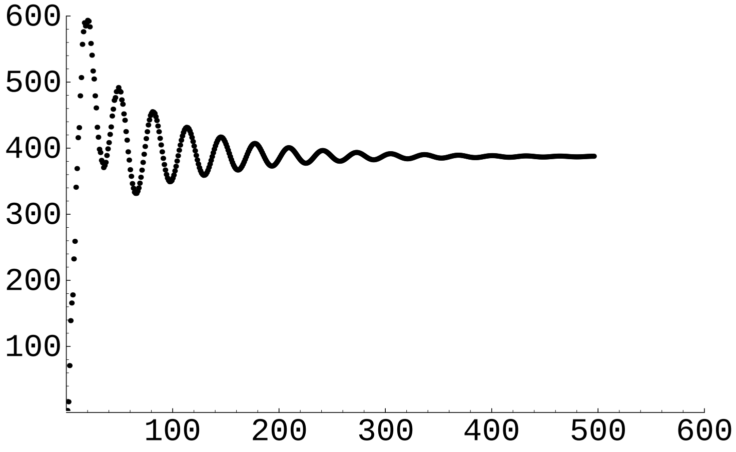

Figure 3.22: Diffraction loss in ppm a conical cavity when perturbed symmetrically by the LIGO I figure error. We started with the field resonating in the unperturbed cavity with 3 ppm diffraction loss and simulated its propagation. The reflection number is shown on the horizontal axis.

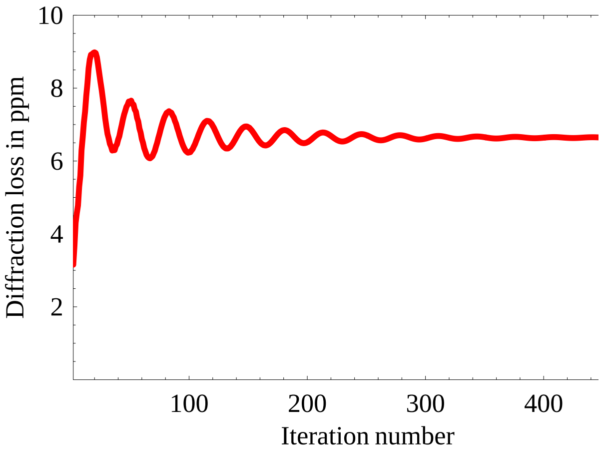

Figure 3.23: Diffraction loss in conical cavity when perturbed symmetrically by one tenth of the LIGO I figure error

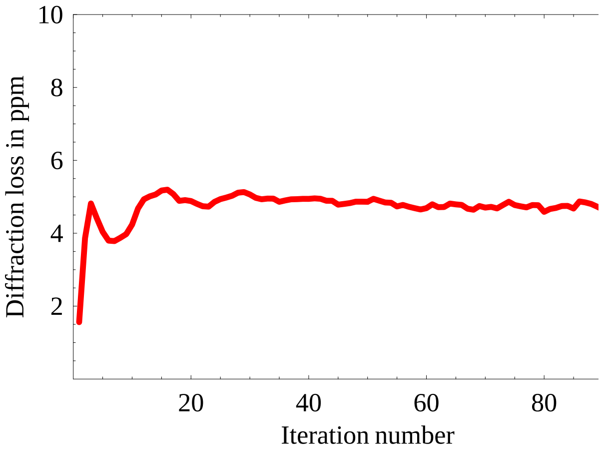

Figure 3.24: Diffraction loss in a nearly-flat Mesa cavity when perturbed symmetrically by the LIGO I figure error

data from [18]. Since LIGO I and Advanced LIGO have different mirror sizes, we interpolated the data and stretched it in order to fit the desired mirror size. This is not very good, because the length scale of the perturbations will make a difference in the losses, but it this method was also used in [10] and it brings us close to real measured figure error.

As we will show later, mirror perturbations with longer wavelength affect Mesa less than they affect the conical cavity and "stretching" the perturbations of a smaller mirror to a larger size decreases the wavelength of the figure error. The net impact is an increase in the Mesa/Cone difference. It is reasonable to expect the mirrors used in Advanced LIGO will be manufactured with higher precision, as new technologies have become available since initial LIGO was built. Also, these new technologies are likely to produce perturbations with a different frequency spectrum.

To cut computational time, we started with a cavity with perturbed mirrors and picked the initial value for the field to be that that resonated in the unperturbed cavity. We then propagated the field back and forth several times until the diffraction loss stopped changing.

Mesa mirrors are more tolerant to figure error. Adding about a tenth of the perturbation to the conical mirrors produces roughly the same increase in diffraction loss as the full perturbation in a Mesa cavity.

If Advanced LIGO is to use conical mirrors manufactured with the same figure error distribution as in Initial LIGO, the magnitude of the figure error needs to be reduced by roughly a factor of 10. As shown in the next section, however, conical mirrors are more sensitive to large scale figure error.

3.4.3 Understanding the Impact of Various Frequency Components of the Mirror Figure Error on the Diffraction Losses

In Section 3.4.2, we used the errors measured on the LIGO I mirrors as a benchmark for our new cavity. There are a few disadvantages in doing this. The LIGO I mirror figure error maps were affected by large errors in the measurement; these errors may well be higher than the measured difference between the desired and the achieved mirror shape.[6] Moreover, the advanced LIGO mirrors are likely to be manufactured using different technology. Initially, the method of choice was to build a spherical mirror first and then apply coating of variable thickness to attain the Mesa shape. Recently, the LIGO community is considering working with QED Technologies, a company that specializes in extremely precise polishing. Their method yields a much different spectral decomposition of the figure errors than the methods implied in LIGO I [7]. If QED Technologies will indeed polish Advanced LIGO's mirrors, the ratio of small-scale to large-scale deviations from the desired shape will be much higher than in LIGO I. That means the large-scale deviations will be less than in the published figure errors, while the small scale perturbations will be higher. It is probably still too

---

[6] I thank Garilynn Billingsley for pointing this out and for her kind comments regarding this entire section.

[7] Tests are currently under way to test the accuracy and limitations of their method.

early to say that QED will actually make the mirrors for Advanced LIGO. They are mentioned here here only as an interesting possibility and as a very experimental motivation for studying the effects of figure errors with different frequencies on Mesa as well as on the conical mirrors herein proposed.

In this section, we report our analysis of the effects of various scale perturbations on the conical and Mesa cavities. Generally speaking, small length scale perturbations of the mirrors result in large angle scattering. The light scattered at large angles leaves the cavity without meeting the other mirror, and thus is lost. Therefore, high angle scattering is expected to affect Mesa and the conical cavity in the same way. Large-scale perturbations, on the other hand, are likely to affect Mesa less than the conical cavity because they scatter light at small angles. The light scattered at low angles from one mirror reaches the other mirror.

In the case of Mesa, because higher modes are long lived, light is likely to stay in the cavity longer and more of it will have the chance to leak back in the ground state. In the conical cavity, light scattered at small angles will leave the cavity much faster and thus be lost because there are no higher modes with low diffraction loss.

Another notable difference is that in a perturbed Mesa cavity, although the diffraction loss is small, the resonating light has significant higher mode components. In our conical cavity, the resonating mode will always be very near to the ground state with higher modes being lost very quickly. This may give the instrument operators better control over the light intensity on the mirror surface.

As seen in Tables 3.5 and 3.4, only the large wavelength components of the initial LIGO measured mirror figure error generate very large diffraction losses in the conical cavity; whereas they either generate very small losses or even decrease the diffraction loss in Mesa. It is exactly these perturbations that the polishing methods developed by QED Technologies should be able to tackle more successfully than the coating method previously considered.

3.4.4 Sensitivity to Mirror Translation

As expected from the previous sections, the conical cavity is more sensitive to correct mirror positioning than is the Mesa cavity. Mirror translations can be thought of as perturbations with large wavelengths and thus would affect the conical mirror more than they affect Mesa. Moreover, in the conical cavity, there is more light near the mirror boundary, the region most affected by an error in positioning the mirrors.

Simulations show that a conical cavity with a mirror translated by 10 μm from its ideal position will have a diffraction loss of 57.61 ppm. A similar diffraction loss is seen in a Mesa cavity with a 4 mm error in the mirror positioning. Thus the conical cavity is far more sensitive to tilt than Mesa. In Table 3.6 we show a few more numerical values for diffraction losses of the conical cavity when one mirror is shifted away from the optic axis.

Table 3.4: Mesa and conical cavity noise when perturbed by randomly generated frequency-filtered figure error.

Random Perturbations with $\lambda \geq$	Cone	Mesa
4R	23.71	3.16
2R	136.95	3.12
R	65.12	3.33
R/2	78.48	3.17
R/4	31.44	5.63
R/8	38.93	35.79
0	38.32	36.41

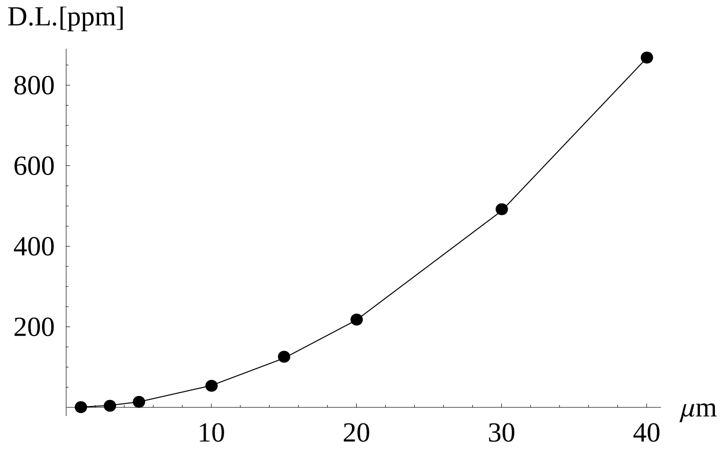

Figure 3.25: Dots represent the diffraction loss in ppm for a conical cavity perturbed by moving one mirror away from the optic axis as a function of this displacement. The continuous line is a quadratic function fit to the data.

Table 3.5: Mesa and conical cavity diffraction losses when the mirrors are perturbed by the some of the Fourier components of the LIGO I noise, rescaled to fit the Advanced LIGO mirror size.

Removed perturbations with $\lambda \geq$	Cone	Mesa
R/16	3.16	2.68
R/8	4.71	3.83
R/4	6.34	5.24
R/2	12.47	7.96
R Large scale structure clearly present	56.28	5.63
2R	184.13	5.03
4R	404.83	4.86

Table 3.6: Conical cavity diffraction losses when the mirrors are shifted away from the optic axis

Mirror Displacement away from optic axis in μm	Cone unperturbed diffraction loss	Additional loss based on 3.03 ppm
1	3.57	0.54
3	7.94	3.91
5	16.67	13.64
10	57.56	53.53
15	125.69	122.66
20	220.96	217.93
30	491.96	488.93
40	871.54	868.51
80	3393.33	3390.30

A quadratic function can be fit well to the data shown in Table 3.6, as seen in Fig. 3.25. The diffraction loss in parts per bounce per million of a conical cavity perturbed by moving one of the mirrors a distance x parallel to itself in a direction orthogonal to the optic axis is thus approximatively given by the formula

$$DL = 3.03ppm + x^2 * 0.542\frac{ppm}{\mu m^2} \tag{3.33}$$

The mirror position in the current LIGO design is not controlled as accurately as needed here in the direction perpendicular to the optic axis. The mirror position in the direction of the optic axis is fixed within a fraction of a wavelength because this is required for locking Gaussian or Mesa beams. Since neither Gaussian nor Mesa beams require similar control level in directions perpendicular to the optic axis, the position in these directions is allowed to oscillate. However, since it is possible to control the mirror position in one direction to the desired accuracy, we believe it is worth considering a redesign of the suspension system that would allow similar levels of control in all directions.

In conclusion, if Advanced LIGO is to use conical mirrors, mirror position needs to be controlled to about 4 μm. If one uses mirror tilt to compensate errors in mirror location, the tilt would need to be controlled to about 1 nano radian.

3.4.5 Driving the Conical Cavity with a Gaussian Beam

Mesa beams have been proposed mainly to drive down the thermal noise. An added advantage is that the Mesa cavity can be driven – and is designed to be driven – by a Gaussian beam.

Our conical cavities support beams with conical phase fronts that are nowhere near Gaussians. We thus do not expect these cavities to be driven with Gaussian beams under any circumstances. We did however run a few simulations in order to understand what would happen if a conical cavity were to be driven by a Gaussian beam.

We bounced a Gaussian inside a Mesa cavity 1500 times at a 512-grid-points resolution on a square grid that was four mirror radii on a side. We noticed a total diffraction loss of only 2.5% and just over 1% after 500 bounces as shown in Fig. 3.31. The power distribution was however not stable and not close to TEM00.

A conical cavity initially excited with the same Gaussian, reached a nearly indistinguishable form from the theoretical prediction within 500 bounces as shown in Fig. 3.26, but it had lost most of its power Fig. 3.30. The diffraction loss per bounce also reaches desirable values much faster than in the Mesa case (Fig. 3.29).

When excited with something different from its own resonant mode, the conical cavity will lose light relatively quickly, while Mesa can easily be driven with a Gaussian.

If a cavity has only one nearly lossless mode, our simulation will converge to it fairly quickly. In

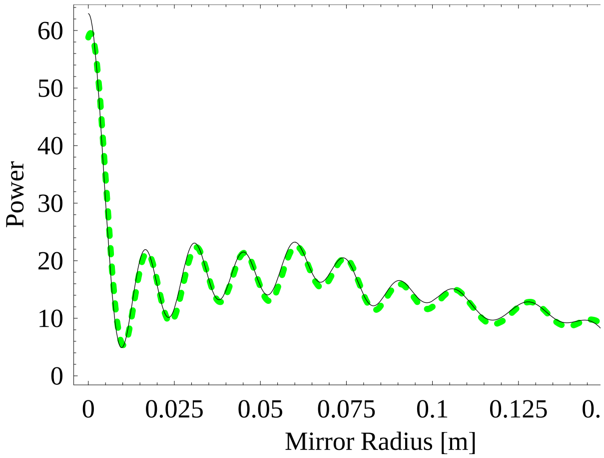

Figure 3.26: Conical cavity power profile (dotted green curve) after 250 round trip propagations (500 mirror reflections) compared with the theoretical prediction (continuous black curve). The diffraction loss reaches 3 ppm after 500 reflections, while the theoretical prediction is 1 ppm according to the clipping approximation. The cavity was initially excited with a Gaussian beam.

practice, however, to have this mode resonate and have the interferometer lock, one would still need to fine tune the cavity length. If a cavity has many nearly-lossless modes, we do not select any of them and thus they all survive. This leads to the light power distribution being different at each bounce, as we can see in the case of Mesa. This only indicates that the cavity can hold lights in several resonating modes, but still one must be picked by fine tuning the cavity length so that only the desired mode resonates. This is only possible if the modes are well separated in phase space.

3.5 Conclusions

We developed and implemented a simple minimization algorithm and used it for finding the LIGO-compatible beam with the lowest thermal noise. We find that although we only minimized for the coating noise, all other noise decreased roughly by comparable factors.

For these beams to be used in LIGO, the test mass suspension system must be redesigned to control tilt to about 1 nano radian and mirror figure errors need to be – at large scale – 10 times smaller than in Initial LIGO.

3.6 Acknowledgements

GariLynn Billingsley provided information about mirror manufacturing and Rana Adhikari made us confident that the suspension system of future LIGO detectors are likely to control mirror position well enough to make conical mirrors useable.

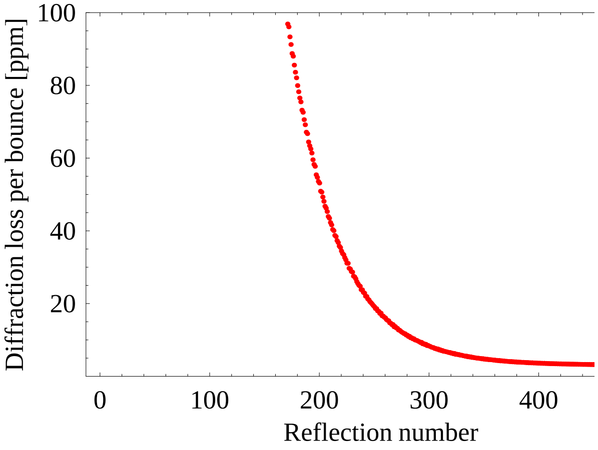

Figure 3.27: Diffraction loss in a conical cavity initially excited with a Gaussian beam

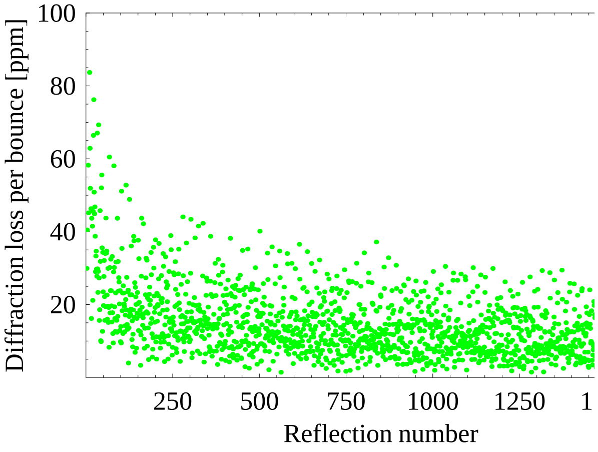

Figure 3.28: Diffraction loss in a Mesa cavity initially excited with a Gaussian beam

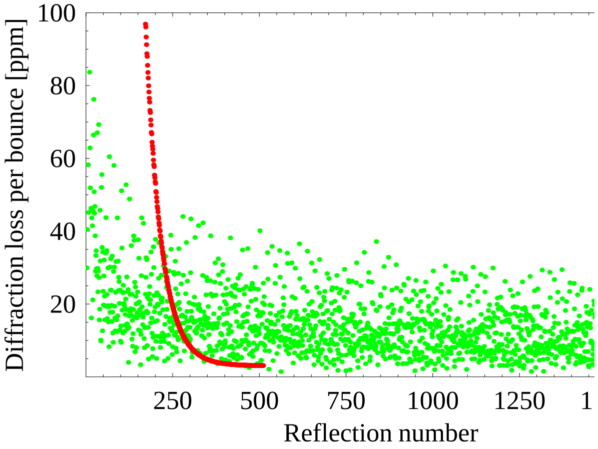

Figure 3.29: Comparison of Mesa- and conical-cavity diffraction losses. Mesa keeps a high diffraction loss and an unstable amplitude distribution for much longer than does the conical cavity, due to many eigenmodes having very small losses.

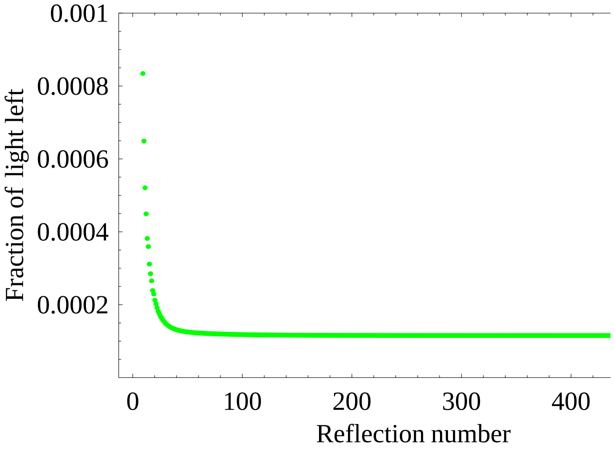

Figure 3.30: The amount of light left in a conical cavity initially excited with a Gaussian as a function of the number of reflections off the end mirrors. Note the very large early loss, followed by very small loss.

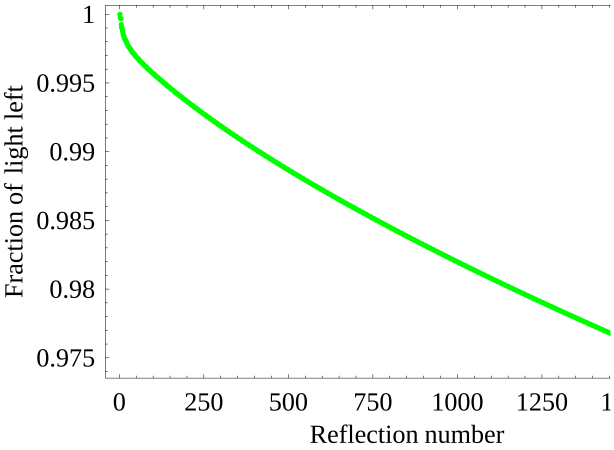

Figure 3.31: The amount of light left in a Mesa cavity initially excited with a Gaussian as a function of the number of reflections off the end mirrors. Note the very small early loss due to many excited eigenmodes that have low diffraction loss and take a very long time to die away.

Ruxandra Bondarescu, and Andrew Lundgren carefully proofread the manuscript, checked my calculations, and gave me valuable advice about the content and the format of this chapter.

The material in this chapter will be published, with some modifications, will soon be submitted for publication. I thank my coauthors, Yanbei Chen, and Oleg Kogan for collaborating with me on this project.

Bibliography

[1] M. Bondarescu and K. S. Thorne, "A new family of light beams and mirror shapes for future LIGO interferometers," Phys. Rev. D **74**, 082003 (2006) arXiv:gr-qc/0409083.

[2] Kip S Thorne, Mihai Bondarescu, Yanbei Chen "Gravitational Waves - A Web Based Course," Available online at http://elmer.tapir.caltech.edu/ph237 or on DVD from Caltech library. The Levin Thought Experiment is discussed in the week 12 homework.

[3] LIGO http://www.ligo.caltech.edu/

[4] G. Lovelace, "The dependence of test-mass coating and substrate thermal noise on beam shape in the advanced laser interferometer gravitational-wave observatory (advanced LIGO)," [arXiv:gr-qc/0610041].

[5] A. Gillespie, F. Raab "Thermally excited vibrations of the mirrors of laser interferometer gravitational-wave detectors," Phys. Rev. D, **52**, 577 (1995)

[6] Y. Levin, "Internal thermal noise in the LIGO test masses: A direct approach," Phys. Rev. D **57**, 659 (1997).

[7] Y. T. Liu and K. S. Thorne, "Thermoelastic Noise and Homogeneous Thermal Noise in Finite Sized Gravitational-Wave Test Masses," Phys. Rev. D **62** 122002 (2000), arXiv:gr-qc/0002055.

[8] G. M. Harry *et al.*, "Thermal noise in interferometric gravitational wave detectors due to dielectric optical coatings," Class. Quantum Grav. **19**, 897 (2002).

[9] E. D'Ambrosio *et al.*, "Reducing Thermoelastic Noise in Gravitational-Wave Interferometers by Flattening the Light Beams," arXiv:gr-qc/0409075.

[10] R. O'Schaughnessy, "Coating thermal noise for arbitrary shaped beams," Class.Quant.Grav. **23** (2006) 7627, arXiv:gr-qc/0607035.

[11] S. Vyatchanin. "Fdt approach calculations of brownian noise in thin layer" (internal LIGO document t040242-00z), http://www.ligo.caltech.edu/docs/T/T040242-00.pdf.

[12] R. O'Shaughnessy, S. Strigin, S. Vyatchanin, "The implications of Mexican-hat mirrors: calculations of thermoelastic noise and interferometer sensitivity to perturbation for the Mexican-hat-mirror proposal for advanced LIGO," (submitted to Phys. Rev. D), arXiv:gr-qc/0409050.

[13] J. Vinet, "Mirror thermal noise in flat-beam cavities for advanced gravitational wave interferometers," Class. Quantum Grav. **22**, 1395 (2005).

[14] M. Born and E. Wolf, *Principles of Optics*, 2nd edition, New York, The MacMillan Company, 1964.

[15] A. G. Fox and T, Li, The Bell System Technical Journal **40**, 453, (1961)

[16] A. Siegman, *Lasers*, Mill Valley, University Science Books, 1986.

[17] P. Savov, J. Agresti, Y. Chen, E. D'Ambrosio, "A duality relation between non-spherical optical cavities and its application to gravitational-wave detectors," arXiv.org:gr-qc/0511062.

[18] LIGO http://www.ligo.caltech.edu/e2e

[19] V. Galdi, G. Castaldi, V. Pierro, I. M. Pinto, J. Agresti, E. D'Ambrosio and R. DeSalvo, "On the analytic structure of a family of hyperboloidal beams of potential interest for future LIGO interferometers," Phys. Rev. D **73**, 127101 (2006) [arXiv:gr-qc/0602074].

[20] J. Durnin, "Exact Solution for nondiffracting beams. I. The scalar theory," J. Opt. Soc. Am. A **4**, 651-654 (1897)

[21] J. Drunin, J. J. Miceli, Jr and J.H. Eberly, "Diffraction-Free Beams," Phys. Rev. Letters **58**, 1499 (1987)

[22] D. McGloin, V. Garcés-Chávez and K. Dholakia " Interfering Bessel beams for optical micromanipulation"

[23] Raúl I. Hernández-Aranda, Sabino Chavéz-Cerda, Julio C. Gutiérez-Vega " Theory of the unstable Bessel Resonator," J. Opt. Soc. Am. A **22**, 1909 (1993)

[24] See Appendix A of this thesis

[25] Giampaolo D'Alessandro, Gian-Luca Oppo "Gauss-Laguerre modes: a sensible basis for laser dynamics" Optics Communications, Vol. **88**, Issues 2-3, 130, (1992)

Chapter 4

Isometric Embeddings of Black Hole Horizons in Three-Dimensional Flat Space

This chapter, with minor modifications, was originally published in [1].

The geometry of a two-dimensional surface in a curved space can be most easily visualized by using an isometric embedding in flat three-dimensional space. Here we present a new method for embedding surfaces with spherical topology in flat space when such a embedding exists. Our method is based on expanding the surface in spherical harmonics and minimizing for the differences between the metric on the original surface and the metric on the trial surface in the space of the expansion coefficients. We have applied this method to study the geometry of back hole horizons in the presence of strong, non-axisymmetric, gravitational waves (Brill waves). We have noticed that, in many cases, although the metric of the horizon seems to have large deviations from axisymmetry, the intrinsic geometry of the horizon is almost axisymmetric. The origin of the large apparent non-axisymmetry of the metric is the deformation of the coordinate system in which the metric was computed.

4.1 Introduction

In the past few years, important progress has been made in the development of fully three-dimensional (3D) numerical relativity codes. These codes are capable of simulating the evolution of strongly gravitating systems, such as colliding black holes and neutron stars, and can provide important physical information about those systems such as the gravitational waves they produce. The codes also allow one to locate and track the evolution of apparent and event horizons of black holes that might exist already in the initial data or might form during the evolution of the spacetime. However, since the location of such horizons is obtained only in coordinate space, one typically has little information about the real geometry of those surfaces. One can, for example, obtain very similar shapes in coordinate space for horizons that are in fact very different (see for example the family of distorted black holes studied in [2]; their coordinate locations are very similar, but their geometries are quite different). The most natural way to visualize the geometry of a black hole horizon, or of any other surface computed in some abstract curved space is to find a surface in ordinary flat space that has the same intrinsic geometry as the original surface. The procedure of finding such a surface is called *embedding* the surface in flat space.

It is a well known fact [3] that any two dimensional surface is *locally* embeddable in flat 3D space. Global embeddings of a surface, on the other hand, might easily not exist, and even when they do they are not easy to find. However, several methods have been proposed in the past for computing partial (or global) embeddings of surfaces when such embeddings exist.

Partial embeddings of a slice through the Misner initial data for colliding black holes [4] have been computed for example in [5]. The method used to find such embeddings starts from the metric of the original surface written in terms of some local coordinates (u, v):

$$ds^2 = Edu^2 + 2Fdudv + Gdv^2 \, . \tag{4.1}$$

One then introduces embedding functions $X(u, v)$, $Y(u, v)$ and $Z(u, v)$ such that

$$dX^2 + dY^2 + dZ^2 = ds^2 = Edu^2 + 2Fdudv + Gdv^2 \, , \tag{4.2}$$

which implies

$$\begin{aligned} E &= X_{,u}^2 + Y_{,u}^2 + Z_{,u}^2 \, , & (4.3)\\ F &= X_{,u}X_{,v} + Y_{,u}Y_{,v} + Z_{,u}Z_{,v} \, , & (4.4)\\ G &= X_{,v}^2 + Y_{,v}^2 + Z_{,v}^2 \, . & (4.5) \end{aligned}$$

The above system of non-linear first order partial differential equations is not of any standard type. In order to solve it one can use a method originally proposed by Darboux. This leads to a single non-linear second order partial differential equation for $Z(u, v)$ known as the Darboux equation. The character of the Darboux equation depends on the sign of the Gaussian curvature K of the surface and on the orientation of the embedding at the point of integration as follows: for $K \geq 0$ the equation is elliptic, for $K \leq 0$ it is hyperbolic and it has parabolic character both if $K = 0$ or if the surface is vertical. For the Misner geometry, the curvature is always negative and the Darboux equation is hyperbolic. It can then be rewritten by using the characteristics as coordinates, and solved as a Cauchy problem given appropriate initial data. Once the Darboux equation has been solved for $Z(u, v)$, the remaining equations can be integrated to give $X(u, v)$ and $Y(u, v)$.

This method is not appropriate for embedding surfaces that have both regions with $K > 0$ and regions with $K < 0$. The reason for this is that the Darboux equation that one has to integrate is elliptic for $K > 0$ and hyperbolic for $K < 0$. This means that for such surfaces the Darboux equation will change type and its integration will become very difficult. This will typically be the case for surfaces with spherical topology, such as black hole horizons, which will always have some regions of positive curvature, and may well have regions of negative curvature too.

One of the first studies of the intrinsic geometry of rotating black hole horizon surfaces was carried out by Smarr [6]. There it was shown, by direct construction of the embedding from the analytic Kerr metric, that while the horizon of a Schwarzschild black hole is spherical, for rotating black holes the horizon has an equatorial bulge, a satisfying and intuitive result that reinforces the notion that geometric studies of black hole horizons can add physical insight. The equatorial bulge can be characterized by an oblateness factor that is uniquely determined by the ratio a/m, where m is the mass of the black hole and a its rotation parameter. It was also shown that for rapidly rotating black holes, with $a/m > \sqrt{3}/2$, the Gaussian curvature becomes negative near the poles, and the surface is not embeddable in Euclidean space, as it is "too flat"!

Extending on this work, using a direct constructive embedding method described below, a number of studies were made of distorted, rotating, and colliding black hole horizons in axisymmetry [7, 2, 8, 9, 10, 11] where it was shown that embeddings are very useful tools to aid in the understanding of the *dynamics* of black holes. For example, distorted rotating black hole horizons were found to oscillate, about their oblate equilibrium shape, at their quasi-normal frequency. The recent work on isolated horizons [12, 13, 14, 15] shows how geometric measurements of the horizon can be used to determine, for example, the spin of a black hole formed in some process, and other physical features.

However, in the absence of axisymmetry, the problem of constructing an embedding for a black hole horizon becomes much more difficult. One approach to compute such embeddings of horizons in 3D spacetimes has been suggested by H.-P. Nollert and H. Herold [16]. They consider a triangular wire frame on the original surface and compute the distances between each point and its neighbors using the intrinsic metric of the surface. They then consider a network with the same topology in flat space and try to solve the system of equations

$$|\mathbf{r}_i - \mathbf{r}_j| = d_{ij} \,, \tag{4.6}$$

where $\mathbf{r}_k$ represents the position vector of the k^{th} point in flat space and d_{ij} represents the distance between the points P_i and P_j computed on the original surface. If necessary, they refine the grid until they reach a desired accuracy.

The approach of Nollert and Herold seems very natural, but is has the serious drawback that it does not always converge to the correct solution. The reason for this is that the method imposes constraints only on the distances between points, but it does not guarantee that the final surface will be smooth. There are in fact multiple solutions to the system of equations, and for most such solutions the resulting embedding is not smooth. For example, if one tries to embed a simple sphere, this method might indeed converge to the sphere, but it might also converge to the surface one obtains if one cuts the top of the sphere, turns its up-side down and glues it back. The distances between point are the same in both surfaces, but only one of them is smooth.

The method for computing embeddings that we present in this paper is based on a spectral decomposition of the surface in spherical harmonics written in a non-trivial mapping of the coordinate system. We search for the embedding by minimizing for the difference between the metric of the original surface and that of our trial embedding in the space of the coefficients of the spherical harmonics and of the coordinate mappings. Since we use a decomposition of the surface in spherical harmonics, the surface is guaranteed to be smooth. By increasing the number of spherical harmonics used in the decomposition of the physical surface, one can get as close to the correct embedding as desired.

4.2 Our Method

The intrinsic geometry of any surface is completely determined by its metric. To construct the embedding of a given surface S, one needs to find a surface S' in flat space that has the same metric as S in an appropriate coordinate system. It is important to stress here the fact that finding the embedding surface S' also requires that one finds an appropriate mapping of the original coordinate system in the surface S to a new coordinate system in the surface S' in which the two metrics are supposed to agree.

4.2.1 A Direct Method for Horizon Embeddings in Axisymmetry

Before describing our new method, it is instructive to describe a simple and direct method for axisymmetric embeddings of horizons, used by a number of authors to study the physics of dynamic black holes [17, 2, 8, 9, 10, 11, 18].

For the case of non-rotating, axisymmetric spacetimes (easily generalized to rotation, but restricted here merely for ease of illustration), the 3D metric on a given time slice can be written as

$$ds^2_{(3)} = A(\eta,\theta)d\eta^2 + B(\eta,\theta)d\theta^2 + D(\eta,\theta)\sin^2\theta d\phi^2. \tag{4.7}$$

The location of the axisymmetric horizon surface is given by the function $\eta = \eta_s(\theta)$. The 2D metric induced on the horizon surface is then given by

$$ds^2_{(2)} = \left[B + \left(\frac{d\eta_s}{d\theta} \right)^2 A \right] d\theta^2 + D \sin^2 \theta d\phi^2 \,. \tag{4.8}$$

Now, the flat metric in cylindrical coordinates (z, ρ, ψ) can be written as

$$ds^2 = dz^2 + d\rho^2 + \rho^2 d\psi^2. \tag{4.9}$$

To create an embedding in a 3D Euclidean space, we want to construct functions $z(\theta, \phi), \rho(\theta, \phi)$, and $\psi(\theta, \phi)$ such that we can identify the line elements given by Eqs. (4.8) and (4.9), that is, that all lengths will be preserved.

Here, we are faced with our first choice about the coordinates used in the embedding, a problem that will be more complex in the general case as we show below. Since the spacetime itself is axisymmetric, it is a natural choice to make the embedding axisymmetric. We choose, then, to construct a surface for a constant value of $\phi = 0$, and we then have $z = z(\theta), \rho = \rho(\theta)$, and the resulting embedding will be a surface of revolution about the $z-$axis. Using the obvious mapping between ψ and ϕ, $\psi = \phi$, it becomes straightforward to derive ordinary differential equations to integrate for $\rho(\theta)$ and $z(\theta)$ along the horizon surface. It is important to emphasize that we have to make a choice about the embedding coordinates, even in this simpler case, as we must in the general case discussed below.

Using this method, embeddings were carried out during the numerical evolution for a variety of dynamic, axisymmetric black hole spacetimes [17, 2, 8, 9, 10, 11, 18]. The evolution of these embeddings were found to be extremely useful in understanding the physics of these systems. We will use some of these results as test cases for the more general method for 3D spacetimes, as detailed in the next section.

4.2.2 Our General Method for Embeddings in Full 3D

Given a coordinate system ξ^i $(i, j = 1, 2)$ on our surface, the first step in looking for an embedding is to find the two dimensional metric g_{ij} of the surface induced by the metric of the three dimensional space h_{ab} $(a, b = 1, 2, 3)$ in which it is defined. The general procedure to find such induced metric is to construct a coordinate basis of tangent vectors $\mathbf{e}_i := \partial_i$ on the surface. The induced metric will then be given by

$$g_{ij}(\theta, \phi) = \mathbf{e}_i(\theta, \phi) \cdot \mathbf{e}_j(\theta, \phi) = h_{ab}\, e^a_i\, e^b_j \,, \tag{4.10}$$

where e^a_i is the component of the vector $\mathbf{e}_i$ with respect to the three dimensional coordinate x^a.

Since the surfaces we are concerned with in this paper (black hole horizons) have spherical topology, we will assume that the three-dimensional metric h_{ab} is given in terms of spherical coordinates (r, θ, ϕ) defined with respect to some origin enclosed by the surface. Furthermore, we will also assume that the surface is a "ray-body" (Minkowski's *strahlkorper* [19], also known as a "star-shaped" region) that is, a surface such that any ray coming from the origin intersects the surface at only one point. Such a property implies that we can choose as a natural coordinate system on the surface simply the angular coordinates (θ, ϕ).

If we take our surface to be defined by the function $r = f(\theta, \phi)$, then it is not difficult to show that the induced metric g_{ij} on the surface will be given in terms of the three-dimensional metric h_{ab} as:

$$\begin{aligned} g_{\theta\theta} &= h_{\theta\theta} + h_{rr} \left(\partial_\theta f\right)^2 + 2 h_{r\theta} \partial_\theta f \, , && (4.11) \\ g_{\phi\phi} &= h_{\phi\phi} + h_{rr} \left(\partial_\phi f\right)^2 + 2 h_{r\phi} \partial_\phi f \, , && (4.12) \\ g_{\theta\phi} &= h_{\theta\phi} + h_{rr} \, \partial_\theta f \partial_\phi f + h_{r\phi} \partial_\theta f + h_{r\theta} \partial_\phi f \, . && (4.13) \end{aligned}$$

Let us now for moment a assume that an embedding of our surface in flat space exists, and let us also introduce a spherical coordinate system (r_e, θ_e, ϕ_e) in flat space. Notice that there is no reason to assume that a point with coordinates (θ, ϕ) in the original surface will be mapped to a point with the same angular coordinates in the embedding. In general, the embedded surface in flat space will be described by the relations

$$r_e = r_e(\theta, \phi) \, , \quad \theta_e = \theta_e(\theta, \phi) \, , \quad \phi_e = \phi_e(\theta, \phi) \, . \qquad (4.14)$$

A crucial observation at this point is that the angular coordinates $\{\theta, \phi\}$ in the original surface still provide us with a *well behaved coordinate system in the embedded surface*, only one that does not correspond directly to the flat space angular coordinates $\{\theta_e, \phi_e\}$, but is instead related to them by the coordinate transformations $\theta_e = \theta_e(\theta, \phi)$ and $\phi_e = \phi_e(\theta, \phi)$. This means that under the embedding, points with coordinates (θ, ϕ) in the original surface will be mapped to points with *the same* coordinates (θ, ϕ) in the embedded surface, but *different* coordinates (θ_e, ϕ_e). We then have two natural sets of coordinates in the embedded surface: the ones inherited directly from the original surface through the embedding mapping, and the standard angular coordinates in flat space.

By definition, an embedding preserves distances, so the proper distance between two points in the original surface must be equal to the distance between the two corresponding points in the embedded surface. Since those corresponding points have precisely the same coordinates $\{\theta, \phi\}$, we must conclude that for the embedding to be correct, the components of the metric tensor in both surfaces when expressed in terms of the coordinates $\{\theta, \phi\}$ must be identical. That is, if we call g^e_{ij}

the metric of the embedded surface, we must have

$$g_{\theta\theta} = g^e_{\theta\theta} \, , \quad g_{\theta\phi} = g^e_{\theta\phi} \, , \quad g_{\phi\phi} = g^e_{\phi\phi} \, . \tag{4.15}$$

It is important to stress that the components of the metric in the embedded surface will only be equal to the components of the metric in the original surface if we use the inherited coordinate system, but not if we use the standard angular coordinates in flat space.

Computing the components of the metric in the embedded surface in terms of the inherited coordinate system $\{\theta, \phi\}$, given the embedding relations (4.14), is not difficult. All one needs to do in practice is to consider four points in the original surface with coordinates $P_1(\theta, \phi)$, $P_2 = (\theta + \delta\theta, \phi)$, $P_3 = (\theta, \phi + \delta\phi)$, $P_4 = (\theta + \delta\theta, \phi + \delta\phi)$, find their corresponding coordinates $\{r_e, \theta_e, \phi_e\}$ in flat space using (4.14), compute their squared distances using the flat space metric, and then solve for the metric components from

$$\begin{aligned}
(\overline{P_1 P_2})^2 &= g^e_{\theta\theta} \, d\theta^2 \, , && (4.16) \\
(\overline{P_1 P_3})^2 &= g^e_{\phi\phi} \, d\phi^2 \, , && (4.17) \\
(\overline{P_1 P_4})^2 &= g^e_{\theta\theta} \, d\theta^2 + g^e_{\phi\phi} \, d\phi^2 + 2 g^e_{\theta\phi} \, d\theta d\phi \, . && (4.18)
\end{aligned}$$

Finding the embedding now means finding a mapping (4.14) such that equations (4.15) are satisfied everywhere.

Let us consider first the relation between the (θ, ϕ) coordinates on the original surface and the angular coordinates (θ_e, ϕ_e) in flat space. Even if these two sets of coordinates are not equal, we can safely assume that there is a one-to-one correspondence between them. Moreover, both are sets of angular coordinates, so they have the same behavior: θ and θ_e go from 0 to π, and ϕ and ϕ_e go from 0 to 2π and are periodic. From these properties, it is not difficult to see that the most general functional relation between both sets has the form

$$\begin{aligned}
\theta_e(\theta, \phi) &= \theta + \sum_{n=0}^{\infty} b_{n0} \sin(n\theta) \\
&\quad + \sum_{n=1}^{\infty} \sum_{m=1}^{\infty} b_{nm} \sin(n\theta) \, \sin(m\phi) \, , && (4.19) \\
\phi_e(\theta, \phi) &= \phi + c_{00} \, \theta + \sum_{n=1}^{\infty} c_{n0} \sin(n\theta) + \sum_{m=1}^{\infty} c_{0m} \sin m\phi \\
&\quad + \sum_{n=1}^{\infty} \sum_{m=1}^{\infty} c_{nm} \sin(n\theta) \, \sin(m\phi) \, . && (4.20)
\end{aligned}$$

The second term in the expansion for θ_e represents a general axisymmetric re-mapping of θ, while the third term is required if axisymmetry is not assumed. In the expression for ϕ_e, the second and third terms represent a possible rigid twist of the coordinate system, and the last two terms stand for a general dependence of ϕ_e on both θ and ϕ.

For the radial coordinate r_e, it is also not difficult to see that one can use a simple expansion in spherical harmonics of the form

$$r_e(\theta,\phi) = \sum_{l=0}^{\infty} \sum_{m=-l}^{l} \sqrt{4\pi}\, a_{lm} Y_{lm}(\theta,\phi)\,, \tag{4.21}$$

where the overall normalization factor of $\sqrt{4\pi}$ has been inserted so that a_{00} is the average radius of the surface, a_{10} is its average displacement in the z-direction, and so on. We will also use a real basis of spherical harmonics, for which m and $-m$ stand for an angular dependence $\cos(m\phi)$ and $\sin(m\phi)$, instead of the complex $\exp(im\phi)$ and $\exp(-im\phi)$.

The metric of the embedded surface will now be completely determined by the set of coefficients a_{lm}, b_{nm} and c_{nm}. The space of these coefficients can be regarded as a vector space V, with any given point in V representing a surface in flat space together with a certain coordinate mapping.

Consider now an *embeddable* surface S in some arbitrary curved space. It is not difficult to find a real valued function F defined on V that has a global minimum at the point $P \in V$ for which the metric of the embedded surface S^e is the same as the metric of the original surface. One such function is

$$\begin{aligned} F = \int_{\theta=0}^{\pi} \int_{\phi=0}^{2\pi} \quad & \Big[\left(g_{\theta\theta}(\theta,\phi) - g^e_{\theta\theta}(\theta,\phi)\right)^2 \\ & + \left(g_{\phi\phi}(\theta,\phi) - g^e_{\phi\phi}(\theta,\phi)\right)^2 \\ & + \left(g_{\theta\phi}(\theta,\phi) - g^e_{\theta\phi}(\theta,\phi)\right)^2 \Big] \; d\theta d\phi\,. \end{aligned} \tag{4.22}$$

We call the function F above the “embedding” function. It is easy to see that $F \geq 0$ on any point in V, and that $F = 0$ if and only if $g = g^e$ for all (θ,ϕ). The embedding then corresponds to the absolute minimum of F in V. There are many different numerical algorithms for finding minima of general functions in multidimensional spaces. In our code we have used Powell’s minimization algorithm [20], but we are aware that other methods might perform better. It is important to mention that the definition of the embedding function F above is by no means unique. Many different forms for F can be constructed, in particular, one could take into account the fact that not all metric functions have similar magnitudes and construct an embedding function that normalizes each term in the above expression.

One of the problems with minimization algorithms in general is that they cannot distinguish between a global minimum (what we really want) and a local minimum. In our case, the value of F

at the absolute minimum is zero, so we can easily distinguish between a real embedding and a wrong solution that might appear if the minimization algorithm gets stuck in a local minimum. However, steering the algorithm toward the global minimum is non-trivial. From experience we have seen that local minima for which $F \neq 0$ do exist for our problem. In order to avoid them, we have found it necessary to run first the minimization algorithm with a small number of coefficients a, b, and c, and then increase the number of coefficients one by one until we find a good solution. This method is certainly time consuming, but it seems to work well in the examples we have considered so far.

Of course, in order to find a "perfect" embedding, one would have to push the number of coefficients all the way to infinity. This is numerically impossible, so in practice we just set up a given tolerance in the value of the function F and increase the number of coefficients until we achieve that tolerance. We also check that the value of F goes to zero exponentially as we increase the total number of coefficients. We have seen that $n = l \sim 14$ is enough for relatively simple surfaces like most black hole horizons. If one wants to embed something more complicated (like a human face, for example) starting from its metric in some coordinate system, this value would clearly be too small. Another way to see whether an embedding is good or not is to compare directly the metric of the original surface with the metric of the resulting embedding. If the fit is good enough, the code has converged to the correct embedding.

One important test we have used for our algorithm is a direct comparison of the results obtained with our code with embeddings computed with a different code in the special case when the surface is axisymmetric.

4.3 Tests

4.3.1 Recovering a Known Surface

A very simple test for our algorithm is to look for the embedding of a surface that is known to be embeddable and has a known embedding. In order to do this we first construct a surface in flat space by choosing some arbitrary values of the spherical harmonic coefficients. We then compute the metric of this surface in the standard (θ, ϕ) angular coordinates, and give this metric as input to our code. The code must then recover the correct values of the spherical harmonic coefficients *plus* a trivial mapping of the angular coordinates.

We show an example of this in Fig. 4.1, where we have chosen a surface defined by the spherical harmonic coefficients:

$$a_{00} = 9 \,, \quad a_{22} = 1 \,, \quad a_{44} = 4 \,, \tag{4.23}$$

with all other coefficients equal to zero. In the upper panel of the figure we show the original surface, and in the lower panel the resulting embedding. The differences in the shape of the two surfaces are

Table 4.1: Comparison of the recovered expansion coefficients for the embedding of the test surface described in the text.

Expansion coefficient	Original value	Recovered value
a_{00}	9	$9 + 1.1 \times 10^{-5}$
a_{20}	0	-3.6×10^{-5}
a_{22}	1	$1 + 4 \times 10^{-6}$
a_{40}	0	1.5×10^{-5}
a_{42}	0	-2.24×10^{-5}
a_{44}	2	$2 + 1.9 \times 10^{-5}$

very difficult to see.

For this test we have used 100 × 100 grid points to describe the surface. Since the surface is symmetric with respect to reflections on all three (x, y, z) coordinate planes, we have considered only one octant, so the angular resolution was $\Delta\theta = \Delta\phi = \pi/200$. The recovered expansion coefficients are shown in Table 4.1. The coefficients corresponding to the mapping of the angular coordinates, as well as the rest of the Y_{lm} coefficients were either exactly zero because of the octant symmetry or had values smaller than 10^{-3}.

Figure 4.2 shows a direct comparison of the metric components $g_{\theta\theta}$, $g_{\theta\phi}$ and $g_{\phi\phi}$ along the lines $\theta = \pi/4$ and $\phi = \pi/4$, i.e in the middle of the computational domain.

The final value for the embedding function in this test was $F = 1.6 \times 10^{-5}$, but we have found that we can easily decrease this value by refining the numerical grid on the surface.

4.3.2 An Axisymmetric Example: Rotating Black Holes

As already mentioned in section 4.1, a well-known set of axisymmetric surfaces whose embeddings have been studied, first by Smarr [6], and also as a test case in [16], is that of the horizons of rotating

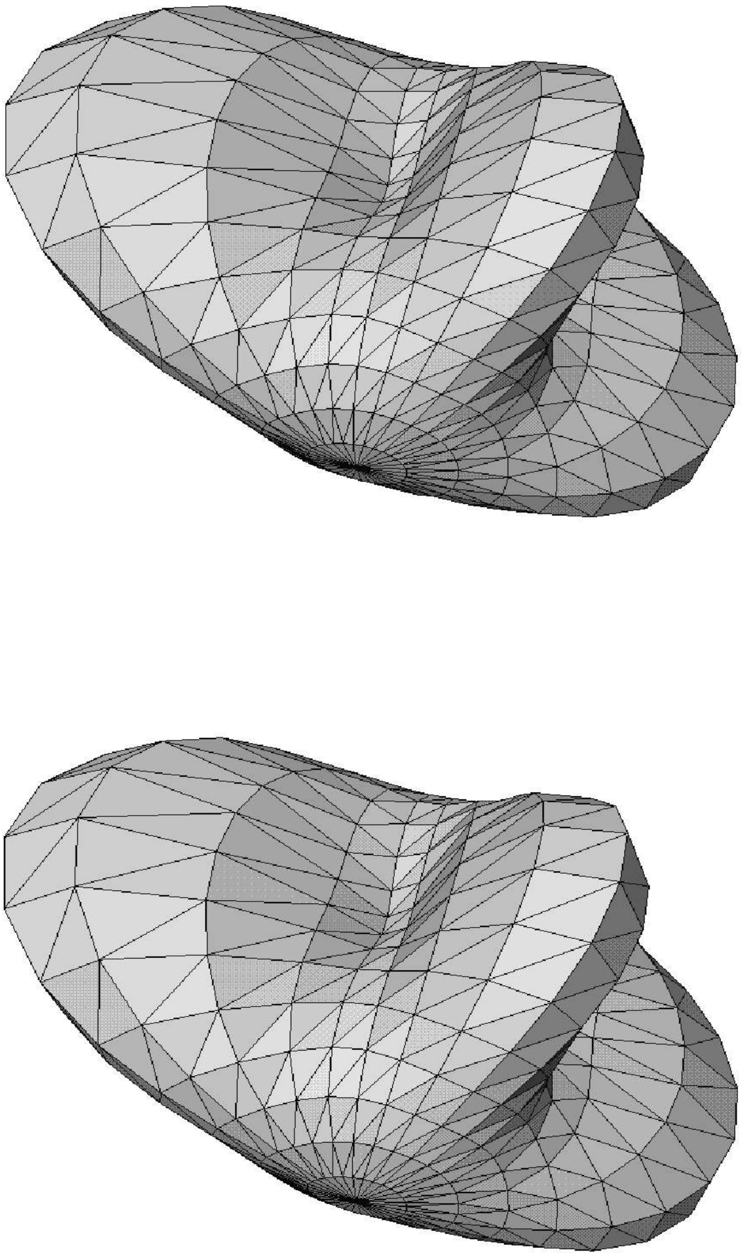

Figure 4.1: Embedding of a test surface defined by the spherical harmonic coefficients ($a_{00} = 9$,$a_{22} = 1$,$a_{44} = 4$). The upper panel shows the original surface and the lower panel the resulting embedding.

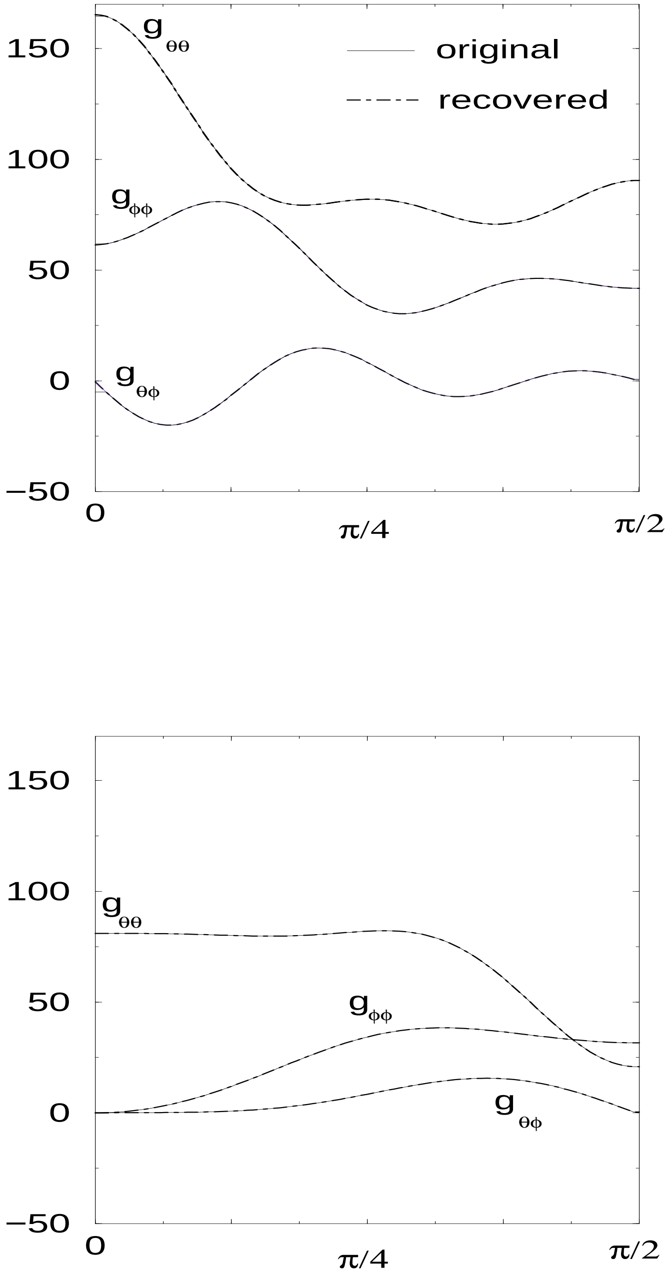

Figure 4.2: The difference in the metric components for the embedding of the test surface described in the text. On the left panel we show the line $\theta = \pi/4$ and on the right panel the line $\phi = \pi/4$.

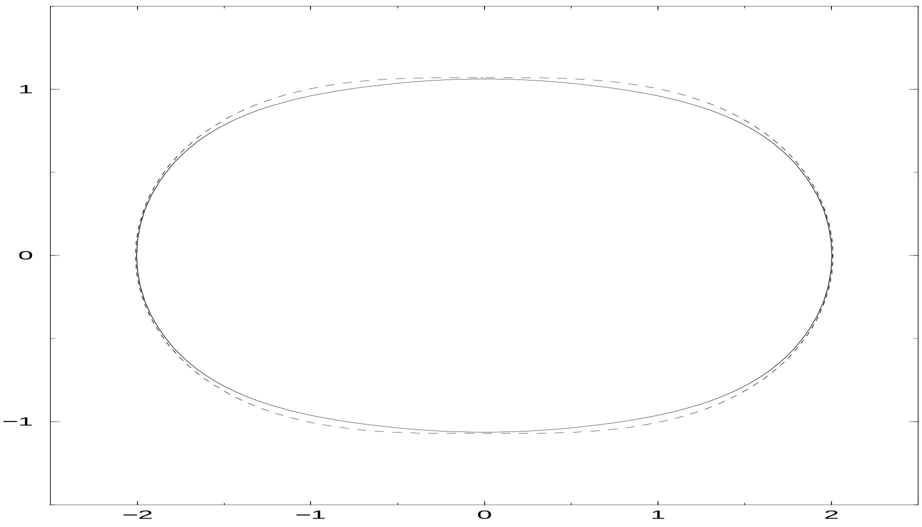

Figure 4.3: Embedding of a Kerr black hole with $a/m = \sqrt{3}/2$. The dotted line is the embedding we obtained using our minimization algorithm. The solid line is an embedding of the same surface computed with an axisymmetric algorithm.

black holes. In the static Kerr case, the metric of the horizon is given by

$$d\sigma^2 = \rho^2 \, d\theta^2 + \frac{\sin^2\theta}{\rho^2} \left(r^2 + a^2\right) d\phi^2 \, , \tag{4.24}$$

with

$$\rho^2 = r^2 + a^2 \cos^2\theta \, , \quad r = m + \sqrt{m^2 - a^2} \, , \tag{4.25}$$

and where m and a are two parameters representing the mass of the black hole and its angular momentum respectively.

It is well known that the Kerr horizon is globally embeddable in flat space only for $a/m \leq \sqrt{3}/2$ [6]. Using our embedding code, we have been able to successfully recover these embeddings when they exist. As an example we show in Fig. 4.3 the embedding obtained for the last embeddable case $a/m = \sqrt{3}/2$. The solid line shows the embedding obtained with the axisymmetric algorithm described above, and the dotted line the one obtained with our minimization algorithm.

When $a/m \geq \sqrt{3}/2$, a global embedding does not exist, and our method fails as expected. Figure 4.4 shows the result of an attempt to embed a Kerr black hole horizon in the case when $a/m = 0.99$. The dotted line is the output of our minimization algorithm and the solid line is an embedding of the same surface made with an axisymmetric algorithm in the embeddable region, plus a flat top in the region where the embedding does not exist. The axisymmetric method is a *local* constructive method, and hence it is able to build the embedding surface from one point to the next where it exists (in this case starting from the equator). Since our method is *global* we get the embedding wrong everywhere. As currently implemented, our method will insist on trying to find a global embedding, and will settle on a shape that minimizes the function F. If the embedding does not exist, the minimum value of F found will be clearly different from zero. This is easily seen by examining the residual function F for the embeddings of the Kerr horizons. In Fig. 4.5 we show the value of the minimum of F found with our algorithm, plotted against the total number of expansion coefficients, for the cases $a/m = \sqrt{3}/2$ (solid line) and $a/m = 0.99$ (dotted line). One can see that for the non-embeddable case, F stops decreasing at a value that is more than 2 orders of magnitude larger than the one we obtain when the embedding exists.

Our code might be adjusted in the future for finding partial embeddings by reducing the integration domain in the definition of F, Eq. (4.22), to something smaller than the full sphere. This approach might lead to correct partial embeddings of surfaces that cannot be embedded globally. The disadvantage would be that one would have to guess the domain where the embedding exits before starting the computation.

4.3.3 Black Hole Plus Brill Wave

We now move to the case of numerically generated, distorted black holes. Schwarzschild black holes distorted by Brill waves [21] have been extensively studied in numerical relativity [22, 23, 24, 25]. The axisymmetric data sets used for numerical evolutions consist of a Schwarzschild black hole distorted by a toroidal, time-symmetric gravitational wave.

It is convenient to describe the metric of the black hole plus Brill wave spacetime in a spherical-polar like coordinate system (η, θ, ϕ) were η is a logarithmic radial coordinate defined by $\eta = \ln(2r/M)$ and (θ, ϕ) are the standard angular coordinates. In these coordinates, the spatial metric has the form [7, 24]

$$dl^2 = \Psi^4 \left[e^{2q} \left(d\eta^2 + d\theta^2 \right) + r^2 \sin^2 \theta d\phi^2 \right] \, , \tag{4.26}$$

where both q and Ψ are functions of η and θ only. In order to satisfy the appropriate regularity and fall-off conditions, the function q has been chosen in the following way

$$q(\eta, \theta) = a \sin^n \theta \left[e^{-\left(\frac{\eta+b}{\omega}\right)^2} + e^{-\left(\frac{\eta-b}{\omega}\right)^2} \right] \, , \tag{4.27}$$

where n is an arbitrary even number larger than 0. The parameter a characterizes the amplitude of the Brill wave, while the parameters b and ω characterize its radial location and width respectively. Having chosen the form of the function q, the hamiltonian constraint is solved numerically for the

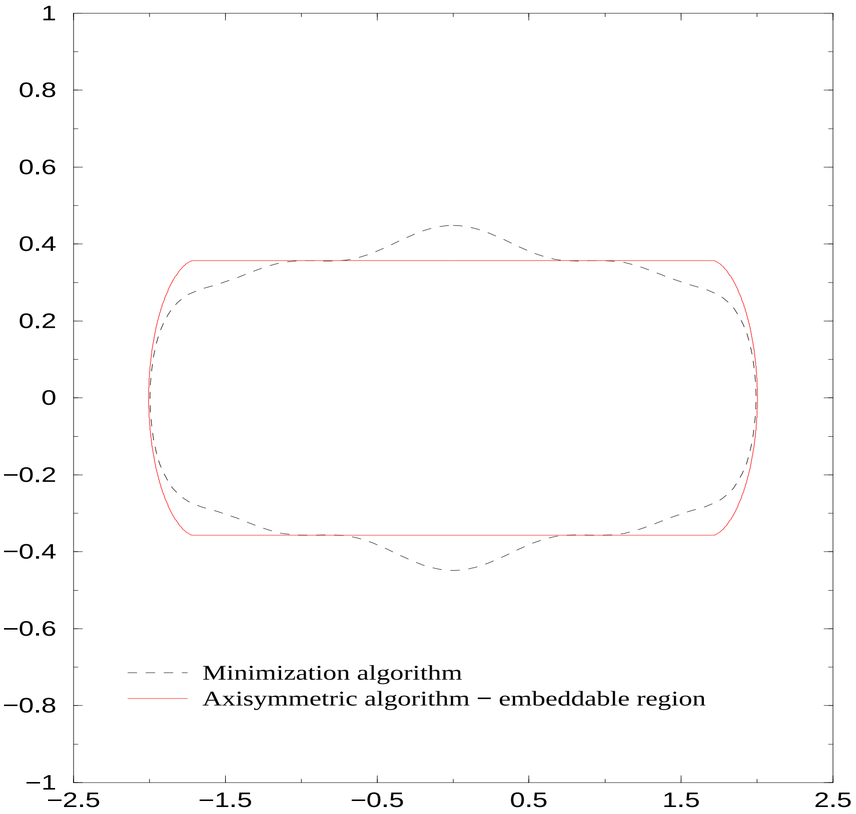

Figure 4.4: An attempt to embed a Kerr black hole horizon with $a/m = 0.99$. The dotted line is the output of the minimization algorithm. The solid line is an embedding of the same surface made with an axisymmetric algorithm. The flat line on the top represents the region where an embedding in flat space does not exist.

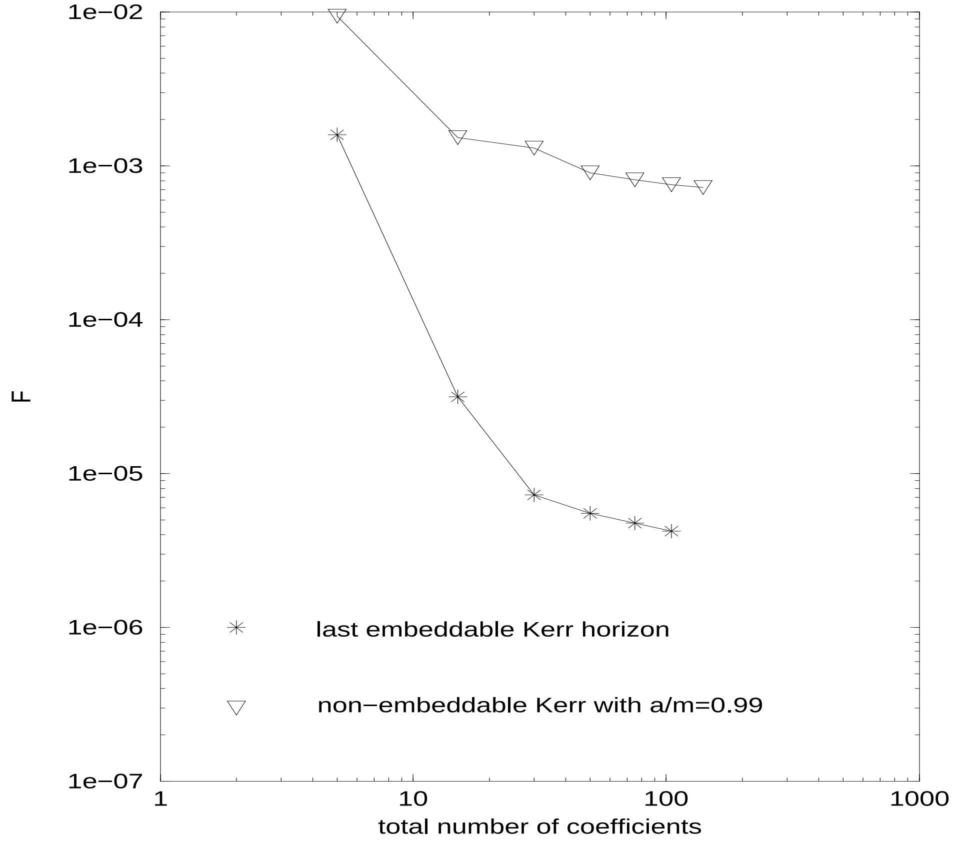

Figure 4.5: The value of the embedding function F versus the total number of coefficients for the two Kerr black holes discussed above. The triangles correspond to $a/m = 0.99$ and the stars to $a/m = \sqrt{3}/2$.

conformal factor Ψ. An isometry condition is imposed at a coordinate sphere to guarantee that the final spacetime will contain a black hole.

Notice that the metric (4.26) is the three-dimensional metric of space, and not the two-dimensional metric of the apparent horizons. The apparent horizons for these data sets have to be located numerically. Once these horizons are found, their two-dimensional metric can be computed from the three-dimensional metric given above, using the expressions given in (4.13).

The horizons from these axisymmetric black hole plus Brill wave data sets and their embeddings have been studied previously in [24] and we have been able to reproduce their results using our algorithm. An example of this can be seen in Fig. 4.6, where we show the embedding of the horizon of a black hole plus Brill wave data set corresponding to the parameters

$$a = 1.0\,, \quad b = 0.0\,, \quad w = 1.0\,, \quad n = 2\,. \tag{4.28}$$

In the figure, the dotted line shows the embedding obtained with our minimization algorithm, and the solid line shows the embedding of the same surface obtained in [24]. Notice how the intrinsic geometry of the horizon is far from spherical.

4.3.4 Application to Full 3D Spacetimes

Having tested our algorithm on both analytic and numerically generated axisymmetric black hole spacetimes, we now turn to the case of full 3D black hole spacetimes for which our method was developed.

The axisymmetric black hole plus Brill wave data sets from [24] have been generalized in [27] to full 3D by multiplying the Brill wave function q by a factor that has azimuthal dependence to obtain

$$\begin{aligned} q(\eta,\theta,\phi) \quad &= \quad a \sin^n \theta \, \left(1 + c \, \cos^2 \phi\right) \\ & \qquad \left[e^{-\left(\frac{\eta+b}{\omega}\right)^2)} + e^{-\left(\frac{\eta-b}{\omega}\right)^2} \right] \, , \end{aligned} \tag{4.29}$$

where c is an arbitrary parameter characterizing the non-axisymmetry of the Brill wave.

We have computed embeddings of the non axisymmetric apparent horizons obtained in this case. Here we will show examples of two such horizons. First we consider the embedding of the apparent horizon for the data set with parameters

$$a = 0.3\,, \quad b = 0.0\,, \quad \omega = 1.0\,, \quad n = 4\,, \quad c = 0.4\,, \tag{4.30}$$

which corresponds to a relatively small non-axisymmetric distortion of the black hole. Figure 4.7 shows the embedding of the corresponding apparent horizon. Notice how the surface looks quite

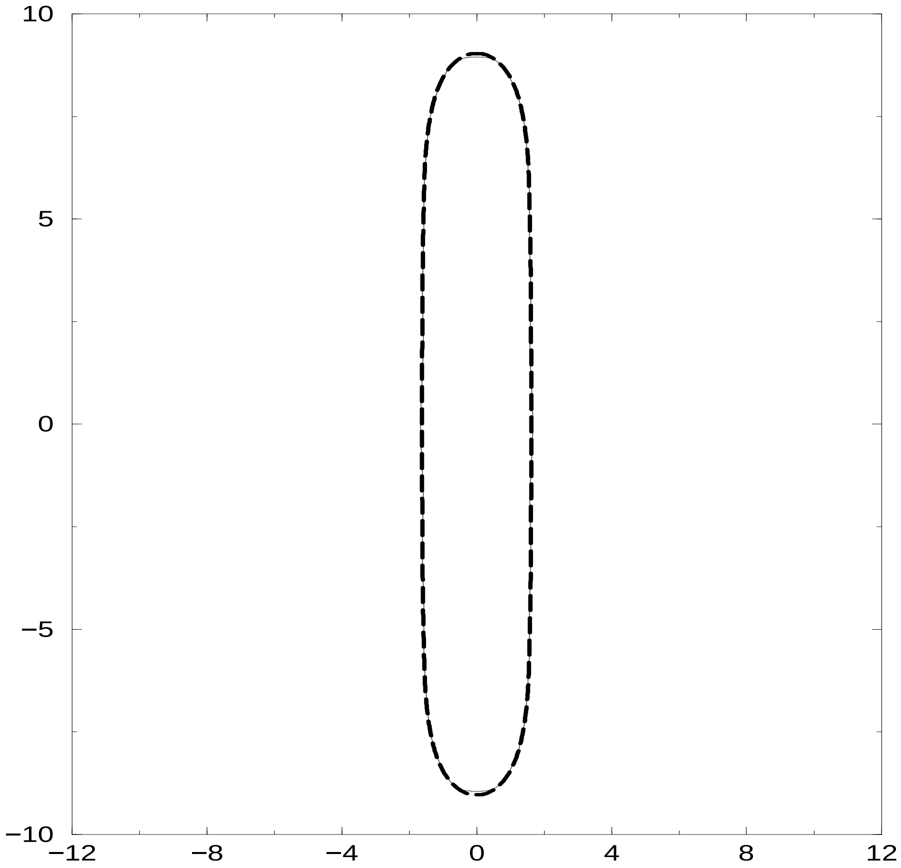

Figure 4.6: Embedding of the apparent horizon of a black hole plus Brill wave data set corresponding to the parameters ($a = 1.0, b = 0.0, \omega = 1.0, n = 2$). The dotted line is the embedding obtained with our minimization algorithm and the solid line the embedding of the same surface obtained by Anninos et al.

axisymmetric even though we have added a non-trivial non-axisymmetric contribution to the metric. It is clear that the non-axisymmetry of the metric components is to a large degree a coordinate effect. Numerical evolutions of such black holes do show radiation in non-axisymmetric modes of gravitational radiation. However the mass energy carried away by the non-axisymmetric modes is much smaller than the energy of the axisymmetric modes [28, 22]. This is consistent with our result showing that the horizon is almost axi-symmetric.

Figure 4.8 shows a direct comparison of the different angular metric components on the apparent horizon and the resulting embedding, along the $\phi = \pi/4$ and $\theta = \pi/4$ lines. We can see how the fit is very good in both cases. Notice also that there is indeed some dependence of the metric components on ϕ.

To check if our algorithm is converging to the correct embedding, we show in Fig. 4.9 the value of the embedding function F at the minimum, in terms of the total number of expansion coefficients. We clearly see that the value of F is converging exponentially to zero.

As a second example, we now consider the embedding of the apparent horizon corresponding to the black hole plus Brill wave data set with parameters

$$a = 0.3\,, \quad b = 0.0\,, \quad \omega = 1.0\,, \quad n = 4\,, \quad c = 1.9\,. \tag{4.31}$$

In this case, the non-axisymmetry is considerably larger, and one can see from Fig. 4.10 that the horizon is clearly not axisymmetric.

In Fig. 4.11 we show again a direct comparison of the angular metric components on the apparent horizon and the resulting embedding along the $\phi = \pi/4$ and $\theta = \pi/4$ lines. As before, the fit is very good.

Finally, in Fig. 4.12 we show again the value of the embedding function F at the minimum in terms of the number of expansion coefficients. As before, the value of F converges exponentially to zero, but the convergence is slower than in the previous example due to the higher degree of complexity of the surface.

4.4 Conclusions

We have implemented and tested a new algorithm for computing isometric embeddings of curved surfaces with spherical topology in flat space. We define a function on the space of surfaces that has a global minimum for the right embedding and we find this minimum using a standard minimization algorithm. In this paper we have discussed the method and its applications to black hole visualization in numerical relativity. The method has been tested both on simple test surfaces and on Kerr black hole horizons, and shown to correctly reproduce known results within specified tolerances. We have

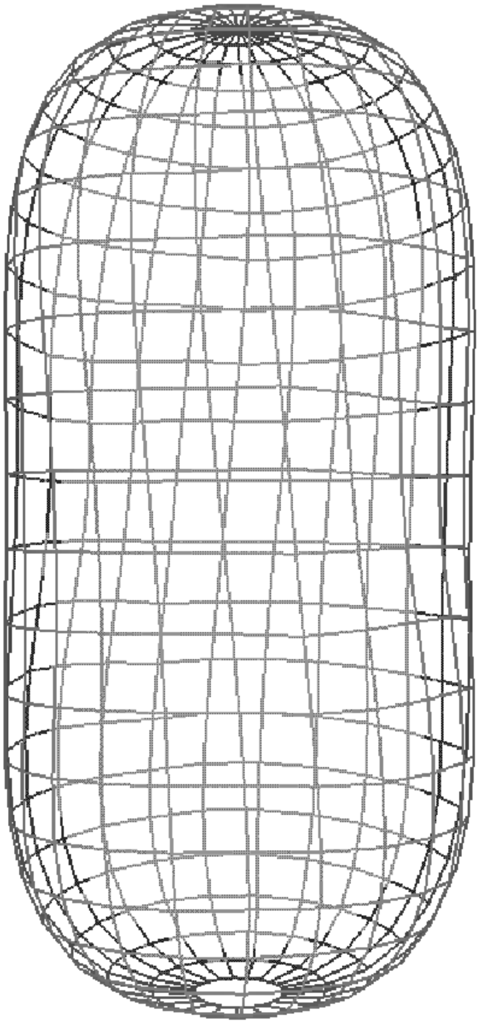

Figure 4.7: Embedding of the apparent horizon for the non axisymmetric black hole plus Brill wave data set corresponding to the parameters $(a = 1.0, b = 0.0, \omega = 1.0, n = 4, c = 0.4)$. Although the metric has a non-trivial non-axisymmetric contribution, the surface looks quite axisymmetric.

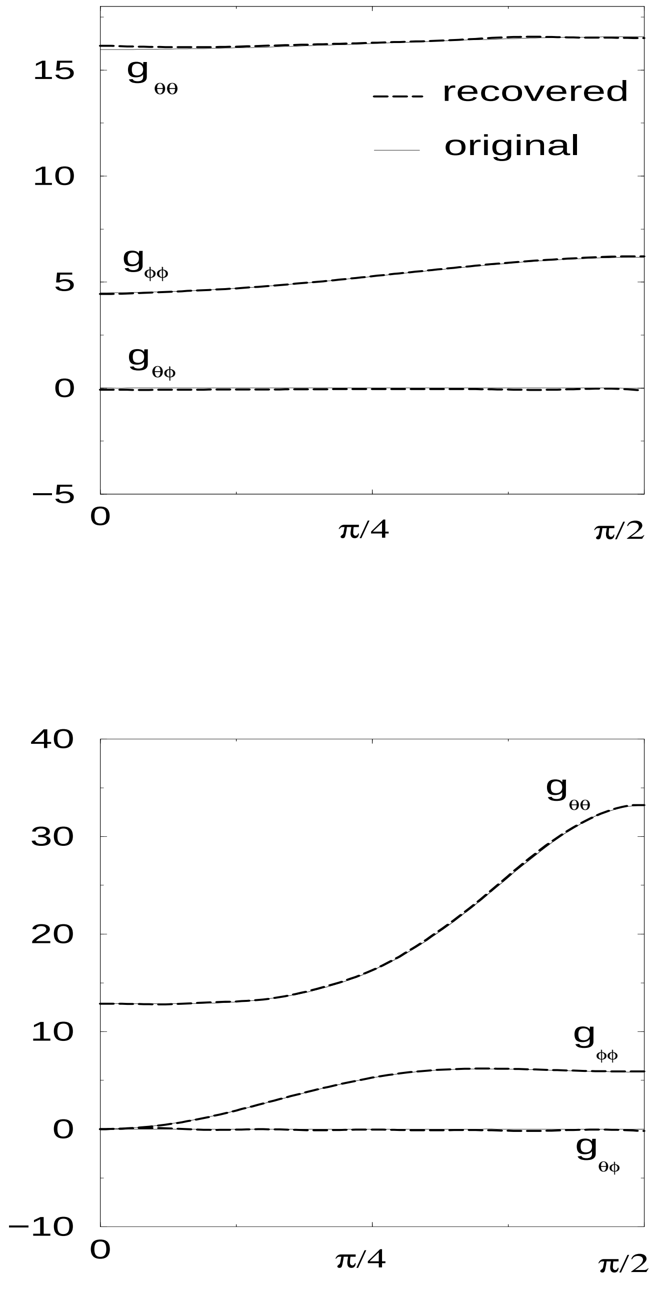

Figure 4.8: We show the angular metric components on the apparent horizon and on the resulting embedding for the black hole plus Brill wave data set corresponding to the parameters ($a = 1.0, b = 0.0, \omega = 1.0, n = 4, c = 0.4$). On the left panel we show the line $\theta = \pi/4$ and on the right panel the line $\phi = \pi/4$.

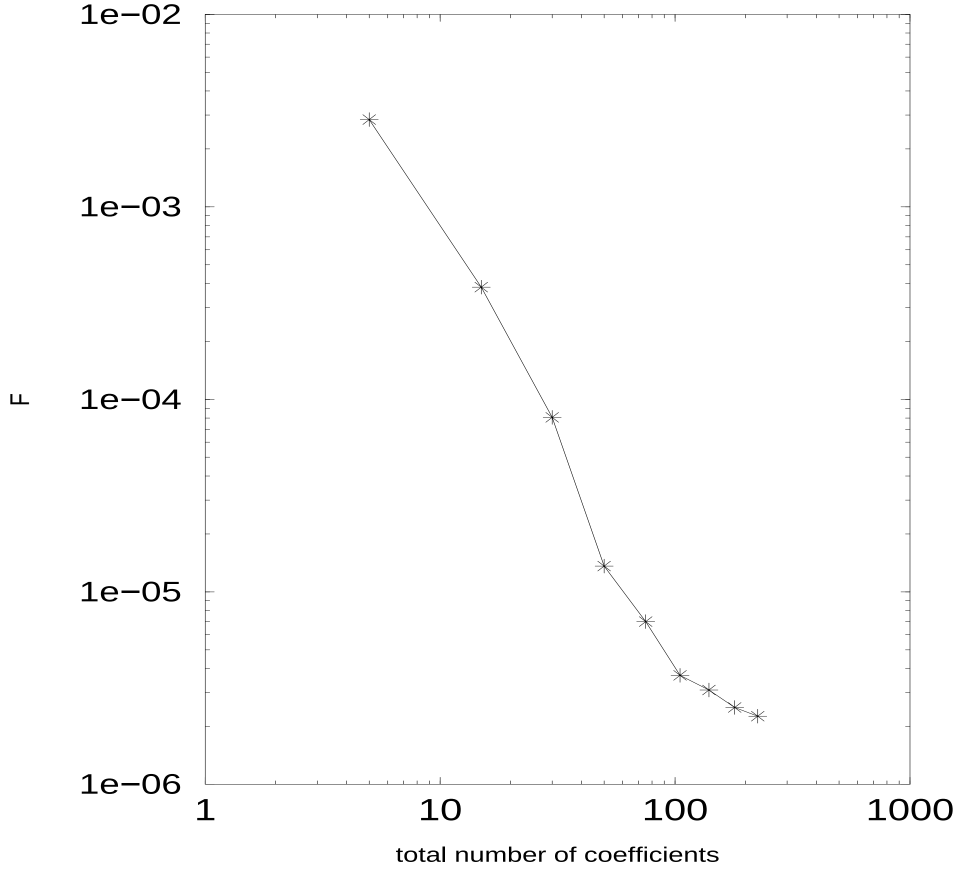

Figure 4.9: We show the value of the embedding function F at the minimum in terms of the total number of expansion coefficients in a logarithmic scale for the black hole plus Brill wave data set corresponding to the parameters $(a = 1.0, b = 0.0, \omega = 1.0, n = 4, c = 0.4)$.

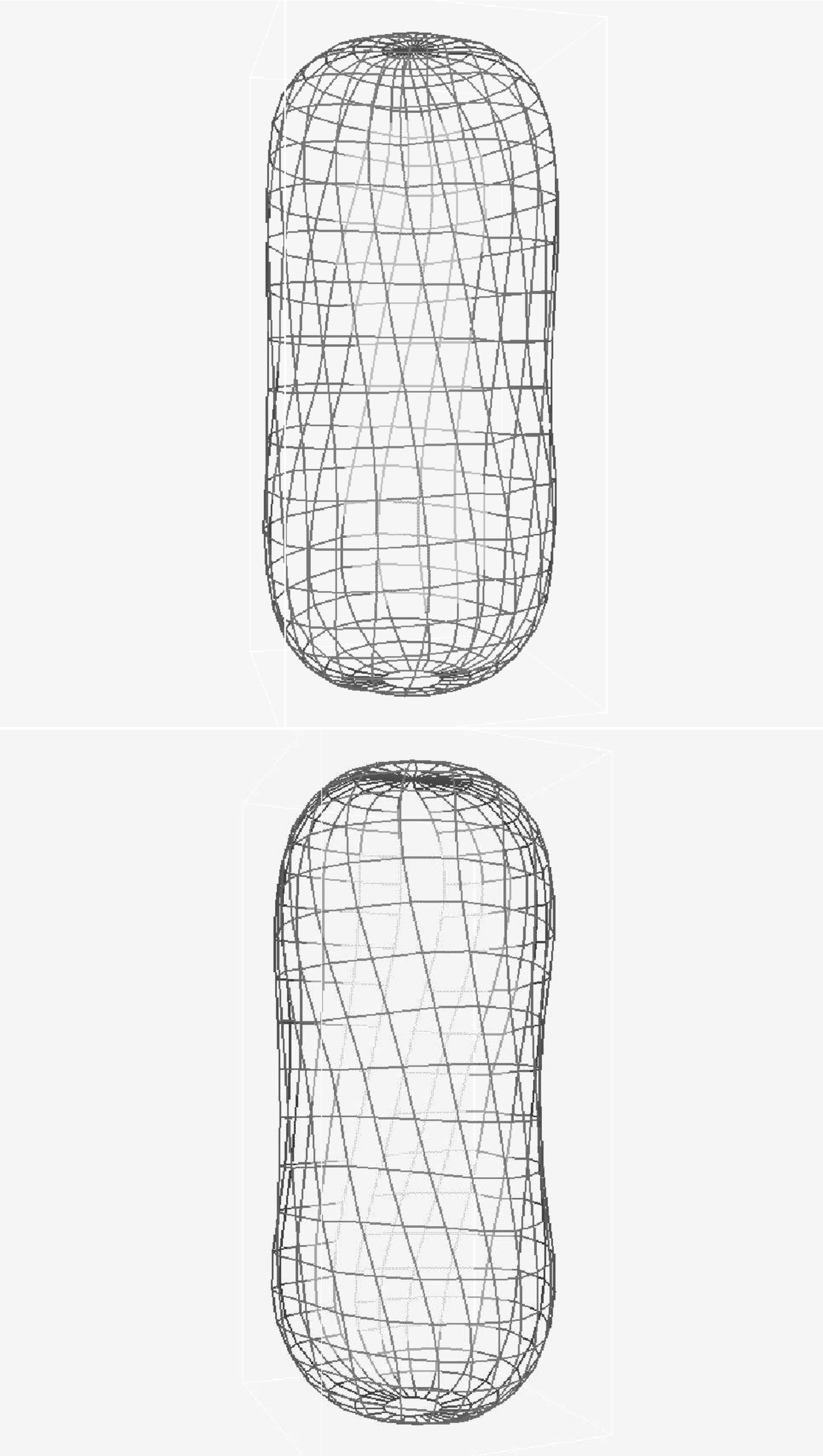

Figure 4.10: Two orientations of the embedding of the apparent horizon of a black hole perturbed by a Brill wave with a higher non-axisymmetry than in the previous example.

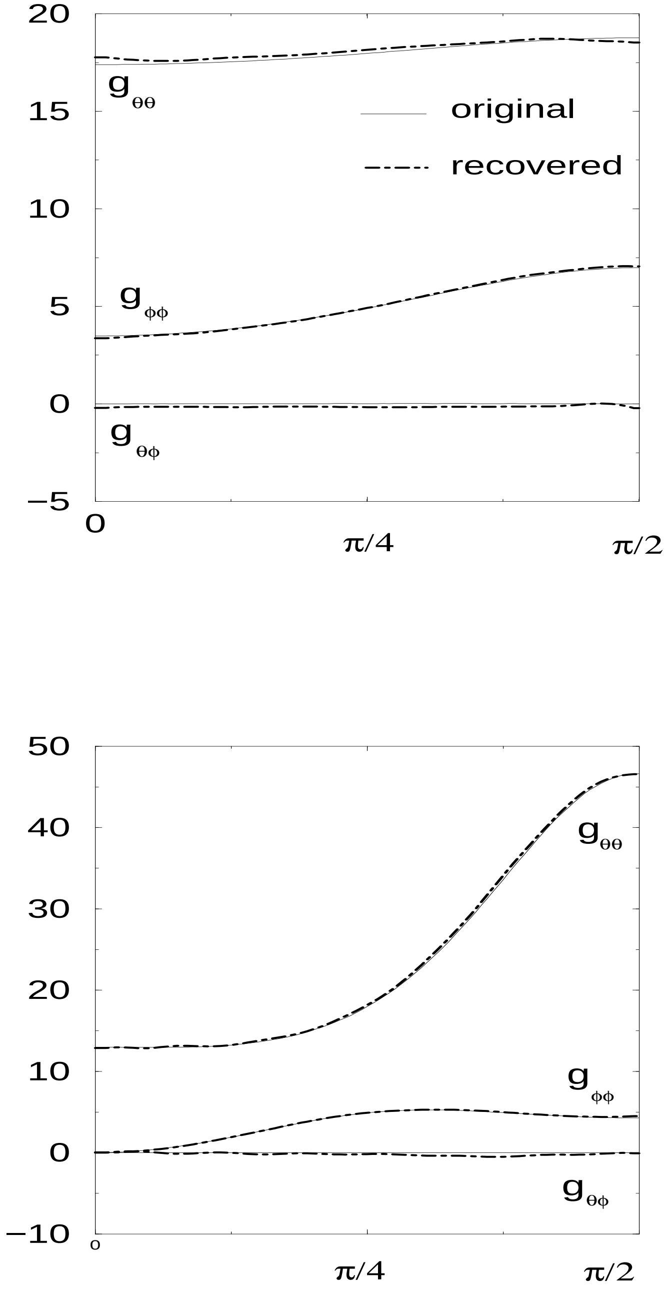

Figure 4.11: The three independent components of the metric for the black hole plus Brill wave will a larger non-axisymmetric perturbation. On the left panel we show the line $\theta = \pi/4$ and on the right panel the line $\phi = \pi/4$.

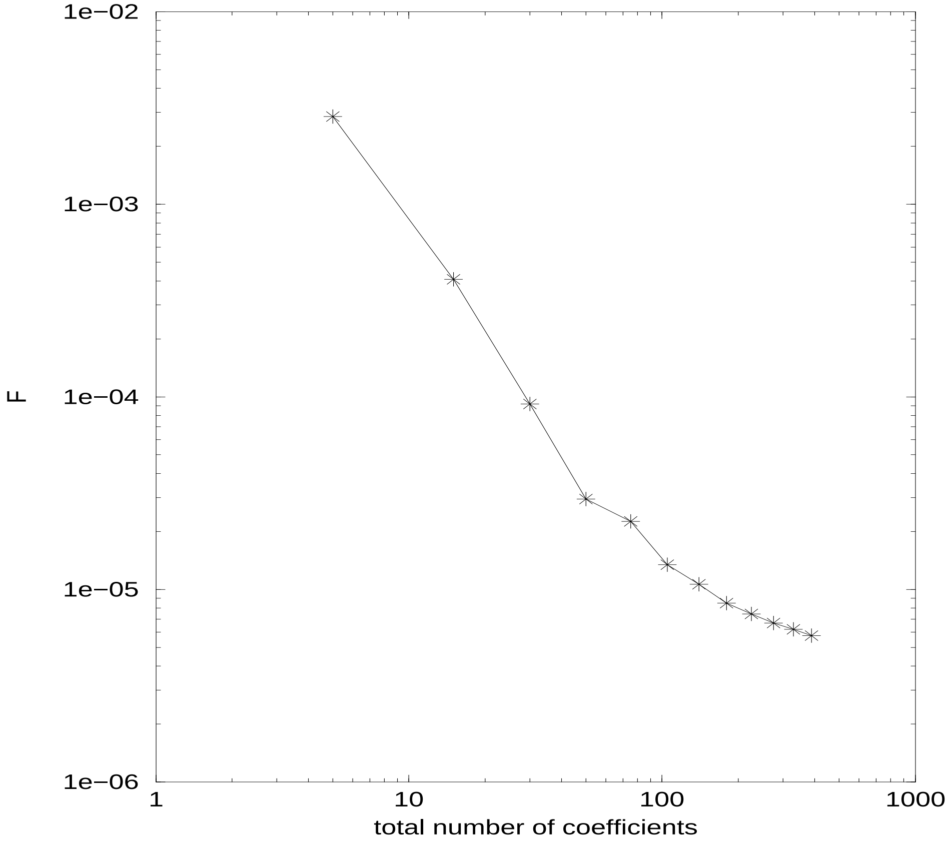

Figure 4.12: The value of the embedding function F at the minimum in terms of the total number of expansion coefficients on a logarithmic scale for the black hole plus Brill wave with a larger non-axisymmetric contribution.

also used our method construct embeddings of non-axisymmetric, distorted black holes for the first time. We observed that the non-axisymmetry of the embedded surface is somehow smaller than one expects from just looking at the metric. This is consistent with the small amount of gravitational radiation emitted in non-axisymmetric modes during the numerical evolution of such systems [22, 28].

Our method is rather robust, and by construction produces smooth surfaces, therefore avoiding some of the problems of previous methods. One disadvantage of our method is that the expansion in spherical harmonics implies that it can only be used to embed ray-body surfaces (i.e. surfaces such that any ray coming from the origin intersects the surface at only one point), still we expect most black hole horizons to have this property. The main disadvantage, however, is that the method is very time consuming due to the fact that minimization algorithms in general are slow. Another problem is the fact that minimization algorithms can easily get trapped in local minima. In order to avoid this we have found it necessary to increase the number of coefficients one by one and to use at each step the result of the previous step as initial guess, adding to the total amount of time the algorithm needs to find the embedding. As presently implemented, it also cannot find partial embeddings when no global embeddings exist, but straightforward modifications to the algorithm should permit this in certain cases.

In the future, we will apply this method to study the dynamics of 3D black hole horizons as a tool to aid in understanding the physics of such systems. Although our method has been applied in this paper only to apparent horizons, it can clearly be applied to obtain embeddings of event horizons as well, once they have been located in numerical evolutions.

Our embedding algorithm has been implemented as a thorn in the Cactus code [26], and is available to the community upon request from the authors.

Acknowledgements

The authors would like to thank C. Cutler, D. Vulcanov and A. Rendall for many helpful discussions. We are also grateful to R. Takahashi for suppling some of the horizon data used in the embeddings and to P. Diener for speeding up our code by changing the way in which we computed Legendre polynomials. We are specially thankful to W. Benger for modifying the visualization package Amira so that it can be used for the three-dimensional visualization of embeddings.

Bibliography

[1] M. Bondarescu, M. Alcubierre and E. Seidel, "Isometric embeddings of black hole horizons in three-dimensional flat space," Class. Quant. Grav. **19**, 375 (2002) [arXiv:gr-qc/0109093].

[2] P. Anninos *et al.*, "Dynamics of black hole apparent horizons," Phys. Rev. D **50**, 3801 (1994).

[3] M. Berger and B. Gostiaux, *Differential Geometry: Manifolds, Curves and Surfaces*, Springer-Verlag, New York, 1998.

[4] C. Misner, "Wormhole Initial Conditions," Phys. Rev. D **118**, 1110 (1960).

[5] J. D. Romano and R. H. Price, "Embedding Initial Data for Black-Hole Collisions," Class. Quantum Grav. **12**, 875 (1995).

[6] L. L. Smarr, "Surface Geometry of Charged Rotating Black Holes," Phys. Rev. D **7**, 289 (1973).

[7] D. Bernstein, Ph.D. thesis, University of Illinois Urbana-Champaign, 1993.

[8] P. Anninos *et al.*, "Visualizing black hole space-times," IEEE Computer Graphics and Applications **13**, 12 (1993).

[9] P. Anninos *et al.*, "Dynamics of Apparent and Event Horizons," Phys. Rev. Lett. **74**, 630 (1995).

[10] P. Anninos *et al.*, in *The Seventh Marcel Grossmann Meeting: On Recent Developments in Theoretical and Experimental General Relativity, Gravitation, and Relativistic Field Theories*, R. T. Jantzen, G. M. Keiser, and R. Ruffini editors, pp. 648, World Scientific, Singapore, 1996.

[11] P. Anninos *et al.*, "Oscillating apparent horizons in numerically generated spacetimes," Australian Journal of Physics **48**, 1027 (1995).

[12] A. Ashtekar, C. Beetle, and S. Fairhurst, "Isolated Horizons: A generalization of black hole mechanics," Class. Quantum Grav. **16**, L1 (1999).

[13] A. Ashtekar, C. Beetle, and S. Fairhurst, "Mechanics of isolated horizons," Class. Quantum Grav. **17**, 253 (2000).

[14] A. Ashtekar *et al.*, “Generic Isolated Horizons and Their Applications,” Phys. Rev. Lett. **85**, 3564 (2000).

[15] A. Ashtekar, C. Beetle, and J. Lewandowski, “Mechanics of rotating isolated horizons,” Phys. Rev. D **64**, 044016 (2001).

[16] H.-P. Nollert and H. Herold, in *Relativity and Scientific Computing*, edited by F. W. Hehl, R. A. Puntigam, and H. Ruder, pp. 330, Springer Verlag, Berlin, 1998.

[17] D. Bernstein *et al.*, “Numerically generated axisymmetric black hole spacetimes: Numerical methods and code tests,” Phys. Rev. D **50**, 5000 (1994).

[18] J. Massó, E. Seidel, W.-M. Suen, and P. Walker, “Event horizons in numerical relativity. II. Analyzing the horizon,” Phys. Rev. D **59**, 064015 (1999).

[19] M. R. Schroeder, *Number Theory in Science and Communication* Springer-Verlag, Berlin, 1986.

[20] W. H. Press, B. P. Flannery, S. A. Teukolsky, and W. T. Vetterling, *Numerical Recipes*, Cambridge University Press, Cambridge, England, 1986.

[21] D. S. Brill, “On the positive definite mass of the Bondi-Weber-Wheeler time-symmetric gravitational waves,” Ann. Phys. **7**, 466 (1959).

[22] G. Allen, K. Camarda, and E. Seidel, “Black Hole Spectroscopy: Determining Waveforms from 3D Excited Black Holes,” (1998), gr-qc/9806036, submitted to Phys. Rev. D.

[23] K. Camarda and E. Seidel, “Numerical evolution of dynamic 3D black holes: Extracting waves, ” Phys. Rev. D **57**, R3204 (1998), gr-qc/9709075.

[24] P. Anninos *et al.*, “Three-dimensional numerical relativity: The evolution of black holes,” Phys. Rev. D **52**, 2059 (1995).

[25] A. Abrahams *et al.*, “Numerically generated black-hole spacetimes: Interaction with gravitational waves, ” Phys. Rev. D **45**, 3544 (1992).

[26] *The Cactus Code Web Page, http://www.cactuscode.org*, as of May 10, 2001.

[27] K. Camarda, ”A numerical study of 3D black hole spacetimes,” Ph.D. thesis, University of Illinois at Urbana-Champaign, Urbana, Illinois, 1998.

[28] G. Allen, K. Camarda, and E. Seidel, “Evolution of Distorted Black Holes: A Perturbative Approach,” (1998), gr-qc/9806014, submitted to Phys. Rev. D.

Appendix A

Diffraction-Free beams

A trivial example of a diffraction-free beam is an infinite plane wave:

$$E = e^{i\beta z - \omega t}. \tag{A.1}$$

Perfect plane waves cannot be realized in practice because they have infinite energy and are not too interesting for LIGO. There exists however another solution to the Maxwell Equations that is not constant but also diffraction-free. They are known as Bessel beams [20] and are given by

$$E = e^{i\beta z - \omega t} J_o(\alpha r), \tag{A.2}$$

where

$$r = x^2 + y^2 \tag{A.3}$$

is the distance from the optic axis chosen as z, and J_o is the 0^{th} order Bessel function of the first kind. When $\alpha = 0$, the Bessel beam becomes a plane wave. For $0 < \alpha \leq \frac{\omega}{c}$,this solution describes a non-diffracting beam with amplitude distribution profile decaying at a rate proportional to $\frac{1}{\alpha r}$. The effective width of the beam is determined by α and is the smallest for

$$\alpha = \frac{\omega}{c} = \frac{s\pi}{\lambda}. \tag{A.4}$$

In this limit case, the central spot diameter is about $\frac{3\lambda}{4}$.

Higher-order Bessel beams are also diffraction-free and are given by

$$E_n = e^{i\beta z - \omega t - n\phi} J_n(\alpha r), \tag{A.5}$$

with n a positive integer and ϕ being the azimuthal angle.

The Bessel beams, however, still require infinite energy to create. Their electric field amplitude decays like $\frac{1}{r}$ and their power like $\frac{1}{r^2}$. As we live in a three-dimensional universe, the total power the beam carries at a distance r from the optic axis decays like $\frac{1}{r}$, and integrating this yields infinity. Finite (truncated) versions of the Bessel beams have been created experimentally [21].

Intuitively, Bessel beams can be thought as a superposition of plane waves with wave vectors along the generators of a cone. As the beams interfere, they will produce the Bessel beam centered on the cone's axis. As there are infinitely many infinite plane waves positioned in this manner, the interference pattern, i.e., the Bessel beam will not depend in z, i.e., will be diffraction-free.

A way to produce finite-energy, low-diffraction beams related to the Bessel beams is to replace the plane waves from the previous paragraph with Gaussians. This yields a beam with minimal diffraction known as Bessel-Gauss. The electric field of such a beam near $z = 0$ is given by

$$E = e^{i\beta z - \omega t} J_o(\alpha r) e^{-\frac{r^2}{w_o^2}}. \tag{A.6}$$

For higher order Bessel beams, the Bessel Gauss correspondent is given by

$$E_n = e^{i\beta z - \omega t - n\phi} J_n(\alpha r) e^{-\frac{r^2}{w_o^2}}. \tag{A.7}$$

Bessel-Gauss beams can easily be obtained experimentally by shining a Gaussian or a Laguerre-Gaussian for higher-order Bessel Gauss beams through a conical lens [22]. This paper also notes an interesting self-healing property of the Bessel-Gauss beams. It is claimed that such a beam will repair itself if subjected to small perturbation, such as dust in the propagating medium or possibly mirror figure errors.

The Bessel beams have conical phase fronts and, in some regimes, the Bessel-Gauss beams have conical phase fronts as well. Our minimization algorithm has converged to something surprisingly similar to a Bessel–Gauss beam. The Bessel-Gauss beams, however, appear not to fall in intensity at a specified radius as sharply as do the beams we present in this paper. Their beam shapes [23] and mirrors, as well as the low diffraction we had sought, are all there to witness for their similarity.

Appendix B

Perturbation Theory

B.1 General Principle

Our problem can be summarized as follows: Suppose the propagation from one perfect mirror surface to the other perfect mirror surface is G, and suppose the mirror deviations are $\Delta_j(\vec{r})$, $j = 1, 2$, then the problem is

$$G(1+\epsilon T_1)G(1+\epsilon T_2)\psi_\alpha = \lambda_\alpha \psi_\alpha, \tag{B.1}$$

where

$$T_j(\vec{r}, \vec{r}\,') = 2ik\Delta_j(\vec{r})\delta(\vec{r} - \vec{r}\,'). \tag{B.2}$$

For convenience, we denote

$$U \equiv GG\,, \quad V^{(1)} \equiv GT_1G + GGT_2\,, \quad V^{(2)} \equiv GT_1GT_2 + \frac{1}{2}[GT_1^2G + GGT_2^2]\,. \tag{B.3}$$

We note that the operator U is *symmetric*, but neither *Hermitia* nor *unitary.* It is therefore hard to argue that G has a complete set of eigenvectors. Nevertheless, it is possible to establish some sort of orthogonality system. Suppose $\lambda_\alpha \neq \lambda_\beta$, then it is easy to verify that

$$\psi_\alpha^T G = \lambda_\alpha \psi_\alpha^T\,, \tag{B.4}$$

and that

$$\psi_\alpha^T \psi_\beta = 0\,. \tag{B.5}$$

If there do not exist eigenvectors with $\psi_\alpha^T\psi_\alpha = 0$ (or if we first exclude them from our analysis), we can then normalize the eigenvectors appropriately to give

$$\psi_\alpha^T \psi_\beta = \delta_{\alpha\beta}\,. \tag{B.6}$$

Since the eigenvectors are complex, we still use Dirac bracket notation to facilitate computation. In this notation, we denote ψ_α^T, which is the Hermitian conjugate of ψ_α^*, as $\langle\tilde{\psi}_\alpha|$. Our current knowledge translates into

$$U|\psi_\beta\rangle = \lambda_\beta|\psi_\beta\rangle\,,\ \langle\tilde{\psi}_\alpha|U = \langle\tilde{\psi}_\alpha|\lambda_\alpha\,,\ \langle\tilde{\psi}_\alpha|\psi_\beta\rangle = \delta_{\alpha\beta}\,. \tag{B.7}$$

We can also define

$$\tilde{E} \equiv \sum_\alpha |\psi_\alpha\rangle\langle\tilde{\psi}_\alpha|\,, \tag{B.8}$$

but it is only possible to verify that $\tilde{E}$ is a projection operator, with $\tilde{E}\tilde{E} = \tilde{E}$. If we had excluded eigenvectors with $\psi_\alpha^T\psi_\alpha = 0$, then $\tilde{E}$ would certainly not be identity. But we do have to pretend $\tilde{E}$ to be complete, in order to get an expansion.

Now we construct a perturbation sequence. To start with, we have

$$[U+\epsilon V^{(1)}+\epsilon^2 V^{(2)}][|\psi_\alpha^{(0)}\rangle+\epsilon|\psi_\alpha^{(1)}\rangle+\epsilon^2|\psi_\alpha^{(2)}\rangle] = [\lambda_\alpha^{(0)}+\epsilon\lambda_\alpha^{(1)}+\epsilon^2\lambda_\alpha^{(2)}][|\psi_\alpha^{(0)}\rangle+\epsilon|\psi_\alpha^{(1)}\rangle+\epsilon^2|\psi_\alpha^{(2)}\rangle] \tag{B.9}$$

which gives

$$\begin{aligned} U\psi_\alpha^{(0)}\rangle &= \lambda_\alpha^{(0)}|\psi_\alpha^{(0)}\rangle && \text{(B.10)}\\ U|\psi_\alpha^{(1)}\rangle + V^{(1)}|\psi_\alpha^{(0)}\rangle &= \lambda_\alpha^{(0)}|\psi_\alpha^{(1)}\rangle + \lambda_\alpha^{(1)}|\psi_\alpha^{(0)}\rangle && \text{(B.11)}\\ U|\psi_\alpha^{(2)}\rangle + V^{(1)}|\psi_\alpha^{(1)}\rangle + V^{(2)}|\psi_\alpha^{(0)}\rangle &= \lambda_\alpha^{(0)}|\psi_\alpha^{(2)}\rangle + \lambda_\alpha^{(1)}|\psi_\alpha^{(1)}\rangle + \lambda_\alpha^{(2)}|\psi_\alpha^{(0)}\rangle\,. && \text{(B.12)} \end{aligned}$$

At first order, this leads to

$$\begin{aligned} \lambda_\alpha^{(1)} &= \langle\tilde{\psi}_\alpha^{(0)}|V^{(1)}|\psi_\alpha^{(0)}\rangle && \text{(B.13)}\\ |\psi_\alpha^{(1)}\rangle &= \sum_\beta \frac{|\psi_\beta^{(0)}\rangle\langle\tilde{\psi}_\beta^{(0)}|V^{(1)}|\psi_\alpha^{(0)}\rangle}{\lambda_\alpha^{(0)}-\lambda_\beta^{(0)}}\,. && \text{(B.14)} \end{aligned}$$

At second order, we only need λ_α^2, which is given by [note that $\langle\tilde{\psi}_\alpha^{(0)}|\psi_\alpha^{(1)}\rangle = 0$]

$$\lambda_\alpha^{(2)} = \sum_\beta \frac{\langle\tilde{\psi}_\alpha^{(0)}|V^{(1)}|\psi_\beta^{(0)}\rangle\langle\tilde{\psi}_\beta^{(0)}|V^{(1)}|\psi_\alpha^{(0)}\rangle}{\lambda_\alpha^{(0)}-\lambda_\beta^{(0)}} + \langle\tilde{\psi}_\alpha^{(0)}|V^{(2)}|\psi_\alpha^{(0)}\rangle\,. \tag{B.15}$$

We now insert the specific forms of $V^{(1,2)}$, and assume that eigenmodes of U are also those of G, and denote $\lambda_\alpha = \eta_\alpha^2$. We finally obtain [with the help of inserting $\tilde{E}$]

$$\lambda_\alpha^{(2)} = \eta_\alpha^2 \sum_\beta \frac{1}{\eta_\alpha^2-\eta_\beta^2}\left[\frac{\eta_\alpha^2+\eta_\beta^2}{2}(F_{1\alpha\beta}^2+F_{2\alpha\beta}^2) + 2\eta_\alpha\eta_\beta F_{1\alpha\beta}F_{2\alpha\beta}\right]\,, \tag{B.16}$$

with

$$F_{j\alpha\beta} = \langle \tilde{\psi}_\alpha^{(0)} | T_j | \psi_\beta^{(0)} \rangle = \langle \tilde{\psi}_\beta^{(0)} | T_j | \psi_\alpha^{(0)} \rangle \,, \tag{B.17}$$

where second equality holds because T_j is also a symmetric operator.

B.2 Mirror Tilt

To specialize in our case, we note that $\alpha = (00)$, meaning that we start with the fundamental, axisymmetric mode. The wave function is $\psi_{00}(\vec{r}) = u_{00}(r)$, with

$$\int u_{00}(r) r dr = \frac{1}{\sqrt{2\pi}} \,. \tag{B.18}$$

For tilt, we have

$$T_a(\vec{r}, \vec{r}\,') = 2ik\theta_a |\vec{r}| \cos\varphi \delta(\vec{r} - \vec{r}\,') \,, \quad a = 1, 2. \tag{B.19}$$

Since T has a φ dependence of $\cos\varphi$, we only need β fields with $\cos\varphi$ dependence, which we denote by $\beta = (1j)$; the wave function is $\psi_{1j}(\vec{r}) = u_{1j}(r)\cos\varphi$, with

$$\int u_{1j}(r) r dr = \frac{1}{\sqrt{\pi}}. \tag{B.20}$$

For tilt, we obtain, explicitly,

$$F_{a(00)(1l)} = \sqrt{2} ik\theta_a \frac{\int_0^R u_{00} u_{1l} r^2 dr}{\sqrt{\int_0^R u_{00}^2 r dr \int_0^R u_{1l}^2 r dr}} \,. \tag{B.21}$$

Here it is understood that u_{00} and u_{1l} are functions of r. In addition, ambiguity in taking the square root will disappear in the final result, because $F_{a\alpha\beta}$ always appear in pairs.

Results using perturbation theory have been verified directly with results from FFT code. If we would like to understand the origin of the high loss in the conical cavity, we can estimate the contribution from one particular $\beta = (1l)$. Suppose the mode still has $\eta_{1l} = 1 - \epsilon_l$, with $|\epsilon_l| \ll 1$. It is then easy to show that (up to leading order in ϵ_l)

$$\lambda^{(2)} \approx \frac{1}{2\epsilon_l}(F_1 + F_2)^2. \tag{B.22}$$

The power loss added by tilt is then

$$\delta\mathcal{L} = -\mathrm{Re}\left[\frac{1}{\epsilon_l}(F_1 + F_2)^2\right] \,. \tag{B.23}$$

It may not be unreasonable to assume that $F_{1,2}$ is purely imaginary, because the overlap integral in

Eq. (B.21) should be mostly real (the mirror should correspond well to the phase front), so we have

$$\delta\mathcal{L} \approx -Re(1/\epsilon_l)(F_1+F_2)^2. \tag{B.24}$$

Suppose that we can further write $\epsilon = \mathcal{L}_l/4 + i\phi_l/2$, where $\mathcal{L}_l$ is the diffractional loss of the $(1l)$ mode, and ϕ_l is some detuning. We therefore have

$$\delta\mathcal{L} \approx \mathcal{L}_l \underbrace{\left[\frac{1}{(\mathcal{L}_l/2)^2+\phi_l^2}\right]}_{\text{resonance feature}} \underbrace{\left[2k^2(\theta_1+\theta_2)^2\right]}_{\text{driving amplitude}} \underbrace{\left[\frac{\left(\int_0^R u_{00}u_{1l}r^2dr\right)^2}{\int_0^R u_{00}^2 r dr \int_0^R u_{1l}^2 r dr}\right]}_{\text{overlap function}}. \tag{B.25}$$

This has the following explanation. When mirrors are tilted, the $(1l)$ mode is generated, and combines with (00) mode to form the new eigenmode. The amount that is generated depends on the driving amplitude, overlap function, and resonance feature of the $(1l)$ mode — basically how far away is the $(1l)$ eigenfrequency from the (00) eigenfrequency. This amount of the $(1l)$ mode, times its optical loss, $\mathcal{L}_l$, then gives the additional optical loss.

Following this explanation, in order to have a cavity tolerant to tilt and other imperfections, we would first of all require that $(\mathcal{L}_l^2+\phi_l^2)$ not to be too small, such that the modal structure is *non-degenerate*, and not too much of higher modes will be generated when the mirrors are imperfect. However, we would also require that $\mathcal{L}_l$ to be small, such that even some higher modes were generated, they do not get lost easily, but remain circulating in the cavity. For this reason, the existence of higher-order, low-loss modes is essential to the cavity's tolerance to imperfections. At this stage, this seems very obvious.

Comparing a conical resonator with spherical and Mesa resonators reveals that conical resonators are particularly bad in this respect. Only one mode, the fundamental mode, has a very low diffractional loss, while all other modes have losses higher than 1 percent.